

Condensed Matter Theory of Dipolar Quantum Gases

M. A. Baranov,^{†,‡,§} M. Dalmonte,^{†,⊥} G. Pupillo,^{†,‡,∇} and P. Zoller^{*,†,‡}

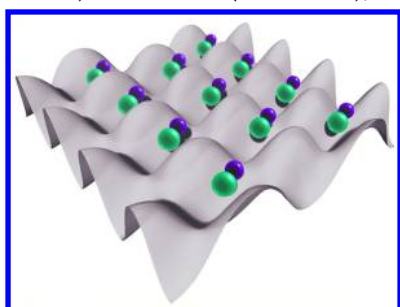
[†]Institute for Quantum Optics and Quantum Information of the Austrian Academy of Sciences, A-6020 Innsbruck, Austria

[‡]Institute for Theoretical Physics, University of Innsbruck, A-6020 Innsbruck, Austria

[§]RRC “Kurchatov Institute”, Kurchatov Square 1, 123182, Moscow, Russia

[⊥]Dipartimento di Fisica dell’Università di Bologna, via Irnerio 46, 40126 Bologna, Italy

[∇]ISIS (UMR 7006) and IPCMS (UMR 7504), Université de Strasbourg and CNRS, Strasbourg, France



CONTENTS

1. Introduction	5012
2. Dipole–Dipole Interaction	5013
2.1. Scattering of Two Dipoles	5013
2.2. Tunability of the Dipole–Dipole Interaction	5014
2.2.1. Tunability of Interactions in Cold Atoms	5014
2.2.2. Effective Hamiltonians for Polar Molecules	5014
2.2.3. Stabilization of Dipolar Interactions in 2D	5016
2.2.4. Advanced Interaction Designing: Blue-Shielding	5017
3. Weakly Interacting Dipolar Bose Gas	5017
3.1. BEC in a Spatially Homogeneous Gas	5017
3.2. BEC in a Trapped Gas	5018
3.2.1. Ground State	5018
3.2.2. Collective Excitations and Instability	5020
3.2.3. Roton Instability of a Quasi 2D Dipolar Condensate	5022
4. Weakly Interacting Dipolar Fermi Gas	5024
4.1. Effects of Dipole–Dipole Interactions	5025
4.2. Normal (Anisotropic) Fermi Liquid State	5025
4.2.1. Anisotropic Fermi Surface and Single-Particle Excitations	5026
4.2.2. Collective Modes (Landau Zero Sound)	5027
4.3. BCS Pairing in a Homogeneous Single-Component Dipolar Fermi Gas	5028
4.4. BCS Pairing in a Trapped Single-Component Dipolar Fermi Gas	5031
4.5. BCS Pairing in a Two Component Dipolar Fermi Gas	5032
4.6. BCS Pairing in a Dipolar Monolayer	5033
4.7. BCS Pairing in a Bilayer Dipolar System	5035
4.8. Stability of Fermionic Dipolar Systems	5037
5. Dipolar Multilayer Systems	5039
6. Strongly Interacting Dipolar Gas	5039

6.1. Two-Dimensional Dipoles: Phase Diagram	5039
Confined Geometries	5040
Open Questions	5041
6.2. Optical Lattices	5041
6.2.1. Dipoles on a 2D Lattice Monolayer	5041
6.2.2. Polarized Dipoles on a Bilayer Optical Lattice	5044
6.3. Advanced Hamiltonian Design with Polar Molecules	5044
6.3.1. Three-Body Interactions	5044
6.3.2. Lattice Spin Models and Quantum Magnetism	5045
6.3.3. Hubbard Models in Self-Assembled Dipolar Lattices	5047
7. Dipolar Gases in One- and Quasi-One-Dimensional Geometries	5048
7.1. Dipolar Gases in a Single Tube	5048
7.1.1. Bosonic and Fermionic Gases in a Shallow Optical Lattice	5050
7.1.2. Bosonic Gases in a Deep Optical Lattice: Extended Bose–Hubbard Models	5050
7.2. Two-Species Mixtures	5051
7.2.1. Fermi–Fermi Mixtures	5051
7.2.2. Bose–Fermi Mixtures	5053
7.3. Quasi-1D Physics: Coupling between Tubes	5053
7.3.1. Two-Leg Ladders	5053
7.3.2. Planar Array of Tubes	5055
8. Conclusions and Outlook	5056
Author Information	5056
Corresponding Author	5056
Notes	5056
Biographies	5057
Acknowledgments	5057
References	5057

1. INTRODUCTION

The realization of Bose Einstein condensates (BEC) and quantum degenerate Fermi gases with cold atoms has been a highlight of quantum physics during the past decade. Cold atoms in the tens of nanokelvin range are routinely obtained via combined laser- and evaporative-cooling techniques.¹ For high-

Special Issue: 2012 Ultracold Molecules

Received: September 9, 2011

Published: August 9, 2012

enough densities ($\gtrsim 10^{12} \text{ cm}^{-3}$), the atomic de Broglie wavelength becomes larger than the typical interparticle distance, and thus, quantum statistics governs the many-body dynamics of these systems. The characteristic features of the physics of cold atomic gases are the microscopic knowledge of the many-body Hamiltonians which are realized in the experiments and the possibility of controlling and tuning system parameters via external fields. External field control of contact interparticle interactions can be achieved, for example, by varying the scattering length via Feshbach resonances,² while trapping of ultracold gases is obtained with magnetic, electric, and optical fields.³ In particular, optical lattices, which are artificial crystals made of light obtained via the interference of optical laser beams, can realize perfect arrays of hundreds of thousands of microtraps,^{4,5} allowing for the confinement of quantum gases to one-dimensional (1D), 2D, and 3D geometries and even the manipulation of individual particles.^{6,7} This control over interactions and confinement is the key for the experimental realization of fundamental quantum phases and phase transitions, as illustrated by the BEC-BCS crossover in atomic Fermi gases⁸ and the Berezinskii–Kosterlitz–Thouless transition⁹ for cold bosonic atoms confined to 2D.

Breakthroughs in the experimental realization of BEC and degenerate Fermi gases of atoms with a comparatively large magnetic dipole moment, such as ^{52}Cr ,^{10–16,298,299,300} ^{168}Er ,¹⁷ and ^{164}Dy atoms^{18,19} (dipole moment $6 \mu_{\text{B}}$, $7 \mu_{\text{B}}$, and $10 \mu_{\text{B}}$, respectively, with μ_{B} Bohr's magneton), and the recent astounding progress in experiments with ultracold polar molecules^{20–31} have now stimulated great interest in the properties of low temperature systems with dominant dipolar interactions (see reviews in refs 32–36 for discussions of various aspects of the problem). The latter have a long-range and anisotropic character, and their relative strength compared to, e.g., short-range interactions can often be controlled by tuning external fields or else by adjusting the strength and geometry of confining trapping potentials. For example, in experiments with polarized atoms, magnetic dipolar interactions can be made to overcome short-range interactions by tuning the effective *s*-wave scattering length to zero using Feshbach resonances.^{10–13} This has already led to the observation of fundamental phenomena at the mean-field level, such as, the anisotropic deformation during expansion and the directional stability^{18,37} of dipolar BECs. Heteronuclear polar molecules in a low vibrational and rotational state, on the other hand, can have large permanent dipole moments along the internuclear axis with strength ranging between one tenth and ten Debye (1 D $\approx 3.335 \times 10^{-30}$ C·m). In the presence of an external electric field (with a typical value of 10^3 – 10^4 V/cm) mixing rotational excitations, the molecules can be oriented in the laboratory frame and the induced dipole moment can approach its asymptotic value, corresponding to the permanent dipole moment. This effect can be used to tune the strength of the dipole–dipole interaction.³⁵ Additional microwave fields allow for advanced tailoring of the interactions between the molecules, where even the shape of interaction potentials can be tuned with external fields, in addition to the strength. This tunability of interactions forms the basis for the realization of novel quantum phenomena in these systems, in the strongly interacting limit.

As a result of this progress, in recent years dipolar gases have become the subject of intensive theoretical efforts, and there is now an extensive body of literature predicting novel properties for these systems.^{32–36} It is the purpose of this review to

provide a summary of these recent theoretical studies with a focus on the many-body quantum properties, to demonstrate the connections and differences between dipolar gaseous systems and traditional condensed-matter systems, and to stress the inherent interdisciplinary nature of these studies. This work covers spatially homogeneous as well as trapped systems, and it includes the analysis of the properties of dipolar gases both in the mean-field (dipolar Bose–Einstein condensates and superfluid BCS pairing transition) and in the strongly correlated (dipolar gases in optical lattices and low-dimensional geometries) regimes.

We tried our best to include all relevant works of this exciting, ever expanding field. We apologize in advance if some papers (hopefully, not many) do not appear below.

2. DIPOLE–DIPOLE INTERACTION

For *polarized* dipolar particles, interparticle interactions include both a short-range van der Waals (vdW) part and a long-range dipole–dipole one. The latter is dominant at large interparticle separations, and assuming a polarization along the *z*-axis as in Figure 1a, the interparticle interaction reads

$$V_{dd}(\mathbf{r}) = \frac{d^2}{r^3}(1 - 3 \cos^2 \theta) \quad (1)$$

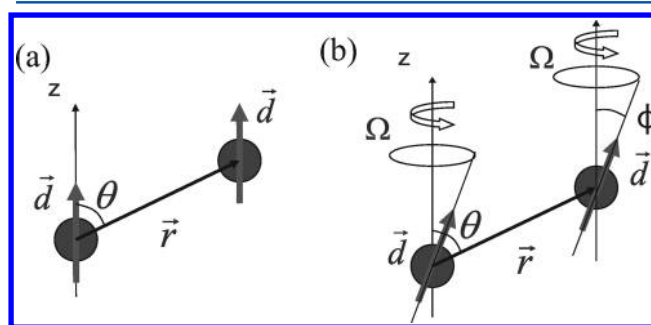


Figure 1. (a) Geometry for the interaction of two aligned dipoles. (b) Tunability of the dipole–dipole interaction by using a time-varying aligning field. The angle ϕ between the dipole orientation and the *z*-axis determines the strength and the sign of the effective interaction.

Here d is the electric dipole moment (for magnetic dipoles d^2 should be replaced with μ^2 , with μ the magnetic dipole moment), \mathbf{r} is the vector connecting two dipolar particles, and θ is the angle between \mathbf{r} and the dipole orientation (the *z*-axis). The potential $V_{dd}(\mathbf{r})$ is both *long-range* and *anisotropic*, that is, partially repulsive and partially attractive. As discussed in the sections below, these features have important consequences for the scattering properties in the ultracold gas, for the stability of the system, as well as for a variety of its properties.

2.1. Scattering of Two Dipoles

The long-range character ($\sim r^{-3}$) of the dipole–dipole interaction results in all partial waves contributing to the scattering at low energies, and not only, e.g., the *s*-wave, as is often the case for short-range interactions. In fact, for dipole–dipole interactions, the phase shift δ_l in a scattering channel with angular momentum l behaves as $\delta_l \sim k$ for $l \geq 0$ and small k (see, e.g., refs 38 and 39).

The effect of the anisotropy of the interaction is instead that the angular momentum is not conserved during scattering: for bosons and fermions, the dipole–dipole interaction mixes all even and odd angular momenta scattering channels, respec-

tively. Due to the coupling between the various scattering channels, the potential V_{dd} then generates a short-range contribution to the total effective potential in the s -wave channel ($l = 0$). This has the general effect to reduce the strength of the short-range part of the interaction.

Thus, for two bosonic dipolar particles (even angular momenta), the scattering at low energies is determined by both the long-range and the short-range parts of the interaction. This is in contrast to the low energy scattering of two fermionic dipoles (odd angular momenta), which is universal in the sense that it is determined only by the long-range dipolar part of the interaction and is insensitive to the short-range details.

For a dilute weakly interacting gas, the above results allow a parametrization of the realistic interparticle interaction between two particles of mass m in terms of the following pseudopotential^{40,41} (see also refs 42 and 43)

$$V(r) = g\delta(\mathbf{r}) + \frac{d^2}{r^3}(1 - 3\cos^2\theta) \quad (2)$$

with

$$g = \frac{4\pi\hbar^2 a(d)}{m} \quad (3)$$

parametrizing the short-range part of the interaction. We note that the long-range part of the pseudopotential $V(r)$ is identical to the long-range part of the original potential and that the scattering length $a(d)$ controlling the short-range part depends on the dipole moment. This dependence is important⁴⁴ when one changes the dipole moment, using external, e.g. electric, fields, as explained below.

The strength of the dipole–dipole interaction can be characterized by the quantity

$$a_d = \frac{md^2}{\hbar^2}$$

which has the dimension of length and can be considered as a characteristic range of the dipole–dipole interaction, or dipolar length. This length determines the low energy limit of the scattering amplitudes, and, in this sense, a_d is analogous to the scattering length for the dipole–dipole interaction. For chromium atoms with a comparatively large magnetic moment of $6\mu_B$ (equivalent dipole moment $d = 0.056$ D), we have $a_d \approx 2.4$ nm. For most polar molecules the electric dipole moment ranges in between 0.1 and 1 D, while a_d ranges from 1 to 10^3 nm. For example, the dipole moment of fermionic ammonia molecules $^{15}\text{ND}_3$ is $d = 1.5$ D with $a_d = 712$ nm, while for $\text{H}^{12}\text{C}^{14}\text{N}$ it increases to $d = 2.98$ D and $a_d = 3620$ nm. This latter value of the effective scattering length is an order of magnitude larger than, for example, the one for the intercomponent interaction in the widely discussed case of a two-species fermionic gas of ^6Li , where $a_{\text{Li}} = -114$ nm. Thus, the strength of the dipole–dipole interaction between polar molecules can be not only comparable with but even much larger than the strength of the short-range interatomic interaction.

2.2. Tunability of the Dipole–Dipole Interaction

One spectacular feature of the dipole–dipole interaction is its tunability. In section 2.2.1 we first review methods for tuning the *strength* and *sign* of dipolar interactions with an eye to cold atoms, and then in section 2.2.2 we discuss tunability for the specific case of polar molecules, where both the *strength* as well as the *shape* of interactions can be engineered.

2.2.1. Tunability of Interactions in Cold Atoms. In ref 45 a technique has been developed to tune the strength as well as the sign of dipolar interactions in atomic systems with a finite permanent magnetic dipole moment. This technique uses a combination of a static (e.g., magnetic) field along the z -axis and a fast rotating field in the perpendicular xy -plane such that the resulting time dependent dipole moment is (see Figure 1b)

$$\mathbf{d}(t) = d\{\mathbf{e}_z \cos\phi + [\mathbf{e}_x \cos(\Omega t) + \mathbf{e}_y \sin(\Omega t)] \sin\phi\}$$

Here Ω is the rotating frequency of the field and the angle ϕ , $0 \leq \phi < \pi/2$, is determined by the ratio of the amplitudes of the static and rotating fields. The above expression implies that the dipoles follow the time-dependent external field adiabatically. This in turn sets an upper limit on the values of the rotating frequency Ω , which should be (much) smaller than the level splitting in the field. However, if the frequency Ω is much larger than the typical frequencies of the particle motion, over the period $2\pi/\Omega$ the particles feel an average interaction V_d

$$\langle V_d(\mathbf{r}) \rangle = \frac{d^2}{r^3}(1 - 3\cos^2\theta)\alpha(\phi)$$

The latter differs from the interaction for aligned dipoles, eq 1, by a factor $\alpha(\phi) = (3\cos^2\phi - 1)/2$, which can be changed continuously from 1 to $-1/2$ by varying the angle ϕ . Thus, this method allows “reversal” of the sign of the dipole–dipole interaction and even cancellation of it completely for $\phi = a \cos 1/\sqrt{3} = 54.7$, similar to the case of NMR techniques.⁴⁶ We note that an analogous technique can also be applied for the electric dipole moments of, e.g., polar molecules. We will review applications of this method below.

2.2.2. Effective Hamiltonians for Polar Molecules. In the following we will be often interested in manipulating interactions for polar molecules in the *strongly interacting* regime. In particular, we will aim at modifying not only the strength but also the *shape* of interaction potentials, as a basis to investigate new condensed matter phenomena. This usually entails a combination of the following two steps: (i) manipulating the internal (electronic, vibrational, rotational, ...) structure of the molecules, and thus their mutual interactions, using external static (dc) electric and microwave (ac) fields, and (ii) confining molecules to a lower-dimensional geometry, using, e.g., optical potentials, as exemplified in Figure 2. Under appropriate conditions, the resulting effective interactions can be made *purely repulsive* at large distances (e.g., at characteristic distances of 10 nm or more), as in the 2D example of Figure 3a. On one hand, this has the effect to suppress possible inelastic collisions and chemical reactions occurring at short-range (i.e., at characteristic distances of $a_c \lesssim 1$ nm), and on the other hand, it allows study of interesting condensed matter phenomena originating from the often-unusual form of the two-body (or many-body-) interaction potentials. In the next few subsections, we review techniques for the engineering of the interaction potentials which will be used in the many-body context in section 6.

Our starting point is the Hamiltonian for a gas of cold heteronuclear molecules prepared in their electronic and vibrational ground-state,

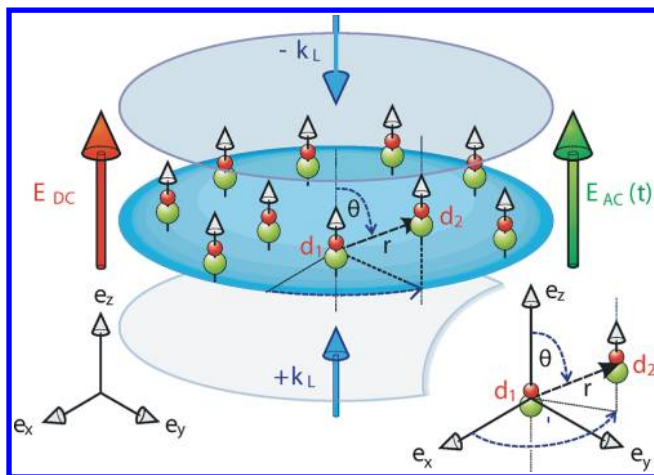


Figure 2. System setup: Polar molecules are trapped in the (x,y) -plane by an optical lattice made of two counter-propagating laser beams with wavevectors $\pm \mathbf{k}_L = \pm k_L \mathbf{e}_z$ (blue arrows). The dipoles are aligned in the z -direction by a dc electric field $\mathbf{E}_{dc} \equiv E_{dc} \mathbf{e}_z$ (red arrow). An ac microwave field is indicated (green arrow). Inset: Definition of polar (θ) and azimuthal (ϕ) angles for the relative orientation of the intermolecular collision axis \mathbf{r}_{12} with respect to a space-fixed frame, with axis along z . [Adapted from ref 57.]

$$H(t) = \sum_i^N \left[\frac{\mathbf{p}_i^2}{2m} + V_{\text{trap}}(\mathbf{r}_i) + H_{\text{in}}^{(i)} - \mathbf{d}_i \cdot \mathbf{E}(t) \right] + \sum_{i < j}^N V_{\text{dd}}(\mathbf{r}_i - \mathbf{r}_j) \quad (4)$$

Here the first term in the single particle Hamiltonian corresponds to the kinetic energy of the molecules, while $V_{\text{trap}}(\mathbf{r}_i)$ represents a trapping potential, as provided, for example, by an optical lattice or an electric or magnetic trap. The term $H_{\text{in}}^{(i)}$ describes the internal low energy excitations of the molecule, which for a molecule with a closed electronic shell $^1\Sigma(\nu = 0)$ (e.g., SrO, RbCs, or LiCs) correspond to the rotational degree of freedom of the molecular axis. This term is

well described by a rigid rotor $H_{\text{in}}^{(i)} = H_{\text{rot}}^{(i)} = B \mathbf{J}_i^2$ with B the rotational constant (in the few to tens of GHz regime) and \mathbf{J}_i the dimensionless angular momentum. The rotational eigenstates $|J, M\rangle$ for a quantization axis z and with eigenenergies $B J(J + 1)$ can be coupled by a static (dc) or microwave (ac) field \mathbf{E} via the electric dipole moment \mathbf{d}_i , which is typically of the order of a few Debye.

In the absence of electric fields, the molecules prepared in a ground rotational state $J = 0$ have no net dipole moment, and they interact via a van-der-Waals attraction $V_{\text{vdw}} \sim -C_6/r^6$, reminiscent of the interactions of cold alkali metal atoms in the electronic ground-states. Electric fields admix excited rotational states and induce static or oscillating dipoles, which interact via strong dipole–dipole interactions V_{dd} with the characteristic $1/r^3$ dependence given in eq 1. For example, a static dc field couples the spherically symmetric rotational ground state of the molecule to excited rotational states with different parity, thus creating a nonzero average dipole moment. The field strength therefore determines the degree of polarization and the magnitude of the dipole moment. As a result, the effective dipole–dipole interaction may be tuned by the competition between an orienting, e.g., dc electric field and the quantum (or thermal) rotation of the molecule. This method effectively works for the values of the field up to the saturation limit, at which the molecule is completely polarized (typically 10^4 V/cm).

The many body dynamics of cold polar molecules is thus governed by an interplay between dressing and manipulating the rotational states with dc and ac fields, and strong dipole–dipole interactions. In condensed matter physics, one is often interested in effective theories for the low-energy dynamics of the many-body system, after the high-energy degrees of freedom have been traced out. The connection between the full molecular N -particle Hamiltonian (4) including rotational excitations and dressing fields, and an effective low-energy theory can be made using the following Born–Oppenheimer approximation: The diagonalization of the Hamiltonian $H_{BO} = \sum_i^N [H_{\text{in}}^{(i)} - \mathbf{d}_i \cdot \mathbf{E}] + \sum_{i < j}^N V_{\text{dd}}(\mathbf{r}_i - \mathbf{r}_j)$ for frozen spatial positions $\{\mathbf{r}_i\}$ of the N molecules yields a set of energy eigenvalues

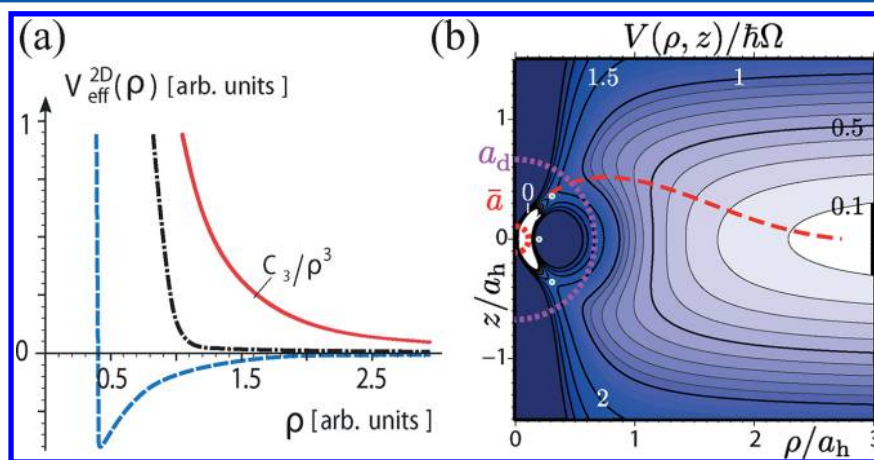


Figure 3. (a) Effective repulsive interaction potentials in 2D. Solid line: Dipolar potential $V_{\text{eff}}^{2D}(\rho) = D/\rho^3$ induced by a dc electric field in the configuration of Figure 2 [$E_{dc} > 0$ and $E_{ac}(t) = 0$]. Dash-dotted line: “Steplike” potential induced by a single ac microwave field and a weak dc field (see also Figure 5). Dashed line: Attractive potential induced by the combination of several ac fields and a weak dc field. The potentials $V_{\text{eff}}^{2D}(\rho)$ and the separation ρ are given in arbitrary units. (b) Potential $V(\rho, z)/(\hbar\Omega)$ versus ρ/a_h and z/a_h for $|m_l| = 1$ for $^{40}\text{K}^{87}\text{Rb}$ in a $\Omega = 2\pi(50 \text{ kHz})$ trap, where $a_h = 56.4 \text{ nm}$, $\bar{a} = 6.25 \text{ nm}$,⁴⁸ and $d = 0.2 \text{ D}$. White circles: saddle points. Dashed lines: semiclassical trajectory for the collision of two molecules. The dashed half-circles show \bar{a} and a_q . (Panels a and b are adapted from refs 57 and 60, respectively.)

$V_{\text{eff}}^{3\text{D}}(\{\mathbf{r}_i\})$, which can be interpreted as the effective interaction potential in the single-channel many-body Hamiltonian

$$H_{\text{eff}} = \sum_{i=1}^N \left[\frac{\mathbf{p}_i^2}{2m} + V_{\text{trap}}(\mathbf{r}_i) \right] + V_{\text{eff}}^{3\text{D}}(\{\mathbf{r}_i\}) \quad (5)$$

The term $V_{\text{eff}}^{3\text{D}}(\{\mathbf{r}_i\})$ represents an effective N -body interaction, which can be expanded as a sum of two-body and many-body interactions

$$V_{\text{eff}}^{3\text{D}}(\{\mathbf{r}_i\}) = \sum_{i<j}^N V^{3\text{D}}(\mathbf{r}_i - \mathbf{r}_j) + \sum_{i<j<k}^N W^{3\text{D}}(\mathbf{r}_i, \mathbf{r}_j, \mathbf{r}_k) + \dots \quad (6)$$

where in most cases only two-body interactions are considered. The dependence of $V_{\text{eff}}^{3\text{D}}(\{\mathbf{r}_i\})$ on the electric fields \mathbf{E} provides the basis for the engineering of the many body interactions, as described below.

We note that the attractive part of the interaction potential can induce instabilities in a dipolar gas at the few body level as well as at the many-body level (this latter case will be discussed in section 3). For example, for several experimentally relevant mixed alkali-metal diatomic species such as KRb, LiNa, LiK, LiRb, and LiCs,⁴⁷ there exist chemically reactive channels that are energetically favorable, leading to particle recombination and two-body losses in the gas. The rate of chemical reactions can be strongly enhanced by dipole–dipole interactions which can attract molecules in a *head-to-tail* configuration (e.g., $\theta = 0$ in Figure 1a) to distances on the order of typical chemical interaction distances, $a_c \lesssim 1$ nm.^{48–56} One aim of interaction engineering is to control these interactions in order to stabilize the gas against particle losses. This will enable the study of complex condensed matter phenomena in these systems.

2.2.3. Stabilization of Dipolar Interactions in 2D. The simplest example of stabilization of dipolar interactions against inelastic collisions is sketched in Figure 2 and consists of a system of cold polar molecules in the presence of a polarizing dc electric field oriented in the z -direction and of a strong harmonic transverse confinement $V_{\text{trap}} = \mu\Omega^2 z^2/2$ with frequency Ω and characteristic length $a_h = (\hbar/m\Omega)^{1/2}$. The latter is provided, e.g., by an optical lattice along z .

Figure 3b shows a contour plot of the interaction potential $V(\rho, z)$ for two dipoles in this quasi-2D geometry, where

$$V(\mathbf{r}) = V_{\text{eff}}^{3\text{D}}(\mathbf{r}) + \frac{m\Omega^2 z^2}{4} \\ = -\frac{C_6}{r^6} + \frac{d^2(1 - 3z^2/r^2)}{4\pi\epsilon_0 r^3} + \frac{m\Omega^2 z^2}{4}$$

Here $\vec{\rho} = (\rho, \phi, z)$ represents the distance between the two molecules in cylindrical coordinates, and $r \equiv |\vec{\rho}|$. The first term is the isotropic vdW potential, assuming the molecules are in their rotational ground state, with a vdW length $\bar{a} = (2\pi/\Gamma(1/4)^2)(2\mu C_6/\hbar^2)^{1/4}$.^{58,59} The second term is the anisotropic dipolar potential, with induced dipole moment d and dipolar length a_d .

Figure 3b illustrates essential features of reduced dimensional collisions: for finite d , the repulsive dipole–dipole interaction overcomes the attractive van-der-Waals potential in the ($z = 0$)-plane at distances $r > \bar{a} \gg a_c$, realizing a repulsive in-plane potential barrier (blue dark region). In addition, the harmonic potential confines the particles's motion in the z direction. The combination of the dipole–dipole interaction and of the

harmonic confinement thus yields a *three-dimensional* potential barrier separating the long-distance, where interactions are repulsive, from the short-distance one, where interactions are attractive and inelastic processes can occur. If the collision energy is smaller than the height of the barrier at the saddle point (white circles), the particles' motion is confined to the long-distance region, where particles scatter elastically. Particle losses are due to tunneling through the potential barrier at a rate $K_j^{(\text{re})}$. Within a semiclassical (*instanton*) approximation valid for $a_d \gg \max\{a_h, \bar{a}\}$, the tunneling rate $K_j^{(\text{re})}$ is well approximated by the exponential form

$$K_j^{(\text{re})} \propto \omega_p \exp[-c(a_d/a_h)^{2/5}] \quad (7)$$

The constant c has been recently computed numerically by Julienne, Hanna, and Idziaszek⁶¹ to be $c \approx 3.03$, while the “attempt rate” ω_p ⁶² for the scattering of two isolated dipoles reads $\omega_p \propto (\hbar^2 \kappa^4 a_h^4 / \mu)$, independent of particles' statistics. Here κ is the momentum for a collision with relative kinetic energy $E_\kappa = \hbar^2 \kappa^2 / (2\mu)$, with $a_\kappa = 2\pi/\kappa$ the de Broglie wavelength. For particles in a crystalline configuration (see section 6.1), ω_p will be proportional to the frequency of phonon oscillations around the mean particle positions $\omega_p \sim (d^2/\mu a^5)^{1/2}$, with a the mean interparticle distance. The expression eq 7 shows that collisional losses may be strongly suppressed for *any* molecular species for a large enough dipole moment or strength of transverse confinement.

In ultracold collisions one often has the following separation of length scales: $a_\kappa \gg a_h \gg \bar{a} \gg a_c$, and a_d can be tuned by, e.g., increasing the external dc field. Parts a and b of Figure 4 show

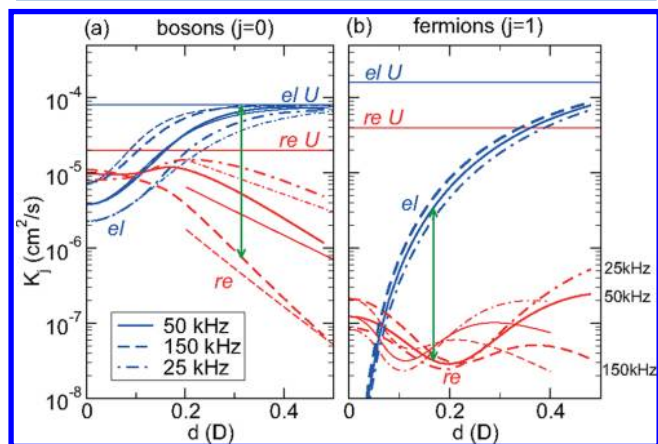


Figure 4. Quasi-2D elastic (el) and reaction (re) rate constants K_j for (a) identical KRb bosons ($j = 0$) and (b) identical KRb fermions ($j = 1$) at a collision energy of $E = k_B(240 \text{ nK}) = h$ (5 kHz) for three different trap frequencies $\Omega/(2\pi) = 25 \text{ kHz}$, 50 kHz, and 150 kHz. Heavy lines: CC. Light lines: UBA or instanton. Horizontal lines show the unitarity limits. Vertical arrows show where $\eta_j = 100$. (From ref 60.)

numerical results for reactive and elastic collision rates of bosonic and fermionic KRb molecules, respectively, and for several strengths of transverse confinement. Here a_κ , a_h , and \bar{a} are on the order of hundreds of nanometers, tens of nanometers, and less than 10 nm, respectively. Because of the moderate $d_{\text{max}} = 0.5$ D of KRb molecules, here $a_d \lesssim a_h$ and the semiclassical regime of large a_d of eq 7 is not reached. Nevertheless, in stark contrast to collisions in 3D,⁵⁰ the figure shows that the ratio between elastic and inelastic collision rates

increases rapidly with d , signaling an increased stability with increasing d . For bosons, the exact numerical results (thick lines) approach rapidly the semiclassical instanton limit (thin lines) with increasing d . The behavior of the inelastic rates for fermions is explained in detail in refs 60 and 63.

Recent landmark experimental results from the JILA group with fermionic KRb molecules show a strong suppression of inelastic collisions and increase of elastic ones with d , in excellent agreement with the predictions of Figure 3. This opens the way to the study of strongly correlated phenomena in these systems.

2.2.4. Advanced Interaction Designing: Blue-Shielding. By combining dc and ac fields to dress the manifold of rotational energy levels, it is possible to design effective interaction potentials $V_{\text{eff}}^{\text{3D}}(\mathbf{r}_i - \mathbf{r}_j)$ with (essentially) any shape as a function of distance. For example, the addition of a single linearly polarized ac field to the configuration of section 2.2.3 leads to the realization of the 2D “steplike” potential of Figure 3a (black dashed-dotted line), where the character of the repulsive potential varies considerably in a small region of space. The derivation of this effective 2D interaction is sketched in Figure 5.^{57,64} The (weak) dc-field splits the first-excited

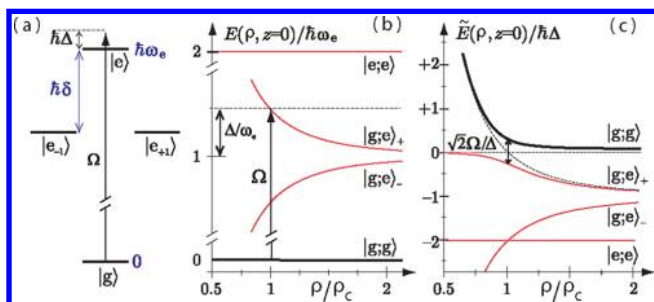


Figure 5. Design of the steplike potential of Figure 3a (black dashed-dotted line): (a) Rotational spectrum of a molecule in a weak dc field. The dc field splits the ($J = 1$)-manifold by an amount $\hbar\delta$. The linearly polarized microwave transition with detuning Δ and Rabi frequency Ω is shown as an arrow. (b) BO-potentials for the internal states for $\Omega = 0$ (bare potentials), where $|g;e_{\pm}\rangle \equiv (|g;e\rangle \pm |e;g\rangle)/\sqrt{2}$. The resonant Condon point ρ_C is indicated by an arrow. (c) ac-field-dressed BO-potentials. The dressed ground state potential has the largest energy.

rotational ($J = 1$)-manifold of each molecule by an amount $\hbar\delta$, while a linearly polarized ac-field with Rabi frequency Ω is blue-detuned from the ($|g\rangle - |e\rangle$)-transition by $\hbar\Delta$; see Figure 5a. Because of $\hbar\delta$ and the choice of polarization, for distances $\rho \gg (d^2/\hbar\delta)^{1/3}$, the relevant single-particle states for the two-body interaction reduce to the states $|g\rangle$ and $|e\rangle$ of each molecule. Figure 5b shows that the dipole–dipole interaction splits the excited state manifold of the two-body rotational spectrum, making the detuning Δ *position-dependent*. As a consequence, the combined energies of the bare ground state of the two-particle spectrum and of a microwave photon become degenerate with the energy of a (symmetric) excited state at a characteristic resonant (Condon) point $\rho_C = (d^2/\hbar\Delta)^{1/3}$, which is represented by an arrow in Figure 5b. At this Condon point, an avoided crossing occurs in a *field-dressed* picture, and the new (dressed) ground state potential inherits the character of the bare ground and excited potentials for distances $\rho \gg \rho_C$ and $\rho \ll \rho_C$, respectively. Figure 5d shows that the dressed ground state potential (which has the *largest energy*) is almost flat for $\rho \gg \rho_C$ and it is strongly repulsive as $1/\rho^3$ for $\rho \ll \rho_C$, which corresponds to the realization of the steplike potential of

Figure 3a. We remark that, due to the choice of polarization, this strong repulsion is present only in the plane $z = 0$, while for $z \neq 0$ the ground state potential can become attractive. The optical confinement along z of section 2.2.3 is therefore necessary to ensure the stability of the system.

The interactions in the presence of a single ac field are described in detail in ref 57, where it is shown that in the absence of external confinement this case is analogous to the (3D) optical blue-shielding developed in the context of ultracold collisions of neutral atoms,^{65–67} however with the advantage of the long lifetime of the excited rotational states of the molecules, as opposed to the electronic states of cold atoms. The strong inelastic losses observed in 3D collisions with cold atoms^{65–67} can be avoided via a judicious choice of the field’s polarization, eventually combined with a tight confinement to ensure a 2D geometry (as e.g. in Figure 2 above). For example, in ref 68 it is shown that in the presence of a dc field and of a circularly polarized ac field the *attractive* time-averaged interaction due to the rotating (ac-induced) dipole moments of the molecules allows for the cancellation of the total dipole–dipole interaction. The residual interactions remaining after this cancellation are *purely repulsive 3D interactions* with a characteristic van-der-Waals behavior $V_{\text{eff}}^{\text{3D}}(\mathbf{r}) \sim (d^4/\hbar\Delta)/r^6$. This 3D repulsion provides for a shielding of the inner part of the interaction potential, and thus, it will strongly suppress inelastic collisions in experiments.

Recent works^{69,70} have considered the microwave spectra of alkali-metal dimers including hyperfine interactions. It is an important open question to determine the effects that the presence of internal states, such as, e.g., hyperfine states, have on the broad class of shielding techniques described above.

3. WEAKLY INTERACTING DIPOLAR BOSE GAS

3.1. BEC in a Spatially Homogeneous Gas

Let us discuss now the influence of the dipole–dipole interaction on the properties of a homogeneous single-component dipolar Bose gas. (This and the next sections are substantially revised and updated versions of the corresponding parts of ref 32.) This can be most conveniently done in the language of second quantization. For this purpose we introduce the particle creation and annihilation field operators $\hat{\psi}^\dagger(\mathbf{r})$ and $\hat{\psi}(\mathbf{r})$ satisfying the standard bosonic commutation relation

$$[\hat{\psi}(\mathbf{r}), \hat{\psi}^\dagger(\mathbf{r}')] \equiv \hat{\psi}(\mathbf{r})\hat{\psi}^\dagger(\mathbf{r}') - \hat{\psi}^\dagger(\mathbf{r}')\hat{\psi}(\mathbf{r}) = \delta(\mathbf{r} - \mathbf{r}')$$

$$[\hat{\psi}(\mathbf{r}), \hat{\psi}(\mathbf{r}')] = [\hat{\psi}^\dagger(\mathbf{r}), \hat{\psi}^\dagger(\mathbf{r}')] = 0$$

The corresponding second quantized Hamiltonian of the system then reads

$$\hat{H} = \int d\mathbf{r} \hat{\psi}^\dagger(\mathbf{r}) \left[-\frac{\hbar^2}{2m} \nabla^2 - \mu \right] \hat{\psi}(\mathbf{r}) + \frac{1}{2} \int d\mathbf{r} d\mathbf{r}' \hat{\psi}^\dagger(\mathbf{r}) \times \hat{\psi}^\dagger(\mathbf{r}') V(\mathbf{r} - \mathbf{r}') \hat{\psi}(\mathbf{r}') \hat{\psi}(\mathbf{r}) \quad (8)$$

where m is the mass of the particles, $V(\mathbf{r})$ is the interparticle interaction, and the chemical potential μ fixes the average density n of the gas. We consider the case when the system is away from any “shape” resonances^{38,39,71} and, therefore, replace the original interparticle interaction with the pseudopotential (eq 2). Assuming that the system is dilute, $na^3 \ll 1$, we can write the Hamiltonian as

$$\hat{H} = \int d\mathbf{r} \hat{\psi}^\dagger(\mathbf{r}) \left[-\frac{\hbar^2}{2m} \nabla^2 - \mu + \frac{1}{2} g |\hat{\psi}(\mathbf{r})|^2 \right] \hat{\psi}(\mathbf{r}) + \frac{1}{2} \int d\mathbf{r} d\mathbf{r}' \hat{\psi}^\dagger(\mathbf{r}) \hat{\psi}^\dagger(\mathbf{r}') V_d(\mathbf{r} - \mathbf{r}') \hat{\psi}(\mathbf{r}') \hat{\psi}(\mathbf{r}) \quad (9)$$

where V_d is given by eq 1 and $g = 4\pi\hbar^2 a/m$ (as compared to eq 3, we omit the dependence of the scattering length a on the dipole moment d). Note that the scattering length has to be positive, $a > 0$, to avoid an absolute instability due to local collapses.⁷²

As we will see below, an important parameter that determines the properties of the system described by the Hamiltonian (eq 9) is

$$\varepsilon_{dd} = \frac{4\pi}{3} \frac{d^2}{g} = \frac{md^2}{3\hbar^2 a} = \frac{1}{3} \frac{a_d}{a} \quad (10)$$

It measures the strength of the dipole–dipole interaction relative to the short-range repulsion. In the case $\varepsilon_{dd} < 1$, the short-range part of the interparticle interaction is dominant while the dipole–dipole interaction results in only small corrections. For a positive scattering length a , the system is stable and exhibits BEC at low temperatures. This case corresponds to earlier experiments^{10,13} with Cr BEC ($\varepsilon_{dd} \approx 0.16^{13}$). It was found that the corrections due to magnetic dipole–dipole interaction between ⁵²Cr atoms are of the order of 10%.

For the opposite case $\varepsilon_{dd} > 1$, the anisotropic dipole–dipole interaction plays the dominant role, resulting in instability of a spatially homogeneous system.^{73–75} This instability can be seen in the dispersion relation $E(\mathbf{p})$ between the energy E and the momentum \mathbf{p} of excitations in the Bose-condensed gas, which can be easily obtained within the standard Bogoliubov approach:

$$E(\mathbf{p}) = \sqrt{\frac{p^2}{2m} \left[\frac{p^2}{2m} + 2nV(\mathbf{p}) \right]} = \frac{p}{2m} \sqrt{p^2 + 4mng[1 + \varepsilon_{dd}(3 \cos^2 \theta - 1)]} \quad (11)$$

Here θ is the angle between the excitation momentum \mathbf{p} and the direction of dipoles, and $V(\mathbf{p}) = g + (4\pi d^2/3)(3 \cos^2 \theta - 1)$ is the Fourier transform of $V(\mathbf{r}) = g\delta(\mathbf{r}) + V_d(\mathbf{r})$. Signatures of the anisotropic behavior of the speed of sound have been recently observed in ref ³⁰⁰. For $\varepsilon_{dd} > 1$, the excitation energies $E(\mathbf{p})$ at small p and θ close to $\pi/2$ become imaginary, signaling the instability (collapse). This instability of a spatially homogeneous dipolar Bose gas with dominant dipole–dipole interaction is a result of a partially attractive nature of the dipole–dipole interaction.

3.2. BEC in a Trapped Gas

The above consideration shows that the behavior of a spatially homogeneous Bose gas with a strong dipole–dipole interaction is similar to that of a Bose gas with an attractive short-range interaction characterized by a negative scattering length $a < 0$. In the latter case, however, the collapse of the gas can be prevented by confining the gas in a trap, provided the number of particles N in the gas is smaller than some critical value N_c , $N < N_c$ (see, e.g., ref 72). This is due to the finite energy difference between the ground and the first excited states in a confined gas. For a small number of particles, this creates an

effective energy barrier preventing the collapse and, therefore, results in a metastable condensate. The same arguments are also applicable to a dipolar BEC in a trap; see refs 15 and 16 with one very important difference: The sign and the value of the dipole–dipole interaction energy in a trapped dipolar BEC depend on the trapping geometry, and therefore, the stability diagram contains the trap anisotropy as a crucial parameter.

3.2.1. Ground State. The Hamiltonian for a trapped dipolar Bose gas reads

$$\hat{H} = \int d\mathbf{r} \hat{\psi}^\dagger(\mathbf{r}) \left[-\frac{\hbar}{2m} \nabla^2 - \mu + U_{tr}(\mathbf{r}) + \frac{1}{2} g |\hat{\psi}(\mathbf{r})|^2 \right] \hat{\psi}(\mathbf{r}) + \frac{1}{2} \int d\mathbf{r} d\mathbf{r}' \hat{\psi}^\dagger(\mathbf{r}) \hat{\psi}^\dagger(\mathbf{r}') V_d(\mathbf{r} - \mathbf{r}') \hat{\psi}(\mathbf{r}') \hat{\psi}(\mathbf{r}) \quad (12)$$

where

$$U_{tr}(\mathbf{r}) = \frac{m}{2} [\omega_\rho^2(x^2 + y^2) + \omega_z^2 z^2] \quad (13)$$

is the trapping potential and we again use the pseudopotential (eq 2) for the short-range part of the interparticle interaction assuming that the system is away from “shape” resonances. For the trapping potential, we consider the experimentally most common case of an axially symmetric harmonic trap characterized by the axial ω_z and radial ω_ρ trap frequencies. The aspect ratio of the trap l is defined through the ratio of the frequencies: $l = (\omega_\rho/\omega_z)^{1/2} = l_z/l_\rho$, where $l_z = (\hbar/m\omega_z)^{1/2}$ and $l_\rho = (\hbar/m\omega_\rho)^{1/2}$ are the axial and radial sizes of the ground state wave function in the harmonic oscillator potential (eq 13), respectively. For $l < 1$, one has a pancake-form (oblate) trap, while the opposite case $l > 1$ corresponds to a cigar-form (prolate) trap. Taking into account the anisotropy of the dipole–dipole interaction, one can easily see that the aspect ratio l should play a very important role in the behavior of the system.

The standard mean-field approximation corresponds to taking the many-body wave function in the form of a product of single-particle wave functions:

$$\Psi(\mathbf{r}_1, \dots, \mathbf{r}_N; t) = \prod_{j=1}^N \psi_j(\mathbf{r}_j, t) \quad (14)$$

The condensate is then described by the condensate wave function $\psi(\mathbf{r}, t) = \sqrt{N}\psi_1(\mathbf{r}, t)$ normalized to the total number of particles, $\int d\mathbf{r} |\psi(\mathbf{r}, t)|^2 = N$, and governed by the time-dependent Gross–Pitaevskii (GP) equation

$$i\hbar \frac{\partial}{\partial t} \psi(\mathbf{r}, t) = \left[-\frac{\hbar^2}{2m} \nabla^2 - \mu + U_{tr}(\mathbf{r}) + g |\psi(\mathbf{r}, t)|^2 + d^2 \int d\mathbf{r}' \frac{1 - 3 \cos^2 \theta}{|\mathbf{r} - \mathbf{r}'|^3} |\psi(\mathbf{r}', t)|^2 \right] \psi(\mathbf{r}, t) \quad (15)$$

The validity of this approach was tested in refs 41 and 44 by using many-body diffusion Monte Carlo calculations with the conclusion that a GP equation with the pseudopotential (eq 2) provides a correct description of the gas in the dilute limit $na^3 \ll 1$. Note that, being the product of single-particle wave functions, the many-body wave function (eq 14) does not take into account interparticle correlations at short distances due to their interaction, which takes place at interparticle distances $|\mathbf{r} - \mathbf{r}'| \lesssim a_d = md^2/\hbar^2$. This change of the wave function is taken

into account in eq 15 by the contact part of the pseudopotential (eq 2) [the fourth term on the right-hand-side of eq 15] but ignored in the last term of eq 15 because the main contribution to the integral comes from large interparticle distances (of order the spatial size of the condensate).

Let us first consider stationary solutions of eq 15, for which $\psi(\mathbf{r}, t) = \psi_0(\mathbf{r})$ and $\psi_0(\mathbf{r})$ obeys the stationary GP equation

$$\left[-\frac{\hbar^2}{2m}\nabla^2 + \frac{m}{2}(\omega_\rho^2\rho^2 + \omega_z^2z^2) + g|\psi(\mathbf{r}, t)|^2 + d^2 \int d\mathbf{r}' \frac{1 - 3\cos^2\theta}{|\mathbf{r} - \mathbf{r}'|^3} |\psi_0(\mathbf{r}')|^2 \right] \psi_0(\mathbf{r}) = \mu\psi_0(\mathbf{r}) \quad (16)$$

where $\rho^2 = x^2 + y^2$. Numerical analysis of eqs 15 and 16 was performed in refs 40, 73, 74, 76, and 77 on the basis of numerical solutions of the nonlinear Schrödinger equation (eq 16) together with variational considerations with the Gaussian ansatz for the condensate wave function. In refs 41 and 44 the problem was treated using diffusive Monte Carlo calculations, while the authors of ref 78 apply the Thomas–Fermi approximation that neglects the kinetic energy and allows obtaining of analytical results.

We begin the discussion of the results with the case of a dominant dipole–dipole interaction, $\varepsilon_{dd} \gg 1$, such that the third term on the left-hand-side of eq 16 can be neglected. This case demonstrates already all important features of the behavior of dipolar condensates. The general case will be briefly discussed at the end of this section.

Let us introduce the mean-field dipole–dipole interaction energy per particle

$$V = \frac{1}{N} \int d\mathbf{r} d\mathbf{r}' |\psi_0(\mathbf{r})|^2 \frac{1 - 3\cos^2\theta}{|\mathbf{r} - \mathbf{r}'|^3} |\psi_0(\mathbf{r}')|^2 \quad (17)$$

which together with the trap frequencies ω_z and ω_ρ are important energy scales of the problem. One can easily see that the value of the chemical potential μ and the behavior of the dipolar condensate are determined by the aspect ratio of the trap l , the quantity $V/\hbar\omega_\rho$, and the parameter $\sigma = Na_d/l\rho$. Notice also that the anisotropy of the dipole–dipole interaction results in squeezing the cloud in the radial direction and stretches it in the axial one (along the direction of dipoles) in order to lower the interaction energy. For this reason, the aspect ratio of the cloud $L = L_z/L_\rho$ is always larger than the aspect ratio l of the trap. Here L_z and L_ρ are the axial and the radial sizes of the cloud, respectively.

We now summarize the results of the stability analysis of the dipolar condensate with $\varepsilon_{dd} \gg 1$ (eq 16 with $g = 0$)^{74,76,79} (see also ref 77 for the stability analysis in a general harmonic trap). The mean-field dipole–dipole interaction is always attractive, $V < 0$, for a cigar shaped trap $l \geq 1$, causing instability (collapse) of the gas if the particle number N exceeds a critical value N_c . This critical value depends only on the trap aspect ratio l . It was found that the shape of the cloud with N close to N_c is approximately Gaussian with the aspect ratio $L \approx 2.1$ for a spherical trap ($l = 1$) and $L \approx 3.0$ for an elongated trap with $l \gg 1$.

For a pancake shaped trap with $l \leq 1$, the situation is more subtle. In this case, there exists a critical trap aspect ratio $l_* \approx 0.43$, which splits the pancake shaped traps into soft pancake traps ($l_* < l \leq 1$) and hard pancake traps ($l < l_*$). For soft

pancake traps, one has again a critical number of particles N_c such that the condensates with $N > N_c$ are unstable. For N close to N_c and $l \rightarrow l_*$, the aspect ratio of the cloud L_c approaches the aspect ratio of the trap, $L_c \rightarrow l_*$. Note that in this case the collapse occurs even in a pancake shaped cloud with positive mean dipole–dipole interaction V due to the behavior of the lowest quadrupole and monopole excitations (see section 3.2.2).

For hard pancake traps, it was argued in refs 74 and 76 that the dipolar condensate is stable for any N because the dipole–dipole interaction energy V is always positive. On the other hand, by using more advanced numerical analysis and a larger set of possible trial condensate wave functions, the authors of ref 79 found that the dipolar condensate in a hard pancake trap is also unstable for a sufficiently large number of particles. Similar conclusions were drawn in ref 77. It was found that the critical values of the parameter σ for the instability to occur are orders of magnitude larger than in soft pancake and cigar shaped traps. In addition, the regions in parameter space were discovered where the maximum density of the condensate is not in the center of the cloud such that the condensate has a biconcave shape. (Analogous behavior of the condensate in a general three-dimensional harmonic trap was found in ref 77; see also refs 80 and 81.) These regions exist also in the presence of a small contact interaction with $|a| \lesssim 0.2a_d$, but their exact position and size depend on a . It is important to mention that condensates with normal and biconcave shapes behave differently when the instability boundary is crossed. The condensate with a normal shape develops a modulation of the condensate density in the radial direction, so-called “radial roton” instability, similar to the roton instability for the infinite-pancake trap ($l \rightarrow \infty$);⁸² see section 3.2.3. On the other hand, it is the density modulations in the angular coordinate that lead to the collapse of biconcave condensates—a kind of “angular roton” instability in the trap. In the latter case, one has spontaneously broken cylindrical symmetry.

The behavior of the trapped dipolar condensate can be simply captured by means of a Gaussian variational ansatz for the condensate wave function $\psi_0(\mathbf{r})$:

$$\psi_0(\mathbf{r}) = \sqrt{\frac{N}{\pi^{3/2}L_\rho^2L_z}} \exp\left(-\frac{\rho^2}{2L_\rho^2} - \frac{z^2}{2L_z^2}\right) \quad (18)$$

where the equilibrium radial size L_ρ and the cloud aspect ratio L can be found by minimizing the energy. Note that in order to describe biconcave shaped condensates, one has to consider (see ref 79) a linear combination of two wave functions: the first one is a Gaussian (eq 18), and the second one is the same Gaussian multiplied by $H_2(x/L_\rho) + H_2(y/L_\rho)$, where H_2 is the Hermite polynomial of the second order.

For large values of the parameters Na/l , where $i = \rho$ or z , are large (but still $Na^3 \ll 1$), one can use the Thomas–Fermi approximation to find the chemical potential and the shape of the cloud.⁷⁸ This case corresponds to small kinetic energy, as compared to other energies, and therefore, we can neglect the corresponding term with derivatives in eq 16. The GP equation then becomes

$$\begin{aligned} & \left[\frac{m}{2}(\omega_\rho^2 \rho^2 + \omega_z^2 z^2) + \frac{1}{2}g|\psi(\mathbf{r}, t)|^2 \right. \\ & \quad \left. + d^2 \int d\mathbf{r}' \frac{1 - 3 \cos^2 \theta}{|\mathbf{r} - \mathbf{r}'|^3} |\psi_0(\mathbf{r}')|^2 \right] \psi_0(\mathbf{r}) \\ & = \mu \psi_0(\mathbf{r}) \end{aligned} \quad (19)$$

The solution of this equation reads

$$\psi_0^2(\mathbf{r}) = n(\mathbf{r}) = n_0 \left(1 - \frac{\rho^2}{R_\rho^2} - \frac{z^2}{R_z^2} \right)$$

with the chemical potential

$$\mu = gn_0[1 - 3\epsilon_{dd}F(L)]$$

where n_0 is the density of the condensate in the center of the trap and

$$F(L) = \frac{1}{3} - \frac{G(L) - 1}{L^2 - 1} \quad (20)$$

The energy of the condensate is

$$E = \frac{1}{14}Nm\omega_\rho^2 R_\rho^2 \left(2 + \frac{L^2}{l^4} \right) + \frac{15}{28\pi} \frac{N^2}{R_\rho^2 R_z} g[1 - 3\epsilon_{dd}F(L)] \quad (21)$$

and the radii of the condensate in the radial and axial directions R_ρ and R_z are

$$R_\rho = \left\{ \frac{15gN}{4\pi m\omega_\rho^2 L} \left[1 + \epsilon_{dd} \left(\frac{9}{2} \frac{F(L)}{L^2 - 1} - 1 \right) \right] \right\}^{1/5} \quad (22)$$

$$R_z = LR_\rho \quad (23)$$

and the corresponding aspect ratio of the cloud L can be found from the equation

$$3\epsilon_{dd} \left[3 \left(\frac{1}{2l^4} + 1 \right) \frac{L^2 F(L)}{L^2 - 1} - 1 \right] + (\epsilon_{dd} - 1) \left(1 - \frac{L^2}{l^4} \right) = 0 \quad (24)$$

Note that the above equation coincides with the equation on the aspect ratio for the Gaussian variational ansatz (eq 18) when the kinetic energy contribution is neglected, as shown in ref 73. It was also found that the Thomas–Fermi approximation agrees well with numerical results when used to analyze the stability of the condensate. However, the critical number of particles cannot be found in the Thomas–Fermi approximation because both terms in the expression (eq 21) for the energy have the same dependence $N^{7/5}$ on the number of particles N after taking into account the expressions (eqs 22 and 23) for R_ρ and R_z .

Let us now briefly discuss the stability of a dipolar condensate in the general case with $g \neq 0$. It is obvious that for an attractive short-range interaction with $g < 0$ the condensate can only be (meta)stable for a small number of particles. For a repulsive short-range interaction with $g > 0$ and weak dipole–dipole interaction $0 \leq \epsilon_{dd} < 1$, the condensate is always stable. For $\epsilon_{dd} > 1$ the dipolar condensate can only be metastable for a number of particles smaller than a critical value, $N < N_c$, which depends on ϵ_{dd} and the trap aspect ratio l . This means that the (metastable)condensate solution provides only a local minimum of the energy, while the global minimum

presumably corresponds to a collapsed state with $L \rightarrow \infty$ or, for $l < 1$, a kind of density modulated state.

3.2.2. Collective Excitations and Instability. We have already mentioned that collective excitations play an important role in the stability analysis of a dipolar condensate. They also determine the dynamics of the gas and, therefore, are of experimental interest.

For a trapped dipolar condensate, the analysis of excitations is usually performed on the basis of the Bogoliubov–de Gennes equations, which can be obtained by linearizing the time-dependent GP equation (eq 15) around the stationary solution $\psi_0(\mathbf{r})$. This can be achieved by writing a solution of eq 15 in the form

$$\psi(\mathbf{r}, t) = \psi_0(\mathbf{r}) + \epsilon[u(\mathbf{r}) \exp(-i\omega t) + v^*(\mathbf{r}) \exp(-i\omega t)]$$

where the second term describes small ($\epsilon \ll 1$) oscillations of the condensate around $\psi_0(\mathbf{r})$ with (complex) amplitudes $u(\mathbf{r})$ and $v(\mathbf{r})$. To the first order in ϵ , the linearization of eq 15 gives the Bogoliubov–de Gennes equations

$$\begin{aligned} \hbar\omega u(\mathbf{r}) &= \left[-\frac{\hbar^2}{2m}\nabla^2 - \mu + U_r(\mathbf{r}) + 2 \int d\mathbf{r}' \right. \\ & \quad \left. V(\mathbf{r} - \mathbf{r}')|\psi_0(\mathbf{r}')|^2 \right] u(\mathbf{r}) + \int d\mathbf{r}' \\ & \quad V(\mathbf{r} - \mathbf{r}')|\psi_0(\mathbf{r}')|^2 v(\mathbf{r}) \end{aligned} \quad (25)$$

$$\begin{aligned} -\hbar\omega v(\mathbf{r}) &= \left[-\frac{\hbar^2}{2m}\nabla^2 - \mu + U_r(\mathbf{r}) + 2 \int d\mathbf{r}' \right. \\ & \quad \left. V(\mathbf{r} - \mathbf{r}')|\psi_0(\mathbf{r}')|^2 \right] v(\mathbf{r}) + \int d\mathbf{r}' \\ & \quad V(\mathbf{r} - \mathbf{r}')|\psi_0(\mathbf{r}')|^2 u(\mathbf{r}) \end{aligned} \quad (26)$$

where $V(\mathbf{r} - \mathbf{r}')$ is given by eq 2. The solution of these linear equations provides the eigenfunctions ($u_j(\mathbf{r}), v_j(\mathbf{r})$) with the amplitudes $u_j(\mathbf{r})$ and $v_j(\mathbf{r})$ obeying the normalization condition

$$\int d\mathbf{r} [u_i^*(\mathbf{r}) u_j(\mathbf{r}) - v_i^*(\mathbf{r}) v_j(\mathbf{r})] = \delta_{ij}$$

and the corresponding eigenfrequencies ω_j of the collective modes. The Bogoliubov–de Gennes equations (eqs 25 and 26) can also be obtained by diagonalizing the Hamiltonian equation (eq 13) in the Bogoliubov approximation, which corresponds to splitting the field operator $\hat{\psi}(\mathbf{r})$ into its mean-field value $\psi_0(\mathbf{r})$ and the fluctuating quantum part expressed in terms of annihilation and creation operators $\hat{\alpha}_j$ and $\hat{\alpha}_j^\dagger$ of bosonic quasiparticles (quanta of excitations):

$$\hat{\psi}(\mathbf{r}) = \psi_0(\mathbf{r}) + \sum_j [u_j(\mathbf{r})\hat{\alpha}_j + v_j^*(\mathbf{r})\hat{\alpha}_j^\dagger]$$

The normalization condition for the amplitudes $u_j(\mathbf{r})$ and $v_j(\mathbf{r})$ ensures the bosonic nature of the excitations: The operators $\hat{\alpha}_j$ and $\hat{\alpha}_j^\dagger$ obey the canonical Bose commutation relations.

Nonlocality of the dipole–dipole interaction results in an integrodifferential character of the Bogoliubov–de Gennes equations (eqs 25 and 26), making it hard to analyze them both analytically and numerically. A simpler way is to study the spectrum of small perturbations around the ground state solution of the time-dependent GP eq 15 (see ref 83 for this approach to atomic condensates). Using this approach in

combination with the Gaussian variational ansatz^{73,84} or the Thomas–Fermi approximation,⁸⁵ it is possible to obtain analytic results for several low energy excitation modes.

As an illustration, let us consider a Gaussian variational wave function

$$y(\mathbf{r}, t) = A(t) \prod_{\eta=x,y,z} \exp \left\{ -\frac{[\eta - \eta_0(t)]^2}{2R_\eta^2(t)} + i\eta\alpha_\eta(t) + i\eta^2\beta_\eta(t) \right\} \quad (27)$$

The variational parameters here are the complex amplitude A , the widths R_η , the coordinates of the center of the cloud η_0 , and the quantities α_η and β_η related to the slope and the curvature, respectively. The normalization of the wave function to the total number of particles N provides the constraint

$$N = \pi^{3/2} |A(t)|^2 R_x R_y R_z = \text{const} \quad (28)$$

To find the equations governing the variational parameters, we notice that the time-dependent GP equations (eq 15) are equivalent to the Euler–Lagrange equations for the action

$$S = \int dt L \quad (29)$$

with the Lagrangian

$$L = \int d\mathbf{r} \left\{ \frac{i\hbar}{2} \left[\psi^* \frac{\partial \psi}{\partial t} - \psi \frac{\partial \psi^*}{\partial t} \right] - \frac{\hbar^2}{2m} |\nabla \psi|^2 + [\mu - U_{\text{tr}}(\mathbf{r})] |\psi|^2 \right\} - \frac{1}{2} \int d\mathbf{r} d\mathbf{r}' |\psi(\mathbf{r})|^2 V(\mathbf{r} - \mathbf{r}') \times |\psi(\mathbf{r}')|^2$$

We therefore can obtain an effective Lagrangian L_{eff} that depends on the variational parameters by inserting eq 28 into the previous equation and integrating over space coordinates. We obtain

$$L_{\text{eff}} = -\hbar N \dot{\varphi} - \frac{N}{2} \sum_{\eta} \left[\frac{\hbar^2}{2m R_\eta^2} + \left(\hbar \dot{\beta}_\eta + \frac{2\hbar^2 \beta_\eta^2}{m} + \frac{m\omega_\eta^2}{2} \right) R_\eta^2 \right] - \frac{N^2}{4\sqrt{2}\pi^{3/2} R_x R_y R_z} \times \left[g + d^2 \int d\mathbf{r} \exp \left(-\sum_{\eta} \frac{\eta^2}{2R_\eta^2} \right) \frac{1 - 3 \cos^2 \theta}{r^3} \right] \quad (30)$$

where φ is the phase of A [the modulus of A was excluded by using eq 28] and we set $\eta_0(t) = 0$ and $\alpha_\eta(t) = 0$ for simplicity (this corresponds to ignoring the so-called sloshing motion of the condensate). The standard Euler–Lagrange variational procedure

$$\frac{d}{dt} \left(\frac{\partial L}{\partial \dot{q}_j} \right) - \frac{\partial L}{\partial q_j} = 0$$

with $q_j = (R_\eta, \beta_\eta)$ provides equations of motion for the parameters R_η and β_η :

$$\dot{\beta}_\eta = \frac{m\dot{R}_\eta}{2\hbar R_\eta}$$

and

$$\ddot{R}_\eta + \frac{\partial}{\partial R_\eta} U(R) = 0 \quad (31)$$

The above equation describes the motion of a particle with a unit mass in the potential

$$U(R) = \sum_{\eta} \left(\frac{\hbar^2}{2m^2 R_\eta^2} + \frac{\omega_\eta^2 R_\eta^2}{2} \right) + \frac{N}{4\sqrt{2}\pi^{3/2} R_x R_y R_z} \times \left[g + d^2 \int d\mathbf{r} \exp \left(-\sum_{\eta} \frac{\eta^2}{2R_\eta^2} \right) \frac{1 - 3 \cos^2 \theta}{r^3} \right] \quad (32)$$

Therefore, the frequencies of small amplitude oscillations around the stationary solution can be read from the second derivatives of the potential $U(R)$ at its minimum. In this way one can obtain the frequencies for the first three compressional excitation modes. In refs 73 and 84, these frequencies and the corresponding shapes of the cloud oscillations were found for a cylindrical symmetric trap, $R_x = R_y = R_\rho$, $R_z = LR_\rho$; see Figure 6.

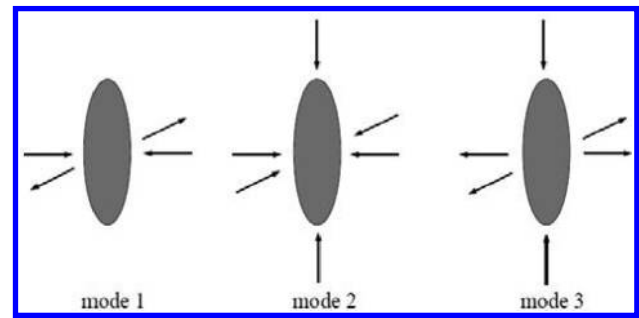


Figure 6. Low-energy excitation modes of a dipolar condensate.

In the considered cylindrical geometry with dipoles oriented along the z -axis, the projection M of the angular momentum on the z -axis is a good quantum number that can characterize the mode: One has $M = 0$ for modes 2 and 3 and $M = 1$ for mode 1. Modes 2 and 3 are often called breathing and quadrupole modes, respectively, and we will follow this convention here. (In the Thomas–Fermi approximation, one can find analytical expressions for these modes; see ref 85.) It is important that, with increasing strength of the dipole–dipole interaction, the quadrupole mode 3 demonstrates the tendency toward instability, and it becomes unstable when ε_{dd} reaches some critical value. This character of instability via softening of mode 2 is similar to that in a Bose gas with a short-range attractive interaction ($a < 0$).

The situation for a dipolar gas with dominant dipole interactions is more complicated.^{79,84,86} It was found (see ref 84) that the instability of collective modes of a dipolar BEC is reminiscent of a gas with an attractive short-range interaction only if the trap aspect ratio is larger than the critical one, $l \gg l_*$ (numerically was found $l > 1.29$): The lowest frequency “breathing” mode 2 becomes unstable when the parameter $\sigma = Na_d/l_\rho \rightarrow \sigma_c$. The variational approach discussed above provides the scaling behavior of its frequency ω_2 near the critical point

(see ref 84): $\omega_2 \sim (\sigma_c - \sigma)^\beta$, with $\beta = 1/4$, which is very close to the experimental value $\beta \approx 0.2$ for Chromium BEC.¹⁵

For intermediate values of l above l_* ($0.75 < l < 1.29$), the mode which drives the instability (the lowest frequency mode) is a superposition of breathing and quadrupole modes with the exponent β still close to $1/4$. The mode has the breathing symmetry (mode 2) for σ far below σ_c , while it changes and becomes quadrupole-like (mode 3) as σ approaches the critical value σ_c .

For l close to l_* ($l < 0.75$) the lowest frequency is the quadrupole mode 3. The frequency of this mode ω_3 tends to zero as σ approaches the critical value, $\omega_3 \sim (\sigma_c - \sigma)^\beta$, with the exponent $\beta \approx 1/4$ if l is not too close to l_* . When l approaches l_* , one has $\sigma_c \rightarrow \infty$, and $\beta > 1/4$. Finally, when $l = l_*$, the frequency of the lowest frequency quadrupole mode ω_3 can be zero only for $\sigma = \infty$.⁸⁶ (Note that this result cannot be reproduced within the Gaussian variational ansatz, which in general does not provide reliable results close to the instability; see ref 84.)

Collective modes for the case $l < l_*$ were analyzed in ref 79 on the basis of the Bogoliubov–de Gennes equations (eqs 25 and 26). The two possible types of solutions for the stable condensate were already mentioned above: A pancake (normal) shaped condensate (the maximum condensate density is in the center of the trap), and a biconcave shaped condensate (the maximum condensate density is at some distance from the center of the trap). It was found that, in the case of a pancake condensate, the mode which drives the instability has zero projection of angular momentum on the z -axis, $M = 0$, and consists of a radial nodal pattern. The number of the nodal surfaces increases with decreasing l (flattening of the condensate). This “radial roton” mode in a confined gas can be viewed as an analog of the roton mode in an infinite-pancake trap from ref 82; see below. In a biconcave condensate near the instability, the lowest frequency mode has nonzero projection of the angular momentum on the z -axis, $M \neq 0$. This mode is an “angular roton” in the trap: For a biconcave-shaped condensate, the maximum density is along the ring, and an angular roton corresponds to density modulation along this ring. The instability in this case corresponds to the collapse of the condensate due to buckling of the density in the angular coordinate and, therefore, breaks the cylindrical symmetry spontaneously (see ref 79 for more details).

3.2.3. Roton Instability of a Quasi 2D Dipolar Condensate. Let us now discuss the effects of the long-range and anisotropic character of dipole–dipole forces in the physically simpler case of an infinite pancake shaped trap, with the dipoles perpendicular to the trap plane.⁸² It was found that a condensate with a large density n_0 can be dynamically stable only when a sufficiently strong short-range repulsive interaction is present. Otherwise, excitations with the certain in-plane momenta q become unstable when the condensate density n_0 exceeds the critical value n_c . Interestingly, the excitation spectrum of a stable condensate with the density $n_0 < n_c$ has a roton–Maxon form similar to that in the superfluid helium (see also ref 87 for the quasi-2D version of this problem).

The time-dependent GP equation for the condensate wave function $\psi(\mathbf{r}, t)$ of dipolar particles harmonically confined in the direction of the dipoles (z -axis) reads

$$i\hbar \frac{\partial}{\partial t} \psi(\mathbf{r}, t) = \left[-\frac{\hbar^2}{2m} \nabla^2 - \mu + \frac{m\omega_z^2 z^2}{2} + g |\psi(\mathbf{r}, t)|^2 + \int d\mathbf{r}' V_d(\mathbf{r} - \mathbf{r}') |\psi(\mathbf{r}', t)|^2 \right] \psi(\mathbf{r}, t) \quad (33)$$

where ω_z is the confining frequency. Let us assume the ground state to be uniform in the in-plane directions such that the ground state wave function $\psi_0(z)$ is independent of the in-plane coordinate $\mathbf{r} = (x, y)$. We can then integrate over \mathbf{r}' in the dipole–dipole term of eq 33 with the result

$$\left[-\frac{\hbar^2}{2m} \frac{d^2}{dz^2} + \frac{m\omega_z^2 z^2}{2} + (g + g_d) \psi_0^2(z) - \mu \right] \psi_0(z) = 0 \quad (34)$$

where $g_d = 8\pi d^2/3$. This one-dimensional equation is similar to the GP equation for short-range interactions. The simplest case corresponds to $g + g_d > 0$, where the chemical potential μ is always positive. Let us consider the case $\mu \gg \hbar\omega_z$ (large condensate density) such that we can use the Thomas–Fermi approximation to find the condensate density profile in the confined direction:

$$n_0(z) = \psi_0^2(z) = n_0(1 - z^2/L^2)$$

where $n_0 = \mu/(g + g_d)$ is the condensate maximum density and $L = (2\mu/m\omega_z^2)^{1/2}$ is the Thomas–Fermi size.

Equation 33 can now be linearized around the ground state solution $\psi_0(z)$ to obtain the Bogoliubov–de Gennes equations for the excitations. These equations are eqs 25 and 26 with $U_{\text{tr}}(\mathbf{r}) = m\omega_z^2 z^2/2$ and $\psi_0(\mathbf{r}) = \psi_0(z)$. Having translational symmetry in the in-plane directions, we can characterize the solutions of these equations by the momentum \mathbf{q} of the in-plane free motion. In addition to \mathbf{q} , we also have an integer quantum number $j \geq 0$ related to the motion in the z -direction such that the amplitudes $\{u(\mathbf{r}), v(\mathbf{r})\}$ have the form $\{u(z), v(z)\} \exp(i\mathbf{q}\rho)$. After introducing the new functions $f_{\pm} = u \pm v$, the Bogoliubov–de Gennes equations read⁸²

$$\omega f_- = H_{\text{kin}} f_+ \quad (35)$$

$$\omega f_+ = H_{\text{kin}} f_- + H_{\text{int}}[f_-] \quad (36)$$

where

$$H_{\text{kin}} = \frac{\hbar^2}{2m} \left[-\frac{d^2}{dz^2} + q^2 + \frac{\Delta\psi_0}{\psi_0} \right]$$

is the kinetic energy operator and

$$H_{\text{int}}[f_-] = 2(g + g_d) \psi_0^2(z) f_-(z) - \frac{3}{2} g g_d \psi_0(z) \int_{-\infty}^{\infty} dz' \psi_0(z') \times \exp(-q|z - z'|) f_-(z') \quad (37)$$

is the interaction operator. The solution of the above equations provides excitation frequencies $\omega_j(q)$ which depend on both j and \mathbf{q} . The most relevant for the stability analysis is the lowest frequency branch $\omega_0(q)$, for which the confined motion is not excited in the limit $q \rightarrow 0$.

Because of the nonlocality of the dipole–dipole interaction, an effective coupling (the last term in eq 37) becomes

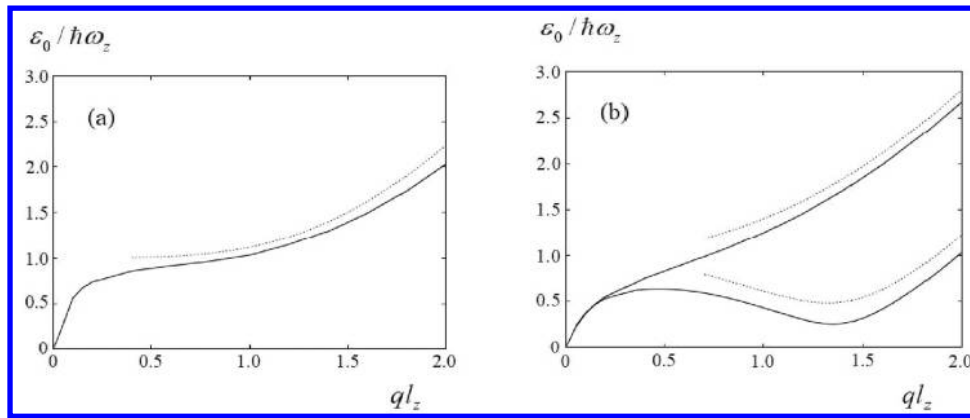


Figure 7. Dispersion law $\omega_0(q)$ for (a) $\beta = 1/2$, $\mu/\hbar\omega_z = 343$; (b) $\beta = 0.53$, $\mu/\hbar\omega_z = 46$ (upper curve) and $\beta = 0.47$, $\mu/\hbar\omega_z = 54$ (lower curve). The solid curves show numerical results. (Taken from ref 82. Copyright 2003 American Physical Society.)

momentum dependent. For small in-plane momenta $qL \ll 1$, excitations of the lowest branch are essentially two-dimensional with a repulsive effective coupling, and their spectrum has been found in ref 88. These excitations are phonons propagating in the xy -plane with the sound velocity c_s :

$$\omega_0(q) = c_s q, \quad c_s = (2\mu/3m)^{1/2}$$

In the opposite limit of large in-plane momenta $qL \gg 1$, the excitations are three-dimensional and the interaction term is then reduced to

$$H_{\text{int}}[f_-] = (2g - g_d)\psi_0^2(z)f_-(z)$$

Equations 35 and 36 are then equivalent to the Bogoliubov–de Gennes equations for the excitations in a condensate with a short-range interaction with the strength $2g - g_d$. This interaction is repulsive if the parameter $\beta \equiv g/g_d > 1/2$, and all excitation frequencies in this case are real and positive for any in-plane momentum q and condensate density n_0 . In the other case $\beta < 1/2$, the interaction is attractive, resulting in dynamical instability of a condensate with regard to high momentum excitations at a sufficiently large density.

The analysis in the Thomas–Fermi regime of the system of eqs 35 and 36 in the most interesting case $qL \gg 1$ and β close to the critical value $1/2$ was performed in ref 82. It was found that at the critical value $\beta = 1/2$ the momentum dependence of the excitation frequencies is characterized by a plateau (see Figure 7a), and the j -th branch reads

$$\omega_j^2(q) = \varepsilon_q^2 + \hbar^2\omega_z^2[1 + j(j+3)/2], \quad qL \gg 1$$

where $\varepsilon_q = \hbar^2q^2/2m$.

For $\beta \neq 1/2$, the lowest branch of the spectrum is

$$\omega_0^2(q) = \varepsilon_q^2 + \frac{(2\beta - 1)(5 + 2\beta)}{3(1 + \beta)(2 + \beta)}\mu\varepsilon_q + \hbar^2\omega_z^2, \quad qL \gg 1 \quad (38)$$

where the condition $\mu\varepsilon_q|2\beta - 1/(1 + \beta)| \ll \hbar^2\omega_z^2$ was assumed. Equation 38 provides us with two types of behavior of the lowest-frequency mode $\omega_0(q)$. It either monotonously increases with q (see Figure 7b) when $\beta > 1/2$ or has a minimum if $\beta < 1/2$. Combined with the fact that $\omega_0(q)$ grows with q for $qL \ll 1$, the existence of this minimum results in a roton–Maxon character of the spectrum as a whole (see Figure 7b). This type of the excitation spectrum in an infinite pancake trap can be understood as follows: For small in-plane momenta $qL \ll L^{-1}$,

excitations have two-dimensional character and are phonons because the dipoles, being oriented perpendicular to the plane of the trap, repel each. On the other hand, excitations with large momenta $q \gg L^{-1}$ have three-dimensional character, and hence, the repulsion between them is reduced. The excitation frequency therefore decreases with an increase of q , reaches a minimum, and starts to increase again as the excitations continuously enter the single-particle regime.

The roton minimum for β close to $1/2$ found from eq 38 is located at $q = (16\mu\delta/15\hbar\omega_z)^{1/2}/l_z$, where $\delta = 1/2 - \beta$, and $l_z = (\hbar/m\omega_z)^{1/2}$ is the harmonic oscillator length for the confined motion and corresponds to the excitation frequency

$$\omega_{0\text{min}} = \sqrt{\hbar^2\omega_z^2 - (8\mu\delta/15)^2}$$

This minimum becomes deeper with increasing density (chemical potential) or δ , and it reaches zero at $q = \sqrt{2}/l_z$ for $\mu\delta/\omega_z = 15/8$. Excitations for larger values of $\mu\delta/\hbar\omega_z$ have imaginary frequencies for $q \sim l_z^{-1}$, and therefore, the condensate becomes unstable.

Equations 35 and 36 for various values of β and $\mu/\hbar\omega_z$ were solved numerically in ref 82. The results for the excitation spectrum in the Thomas–Fermi regime are shown in Figure 7, demonstrating a good agreement between numerical and analytical approaches.

For non-Thomas–Fermi condensates, the stability does not require as strong a short-range repulsive interaction as in the Thomas–Fermi regime because of a large kinetic energy in the confined direction. The spectrum of excitations in this case also has a roton–Maxon character, although the appearance of the roton minimum and the instability take place at smaller values of β ; see ref 82 for details.

Up to now, a roton–Maxon dispersion was observed only in liquid He with strong interparticle interactions. Dipolar condensate provides the first example of a weakly interacting system with a roton–Maxon excitation spectrum. This spectrum can be controlled and manipulated by changing the density, the strength of the confinement, and the short-range interaction, starting from the Bogoliubov-type spectrum, then creating the roton minimum, and finally reaching the point of instability.

It is important to point out that the existence of the roton minimum with $q \neq 0$ at a given $\beta < 1/2$ for $\mu/\hbar\omega_z$ just below the point of instability is likely to indicate the existence of a new ground state, presumably with a periodic density modulation. This is in contrast to the instability of condensates with

attractive short-range interaction, which is driven by unstable long wavelength excitations resulting in local collapses. In this case, the chemical potential is negative and not bounded from below such that no new ground state exists. In section 6 we will show that the excitation spectrum of a two-dimensional dipolar gas in the strongly interacting regime $n_2 a_d^2 \gtrsim 1$ also has the roton minimum, and the system undergoes a liquid to solid quantum phase transition.

4. WEAKLY INTERACTING DIPOLAR FERMIONIC GAS

In this section we discuss fermionic dipolar gases in the weakly interacting regime. Most of the discussion will be devoted to a single-component (polarized) dipolar gas with only brief mention of some results available for two- and more-component dipolar systems.

The crucial differences in the behavior of many-body fermionic systems as compared to bosonic ones are related to the Pauli principle: identical fermions are not allowed to be in the same quantum state. As a result, the many-body wave function of a single component Fermi gas should be antisymmetric with respect to permutations of the positions of any two particles. In the second quantization, this requires that the field operators $\hat{\psi}(\mathbf{r})$ and $\hat{\psi}^\dagger$ obey the canonical anticommutation relations

$$\begin{aligned} \{\hat{\psi}(\mathbf{r}), \hat{\psi}^\dagger(\mathbf{r}')\} &\equiv \hat{\psi}(\mathbf{r}) \hat{\psi}^\dagger(\mathbf{r}') + \hat{\psi}^\dagger(\mathbf{r}') \hat{\psi}(\mathbf{r}) = \delta(\mathbf{r} - \mathbf{r}') \\ \{\hat{\psi}(\mathbf{r}), \hat{\psi}(\mathbf{r}')\} &= \{\hat{\psi}^\dagger(\mathbf{r}), \hat{\psi}^\dagger(\mathbf{r}')\} = 0 \end{aligned}$$

As a direct consequence, the wave function of a relative motion of two identical fermions is allowed to have components with only odd values, $L = 1, 3, \dots$, of the angular momentum, and vanishes when the interparticle distance tends to zero. Therefore, the low-energy scattering of two identical fermions is insensitive to the short-range part of their interaction and is solely determined by the long-range dipole–dipole part V_d . As a result, for a single-component polarized dipolar Fermi gas, we can omit the contact term in eq 2, and the corresponding Hamiltonian then reads

$$\begin{aligned} \hat{H} &= \int d\mathbf{r} \hat{\psi}(\mathbf{r}) \left[-\frac{\hbar}{2m} \nabla^2 - \mu + U_{\text{tr}}(\mathbf{r}) \right] \hat{\psi}(\mathbf{r}) \\ &+ \frac{1}{2} \int d\mathbf{r} d\mathbf{r}' \hat{\psi}^\dagger(\mathbf{r}) \hat{\psi}^\dagger(\mathbf{r}') \times V_d(\mathbf{r} - \mathbf{r}') \hat{\psi}(\mathbf{r}') \hat{\psi}(\mathbf{r}) \end{aligned} \quad (39)$$

where V_d is given by eq 1 and $U_{\text{tr}}(\mathbf{r})$ is the trapping potential (if present).

Another consequence of the Pauli principle is that the state of a many-body system of fermions at a low temperature T is completely different from that for bosons. The average number of ideal fermions in a quantum state i with the energy ε_i is given by the Fermi–Dirac distribution

$$n(\varepsilon_i) = f_{\text{FD}}(\varepsilon_i) = \frac{1}{\exp[(\varepsilon_i - \mu)/T] + 1}$$

where μ is the chemical potential, which depends on T and, as usual, ensures the fixed total number of particles $N = \sum_i n(\varepsilon_i)$. The ground state ($T = 0$) therefore corresponds to an all quantum state with $\varepsilon_i \leq \mu(T = 0) \equiv \varepsilon_F$ being completely occupied [$n(\varepsilon_i) = 1$], while the states with $\varepsilon_i > \varepsilon_F$ are empty [$n(\varepsilon_i) = 0$]. The energy ε_F is called the Fermi energy and sets the typical energy scale as a many-body system of fermions.

The ground state of an ideal homogeneous Fermi gas with $\varepsilon_p = p^2/2m$ corresponds to the so-called Fermi sphere: All quantum states with momenta p below the Fermi momentum $p_F = (2m\varepsilon_F)^{1/2}$ are occupied, and the states with $p > p_F$ are empty. The states with momentum $p = p_F$ form a surface in the momentum space called the Fermi surface, which separates the filled and empty states. Semiclassical state counting provides the relation between the Fermi momentum p_F and the density n of a single-component homogeneous gas:

$$n = \frac{p_F^3}{6\pi^2 \hbar^3} \quad (40)$$

For a trapped Fermi gas we can establish a similar relation, but between the local Fermi momentum $p_F(\mathbf{r})$ and the local density of the gas $n(\mathbf{r})$,

$$n(\mathbf{r}) = \frac{p_F(\mathbf{r})^3}{6\pi^2 \hbar^3} \quad (41)$$

where

$$p_F(\mathbf{r}) = \sqrt{2m[\mu - U_{\text{tr}}(\mathbf{r})]} \quad (42)$$

provided the chemical potential μ is much larger than the level spacing in the trapping potential $U_{\text{tr}}(\mathbf{r})$. This condition corresponds to a large number of particles N in the trap, most of them occupying high energy states of the trapping potential. The wave functions of these states are quasiclassical (see, for example, ref 89), and the calculation of the gas density results in eq 41, which is the essence of the local-density (Thomas–Fermi) approximation. This approximation is legitimate when the trapping potential changes slowly over distances of the order of the average interparticle separation $n^{-1/3} \sim \hbar/p_F$. For an ideal Fermi gas in a harmonic potential, expression 42 gives

$$\begin{aligned} p_F(\mathbf{r}) &= \sqrt{2m[\mu - U_{\text{tr}}(\mathbf{r})]} \\ &= p_F(0) \sqrt{1 - \frac{x^2}{R_{\text{TF}x}^2} - \frac{y^2}{R_{\text{TF}y}^2} - \frac{z^2}{R_{\text{TF}z}^2}} \end{aligned}$$

where $p_F(0) = (2m\mu)^{1/2}$ is the Fermi momentum in the center of the trap and $R_{\text{TF}\alpha} = (2\mu/m\omega_\alpha^2)^{1/2}$ is the Thomas–Fermi size of the gas cloud in the α -direction. The density of the gas in this approximation, according to eq 41, reads

$$n_{\text{TF}}(\mathbf{r}) = n_0 \left(1 - \frac{x^2}{R_{\text{TF}x}^2} - \frac{y^2}{R_{\text{TF}y}^2} - \frac{z^2}{R_{\text{TF}z}^2} \right)^{3/2} \quad (43)$$

where $n_0 = (2m\mu)^{3/2}/(6\pi^2 \hbar^3)$ is the density in the trap center. The calculation of the total number of particles with the use of the above density distribution relates the chemical potential μ to the total number of particles N and the parameters of the trap:

$$\mu = \hbar \bar{\omega} (6N)^{1/3}$$

where $\bar{\omega} = (\omega_x \omega_y \omega_z)^{1/3}$.

For understanding of the properties of the fermionic systems, it is important to keep in mind that the ground state in the form of a filled Fermi sphere stores a large amount of kinetic energy. This guarantees applicability of the perturbation theory for dilute dipolar systems with $p_F a_d / \hbar \ll 1$. Another consequence is the improved stability of fermionic dipolar

gases, as compared to the bosonic ones, against collapse due to the attractive part of the dipole–dipole interaction. This can be understood as follows: The energy per volume for a homogeneous dipolar Fermi gas with density n and an effectively attractive two-body interaction can be written as

$$\frac{E(n)}{V} = \frac{3}{5}\varepsilon_F n - A d^2 n^2$$

where the first term is the kinetic energy of the filled Fermi sphere and the second term is the interaction energy with some numerical coefficient A of the order unity. The first term scales as $n^{2/3}$ (see eq 40) and provides an energy barrier between states with small n and positive energy and collapsing states with $n \rightarrow \infty$ and negative energy. Therefore, one expects stability against collapse when the system is dilute [$n^{-1/3} \gg a_d$ or, equivalently, $p_F a_d / \hbar \ll 1$] and instability in the dense system with $n^{-1/3} \lesssim a_d$ when the interaction energy becomes comparable to or larger than the kinetic energy. Applying this argument to a trapped single-component dipolar Fermi gas, one expects to have a stable gas for $p_F(0)a_d/\hbar < 1$ or $N^{1/6}a_d/l < 1$, where l is the oscillator length, and we use eq 43 to obtain $N \sim [p_F(0)l/\hbar]^6$. We provide more details on the issue of stability later.

4.1. Effects of Dipole–Dipole Interactions

When considering effects of interparticle interactions in Fermi systems, one has to keep in mind two possible scenarios depending on whether the properties of the system (the ground state and excitations) change continuously or abruptly when interactions are switched on. In the first case, an interacting system is called a normal Fermi liquid (in other words, belongs to the Fermi liquid universality class) and has properties that are very much similar to those of an ideal Fermi gas. Of course, the interaction leads to the appearance of new features (collective modes, for example), which are absent in a noninteracting gas, but for many applications, the system can be considered as an ideal gas of fermionic noninteracting quasiparticles. For weak interparticle interactions, the properties of the interacting system can be obtained with the help of perturbation theory, starting from the noninteracting Fermi gas. In the second scenario, the ground state and excitations of the interacting system are qualitatively different from those of the noninteracting Fermi gas, and a system is in the non-Fermi liquid universality class. This scenario is usually associated with breaking of some symmetries of an ideal gas: phase (or gauge) symmetry in a superfluid Fermi liquid or translational symmetry in a charge-density wave or crystal state. The new ground state cannot be continuously connected with the filled Fermi sphere (ground state of a noninteracting Fermi gas), and therefore, one has to go beyond simple perturbative expansions to describe those states. It is important to mention that one does not necessarily need a strong interaction for the second scenario. For example, even an infinitesimally small attractive interaction results in a superfluid ground state. The smallness of the interaction in this case manifests itself in low (much smaller than T_F) critical temperature, T_c —the temperature above which the superfluid properties disappear and the system returns to a normal Fermi liquid. In contrast, the charge-density wave state requires strong interaction, and this state disappears at temperature comparable to or larger than T_F when the gas is essentially classical.

As we will discuss below, depending on an experimental setup, both scenarios are possible in a polarized dipolar gas: A

3D polarized dipolar gas is in the superfluid state for low temperatures, $T < T_c \ll T_F$, and in the normal state (Fermi liquid) for $T > T_c$. The state of a monolayer of polarized dipoles depends on the temperature and the relative angle between the dipole moments and the motion plane of molecules. For the perpendicular orientation of dipoles, the gas is in the normal state, but starting from some critical tilting angle, it becomes a superfluid at small enough temperatures, $T < T_c$. In both cases, the increase of the strength of the dipole–dipole interaction leads to the instability of the homogeneous state, resulting in a collapse or formation of a density-wave state with broken translational symmetry.

4.2. Normal (Anisotropic) Fermi Liquid State

We begin with a discussion of a normal Fermi liquid state of a dipolar fermi gas, which is a generic state for a fermionic dipolar gas at finite ($T_c < T < T_F$) temperatures, as well as for a purely repulsive (in a monolayer, for example) dipolar gas, in a weakly interacting regime $k_F a_d < 1$. Following the original idea of Landau, an interacting normal Fermi system (Fermi liquid) can be described in terms of fermionic quasiparticles, which can be viewed as particles together with the disturbances they produce in the system due to interactions with other particles (particles surrounded by particle–hole excitations)—dressed particles. In the ground state, the quasiparticles occupy all states with energies smaller than or equal to the chemical potential $\mu \approx \varepsilon_F$, forming a filled Fermi sphere (in a spatially uniform dipolar gas, this corresponds to a deformed Fermi sphere in momentum space due to the anisotropy of the dipole–dipole interaction; see below). Excited states are obtained by moving some quasiparticle from occupied states below μ to empty ones above: creation of particle–hole excitations. The advantage of this description is that weakly excited states correspond to a small number of particle–hole excitations near the Fermi surface and, hence, can be described using the dilute gas approximation. Note that, although we are talking about filled quasiparticle states inside the Fermi sphere, quasiparticles in the Fermi liquid are well-defined only in the vicinity of the Fermi surface where their energies $\varepsilon(\mathbf{p})$ are much larger than the inverse of their lifetimes τ_p due to decay via creation of particle–hole pairs. (In a weakly interacting gas, the quasiparticles are well-defined for all momenta.) This is because the presence of occupied states below the Fermi energy strongly reduces the phase space volume for such processes, and as a result, the lifetime τ_p of the quasiparticle near the Fermi surface in a Fermi liquid is much larger than the corresponding time τ_c in a classical gas with the same interparticle interactions and density, $\tau_p \sim [\varepsilon_F/\varepsilon(\mathbf{p})]^2 \tau_c \gg \tau_c$. But for those quasiparticles, we actually need to describe low-energy excitations of the Fermi system and its behavior at low temperatures and under weak external perturbations.

The change of the quasiparticle distribution δn_p (we assume here a spatially homogeneous gas) results in the change of the energy of the system

$$\delta E = \sum_{\mathbf{p}} [\varepsilon(\mathbf{p}) + \mu] \delta n_{\mathbf{p}} + \frac{1}{2V} \sum_{\mathbf{p}, \mathbf{p}'} f(\mathbf{p}, \mathbf{p}') \delta n_{\mathbf{p}} \delta n_{\mathbf{p}'}, \quad (44)$$

where $\varepsilon(\mathbf{p}) = \delta E / \delta n_{\mathbf{p}}|_{\delta n_{\mathbf{p}'}=0}$ is the quasiparticles energy (counted from the chemical potential μ) and the second term describes the interaction between quasiparticles with $f(\mathbf{p}, \mathbf{p}') = \delta^2 E / \delta n_{\mathbf{p}} \delta n_{\mathbf{p}'}|_{\delta n_{\mathbf{p}''}=0}$ being the Landau f -function, which plays a crucial role in the Fermi-liquid theory, and can be either calculated

perturbatively (if the gas is weakly interacting) or measured experimentally. Note that the function f describes the change of the quasiparticle energy under the change of quasiparticle distribution as a result of their interaction,

$$\delta\varepsilon(\mathbf{p}) = \sum_{\mathbf{p}'} f(\mathbf{p}, \mathbf{p}') \delta n_{\mathbf{p}'},$$

which gives rise to Fermi-liquid corrections and makes possible collective motion of quasiparticles (collective modes) even when collisions between quasiparticles can be neglected.

For states close to the Fermi surface (the boundary between occupied and empty states), the quasiparticle energy has the form

$$\varepsilon(\mathbf{p}) \approx \frac{p_F}{m^*} (p - p_F)$$

where p_F is the Fermi momentum specifying the Fermi surface in momentum space, and m^* is the effective mass. The Fermi momentum p_F is related to the density in the same way as in the ideal gas (eq 40) reflecting the fact that numbers of particles and quasiparticles are equal, while the effective mass m^* can be expressed in terms of the f -function (see, for example, ref 90) The compressibility $\kappa = n^{-2} d\mu/dn$, where $\mu = dE/dn$ is the chemical potential, is another important quantity, which can also be expressed in terms of f -function. For a stable system, one must have $\kappa > 0$. Therefore, the knowledge of the compressibility as a function of system parameters provides us with stability conditions of the system against collapse. The stability of the system against possible deformations $\delta n_{\mathbf{p}}$ of the Fermi surface around its equilibrium form (Pomeranchuk criterion^{91,90}) can be obtained from the requirement that the change of the energy caused by this deformation, (eq 44) is positive. In this way, one can detect instabilities different from collapse, related to the nonuniform change of the Fermi surface.

The f -function determines also collective modes in the Fermi liquid (Landau zero sound), which correspond to a collisionless coherent dynamics of particle–hole excitations. The simplest way to describe zero sound is to use a semiclassical (or Wigner) quasiparticle distribution function $n(\mathbf{r}, \mathbf{p}, t)$, which is the Fourier transform of a single-particle density matrix with respect to the relative coordinate,

$$n(\mathbf{r}, \mathbf{p}, t) = \int d\mathbf{r}' \langle \hat{\psi}^\dagger(\mathbf{r} + \mathbf{r}'/2, t) \hat{\psi}(\mathbf{r} - \mathbf{r}'/2, t) \rangle \times \exp(-i\mathbf{p}\mathbf{r}'/\hbar)$$

and describes the local momentum distribution of particles at position \mathbf{r} . In the ground state of a spatially homogeneous system, $n_0(\mathbf{r}, \mathbf{p}, t) = \theta(p_F - p)$ corresponds to a filled Fermi sphere. For a thermal equilibrium state, the step function $\theta(p_F - p)$ has to be replaced with the Fermi-Dirac distribution, $n_T(\mathbf{r}, \mathbf{p}, t) = [\exp(\varepsilon(\mathbf{p})/T) + 1]^{-1}$. Time evolution of the nonequilibrium distributions $n(\mathbf{r}, \mathbf{p}, t) = n_{\text{eq}}(\mathbf{p}) + \delta n(\mathbf{r}, \mathbf{p}, t)$ is described by the quasiparticle kinetic equation

$$\left(\frac{\partial}{\partial t} + \frac{\partial \varepsilon}{\partial \mathbf{p}} \frac{\partial}{\partial \mathbf{r}} + \frac{\partial \varepsilon}{\partial \mathbf{r}} \frac{\partial}{\partial \mathbf{p}} \right) n(\mathbf{r}, \mathbf{p}, t) = 0 \quad (45)$$

where $\varepsilon = \varepsilon(\mathbf{p}) + \sum_{\mathbf{p}'} f(\mathbf{p}, \mathbf{p}') \delta n(\mathbf{r}, \mathbf{p}, t)$ and the collision integral, which normally appears on the right-hand side, is set to zero assuming low temperatures, as discussed above. The solutions of this equation of the form $\delta n(\mathbf{r}, \mathbf{p}, t) \sim \kappa(\mathbf{p}) \exp[i(\mathbf{k}\mathbf{r} - \omega t)] \ll n_{\text{eq}}(\mathbf{p})$ with $\omega = ck$ and $c > v_F$ are called Landau zero sound

and describe coherent motion of particle–hole pairs: propagation of a deformation of the Fermi surface. Generically, solutions of this kind exist when $f(\mathbf{p}, \mathbf{p}')$ is positive (for more details and exact criteria, see, for example, ref 90). Note that the condition $c > v_F$ separates the zero-sound from the continuum of particle-hole excitations and ensures its long lifetime. In the opposite case, the energy of zero-sound waves would be inside the continuum of particle–hole excitations and, hence, the waves would rapidly decay into incoherent particle–hole excitations (Landau damping).

4.2.1. Anisotropic Fermi Surface and Single-Particle Excitations. Due to anisotropy of the dipole–dipole interaction, the Fermi surface in a dipolar gas is not a sphere any more and the modulus of the Fermi momentum depends on the direction. The effective mass becomes a tensor that can be defined from the relation between the Fermi momentum \mathbf{p}_F and Fermi velocity $\mathbf{v}_F = \partial \varepsilon(\mathbf{p}) / \partial \mathbf{p}|_{\mathbf{p}=\mathbf{p}_F}$, $p_{Fi} = m_{ij}^* v_{Fj}$. This can easily be seen by using the following variational ansatz^{92,93}

$$n(\mathbf{p}) = \theta[p_F^2 - \frac{1}{\alpha}(p_x^2 + p_y^2) - \alpha^2 p_z^2] \quad (46)$$

and the variational parameter α is found by minimizing the total energy of the system with the interaction energy calculated in the Hartree–Fock approximation:

$$\frac{E}{V} = \int \frac{d\mathbf{p}}{(2\pi\hbar)^3} \frac{p^2}{2m} n(\mathbf{p}) - \frac{1}{2} \int \frac{d\mathbf{p} d\mathbf{p}'}{(2\pi\hbar)^6} n(\mathbf{p}) V_d(\mathbf{p} - \mathbf{p}') n(\mathbf{p}') \quad (47)$$

where V is the volume of the system and only exchange (Fock) terms contribute to the dipole–dipole interaction energy because the direct Hartree contribution

$$E_d = \frac{1}{2} \int d\mathbf{r} d\mathbf{r}' n(\mathbf{r}) V_d(\mathbf{r} - \mathbf{r}') n(\mathbf{r}')$$

where $n(\mathbf{r})$ is the gas density, vanishes in a homogeneous gas as a result of angular integrations. It was found that $\beta < 1$ so that the Fermi surface is deformed into a spheroid stretched along the direction of dipoles (prolate spheroid). These findings were supported by microscopic calculations in the spirit of Landau liquid theory in refs 94 and 95. The quasiparticle energy calculated from eq 47 reads

$$\varepsilon(\mathbf{p}) = \frac{p^2}{2m} - \int \frac{d\mathbf{p}'}{(2\pi\hbar)^3} V_d(\mathbf{p} - \mathbf{p}') n(\mathbf{p}') - \mu$$

which corresponds to the following Landau f -function for a spatially homogeneous gas

$$f^{\text{hom}}(\mathbf{p}, \mathbf{p}') = -V_d(\mathbf{p} - \mathbf{p}') \quad (48)$$

with only exchange contribution. Note that the condition of spatial homogeneity of the gas is essential for the validity of eq 48. This is because the Fourier component of the dipole–dipole interaction $V_d(\mathbf{q})$ is nonanalytic for $\mathbf{q} \rightarrow 0$ (the limit depends on the direction \mathbf{q} approaches zero). As a result, the direct (Hartree) contribution vanishes only in the spatial homogeneity gas, in which one has $V_d(\mathbf{q})$ averaged over the direction of \mathbf{q} , which is zero. In an inhomogeneous gas, this is not the case and one also has the contribution of the direct dipole–dipole interaction; see, for example, eq 52, describing spatially inhomogeneous variations of the quasiparticle distribution.

Setting $\varepsilon(\mathbf{p})$ to zero gives the position of the Fermi surface in momentum space $\mathbf{p}_F = n p_F(\mathbf{n})$, where \mathbf{n} is a (radial) unit vector (direction) in momentum space. The chemical potential μ then has to be defined self-consistently from assuming a fixed gas density $n = k_F^3/6\pi^2$:

$$n = \int \frac{d\mathbf{p}}{(2\pi\hbar)^3} \theta[-\varepsilon(\mathbf{p})] = \frac{1}{(2\pi\hbar)^3} \int d\mathbf{n} \int_0^{p_F(\mathbf{n})} p^2 dp$$

For weak interaction one finds⁹⁴

$$p_F(\mathbf{n}) = \hbar k_F \left[1 + \frac{1}{9\pi} a_d k_F (3 \cos^2 \theta_n - 1) \right]$$

where θ_n is the angle between \mathbf{n} and the z -axis. This gives $\beta = 1 - 2a_d k_F/9\pi$. The energy and the chemical potential are

$$\frac{E}{V} = \frac{3}{5} \frac{\hbar^2 k_F^2}{2m} \left[1 - \frac{4}{81\pi^2} (a_d k_F)^2 \right]$$

and

$$\mu = \frac{\hbar^2 k_F^2}{2m} \left[1 - \frac{28}{405\pi^2} (a_d k_F)^2 \right]$$

After expanding the quasiparticle energy in the vicinity of the Fermi surface, $\varepsilon(\mathbf{p}) \approx \mathbf{v}_F(\mathbf{p} - \mathbf{p}_F)$, one finds⁹⁵ that the tensor of the effective mass has only longitudinal $m_L^*(\mathbf{n})$ and transverse $m_T^*(\mathbf{n})$ components:

$$\mathbf{v}_F = \mathbf{n} \frac{p_F(\mathbf{n})}{m_L^*(\mathbf{n})} + \mathbf{e}_\theta \frac{p_F(\mathbf{n})}{m_T^*(\mathbf{n})}$$

where \mathbf{E}_θ is the polar angle unit vector and

$$\frac{m}{m_L^*(\mathbf{n})} = \left[1 - \frac{1}{6\pi} a_d k_F (3 \cos^2 \theta_n - 1) \right]$$

$$\frac{m}{m_T^*(\mathbf{n})} = \frac{1}{3\pi} a_d k_F \sin 2\theta_n$$

Calculations for moderate strengths of the dipole–dipole interactions and finite temperatures were performed in refs 92, 94, and 96 including the trapped case (ref 92), as well as 2D (monolayer) and 1D (tube) gases and a two-component dipolar gas (ref 95). We mention here only some details for a monolayer and refer to these references for more details.

In a 2D dipolar gas (monolayer), when the chemical potential μ is much smaller than the frequency ω_z of the transverse confining potential in the z -direction, $\mu \ll \omega_z$, the transverse wave function of particles is limited to the ground state wave function $\phi_0(z)$ of the harmonic oscillator, such that $\psi(\mathbf{r}) = \psi(\rho) \phi_0(z)$, where $\rho = (x, y) = (\rho \cos \phi_\rho, \rho \sin \phi_\rho)$ is the in-plane vector. The corresponding effective 2D dipole–dipole interaction for the in-plane motion

$$\begin{aligned} V_d^{2D}(\rho) &= \int dz dz' \phi_0(z)^2 V_d(\rho, z - z') \phi_0(z')^2 \\ &= -\frac{d^2}{\sqrt{2} l_z \rho^2} \{ 2P_2(\cos \theta) \Psi(1/2, 0; \rho^2/2l_z^2) \\ &\quad - 3 \left[P_2(\cos \theta) - \frac{1}{2} \sin^2 \theta \cos 2\varphi_r \right] \\ &\quad \times \Psi(1/2, -1; \rho^2/2l_z^2) \} \end{aligned} \quad (49)$$

where $\Psi(a, b; z)$ is the confluent hypergeometric function and θ is the angle between the direction of the dipoles (in the (x, z) -plane) and the motion in the (x, y) -plane, has the following Fourier transform

$$\begin{aligned} V_d^{2D}(\mathbf{p}) &= -\sqrt{2} \pi \frac{d^2}{l_z} w(p l_z / \hbar \sqrt{2}) \\ &\quad \times [2P_2(\cos \theta) - \sin^2 \theta \cos 2\varphi_p] \end{aligned} \quad (50)$$

where $w(x) = x \exp(x^2) \operatorname{erfc}(x)$, with $\operatorname{erfc}(x)$ being the error function and φ_p the angle between \mathbf{p} and the x -axis. For $p \sim p_F \ll l_z$, one has

$$V_d^{2D}(\mathbf{p}) \approx -\pi \frac{d^2}{\hbar} p [2P_2(\cos \theta) - \sin^2 \theta \cos 2\varphi_p] \quad (51)$$

which is linear in p . (Strictly speaking, expression 51 contains also a constant which depends on the regularization of the Fourier integral at the origin. This constant corresponds to a short-range interparticle interaction and, hence, has no physical effect in a single component Fermi gas because all its contributions should vanish upon proper antisymmetrization. We therefore set this constant to zero.) Within the Hartree–Fock approximation, one then obtains (assuming $a_d k_F \ll 1$)

$$p_F(\mathbf{n}) = \hbar k_F \left[1 + \frac{8}{15\pi} a_d k_F \sin^2 \theta \cos 2\varphi_p \right]$$

for the position $\mathbf{p} = n p_F(\mathbf{n})$ of the Fermi surface, where now $\mathbf{n} = (\cos \phi_n, \sin \phi_n)$ is the unit vector of direction in the (x, y) -plane, and

$$\frac{m}{m_{2DL}^*(\mathbf{n})} = 1 + \frac{4a_d k_F}{3\pi} \left[P_2(\cos \theta) - \frac{7}{10} \sin^2 \theta \cos 2\varphi_p \right]$$

$$\frac{m}{m_{2DT}^*(\mathbf{n})} = \frac{16}{15\pi} a_d k_F \sin^2 \theta \cos 2\varphi_p$$

for the longitudinal (along \mathbf{n}) and transverse (perpendicular to \mathbf{n}) components of the effective mass, respectively.⁹⁵ Note that for $\theta = 0$ (dipoles are perpendicular to the plane and, therefore, the system has rotational symmetry around the z -axis) the deformation of the Fermi surface disappears and $\mathbf{v}_F = \mathbf{p}_F/m^*$ with $m^*/m \approx 1 - 4a_d k_F/3\pi$.

4.2.2. Collective Modes (Landau Zero Sound).

Collective modes in a dipolar gas can be studied on the basis of the kinetic equation, eq 45. For small deviation of the quasiparticle distribution from equilibrium of the form

$$\delta n(\mathbf{r}, \mathbf{p}, t) \approx \kappa(\mathbf{p}) \exp[i(\mathbf{k}\mathbf{r} - \omega t)] \ll n_{\text{eq}}(\mathbf{p})$$

the kinetic equation reduces to the following equation on the unknown function $\kappa(\mathbf{p})$

$$\begin{aligned} [\omega - \mathbf{k}\nabla_{\mathbf{p}}\varepsilon(\mathbf{p})]\kappa(\mathbf{p}) \\ = \mathbf{k}\nabla_{\mathbf{p}}\varepsilon(\mathbf{p}) \frac{\partial n_{\text{eq}}(\mathbf{p})}{\partial \varepsilon(\mathbf{p})} \int \frac{d\mathbf{p}'}{(2\pi\hbar)^D} f(\mathbf{k}, \mathbf{p}, \mathbf{p}') \kappa(\mathbf{p}') \end{aligned} \quad (52)$$

where $\nabla_{\mathbf{p}} = \partial/\partial\mathbf{p}$ and the wave vector k is assumed to be much smaller than $k_F = p_F/\hbar$, $k \ll k_F$. In the Hartree–Fock approximation, the f -function is $f(\mathbf{k}, \mathbf{p}, \mathbf{p}') = V_d(\mathbf{k}) - V_d(\mathbf{p} - \mathbf{p}')$; see the comments below eq 48 and refs 94 and 95. Equation 52 was analyzed numerically for a 3D gas in refs 94 and 95 and in 2D gas in refs 95 and 97. (Note that in a 2D gas (monolayer) the first term in the f -function can be omitted

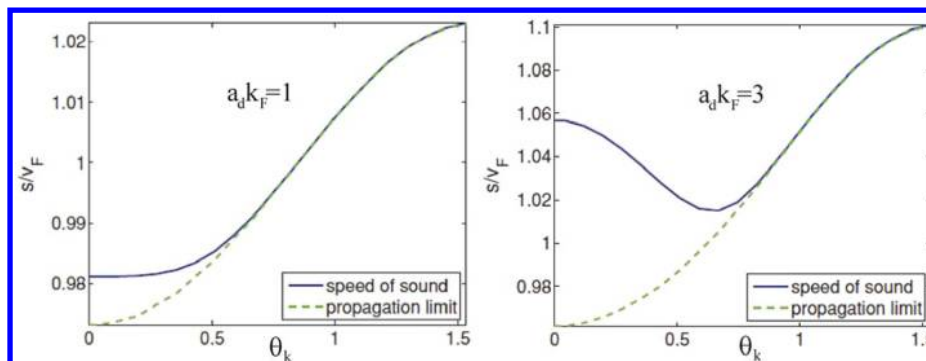


Figure 8. Speed of sound (solid curve) in a 3D dipolar Fermi gas as a function of the angle of propagation θ_k relative to the direction of polarization, for dipolar interaction strengths $a_d k_F = 1$ (left panel) and $a_d k_F = 3$ (right panel). The speed is measured in units of v_F . The dashed curve represents a lower bound on the speed of any undamped mode. (Taken from ref 94. Copyright 2010 American Physical Society.)

following the arguments from the end of the previous section.) The results for the sound velocity in a 3D gas together with the propagation limit due to the particle–hole continuum are shown in Figure 8 as a function of the propagation angle (the angle between \mathbf{k} and the z -axis). They show that the collective mode can propagate only in the certain cone of directions around the direction of dipoles polarization. This is counterintuitive to some extent because this is the direction in which two dipoles attract each other; on the other hand, in the perpendicular direction, in which dipoles repel each other and, hence, one would expect the existence of the collective mode, no zero sound is possible. This can be understood by noting that the zero-sound propagation is dominated by the exchange contribution, not a direct one, and therefore, the intuition based on the direct interaction does not work; see ref 94 for more discussions of this issue. The sound velocity depends strongly on both the propagation direction θ_k and interactions strength $a_d k_F$: It increases monotonically with θ_k for $a_d k_F \lesssim 1$ and becomes nonmonotonic in θ_k for $a_d k_F > 1$; see Figure 8.

In a dipolar monolayer (quasi-2D gas), the situation is even more intriguing because the existence of zero-sound and the value of the sound velocity strongly depend on the propagation direction (ϕ_k is the angle between \mathbf{k} and the x -axis), on the tilting angle θ , and on the strength of the interaction. In this case, there are no collective modes if the tilting angle is smaller than some critical value that depends on the interaction strength; see Figure 9.

This is again counterintuitive because the direct interaction for small tilting angles is purely repulsive (dipoles are almost perpendicular to the motion plane), and one would expect stable collective zero-sound modes. However, similar to the 3D case, the f -function contains only an exchange contribution, and this explains such peculiar behavior of collective modes. (The collective modes without an exchange contribution were considered in ref 96.) Note also that with increasing the tilting angles from the critical one, the direction in plane, in which one has propagating zero-sound, changes from those around the projection \mathbf{d}_{\parallel} of the dipole moment \mathbf{d} on the plane to those around the direction perpendicular to \mathbf{d}_{\parallel} (when the polarization of dipoles approaches the plain); see Figure 10.

Note, however, that the above results for collective modes were obtained with the f -function in the lowest-order Hartree–Fock approximation, $f(\mathbf{k}, \mathbf{p}, \mathbf{p}') = V_d(\mathbf{k}) - V_d(\mathbf{p} - \mathbf{p}')$. Taking higher order terms into account can change the situation: As was shown in ref 98 for the case of a 2D dipolar Fermi gas polarized perpendicular to the motion plane, $\theta = 0$, the

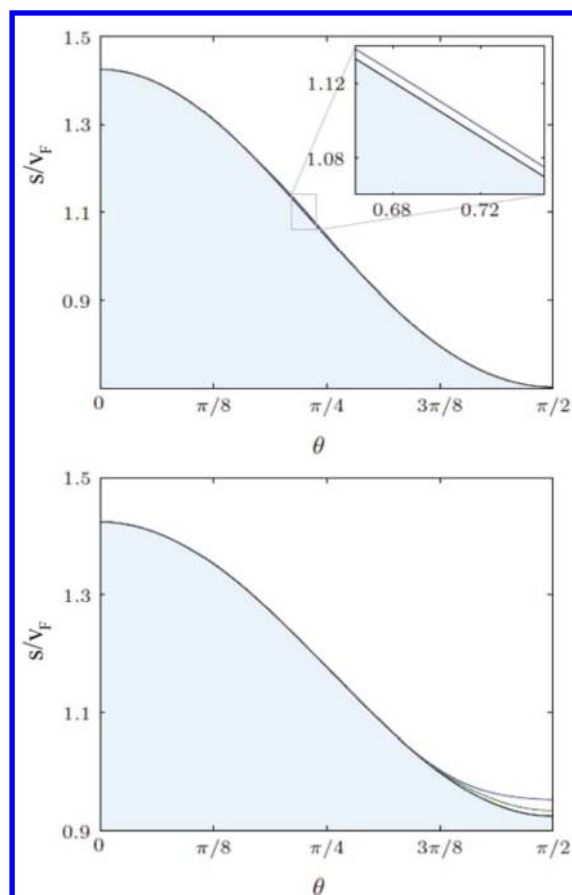


Figure 9. Speed of zero sound in a 2D dipolar Fermi gas as a function of the tilting angle θ for $a_d k_F = 1$ and the propagation angles $\phi_k = 0$ (upper panel) and $\phi_k = \pi/2$ (lower panel). The shaded region corresponds to strong damping. (Taken from ref 97.)

inclusion of second order contributions to the f -function results in the appearance of a stable zero-sound mode with the velocity $s = v_F[1 + 2(a_d k_F)^4]$.

4.3. BCS Pairing in a Homogeneous Single-Component Dipolar Fermi Gas

The partial attractiveness of the dipole–dipole interaction opens the possibility for BCS pairing in a fermionic many-body dipolar system at sufficiently low temperatures. As we will see in this section, the pairing in dipolar systems has generically an unconventional character (different from a singlet isotropic s -

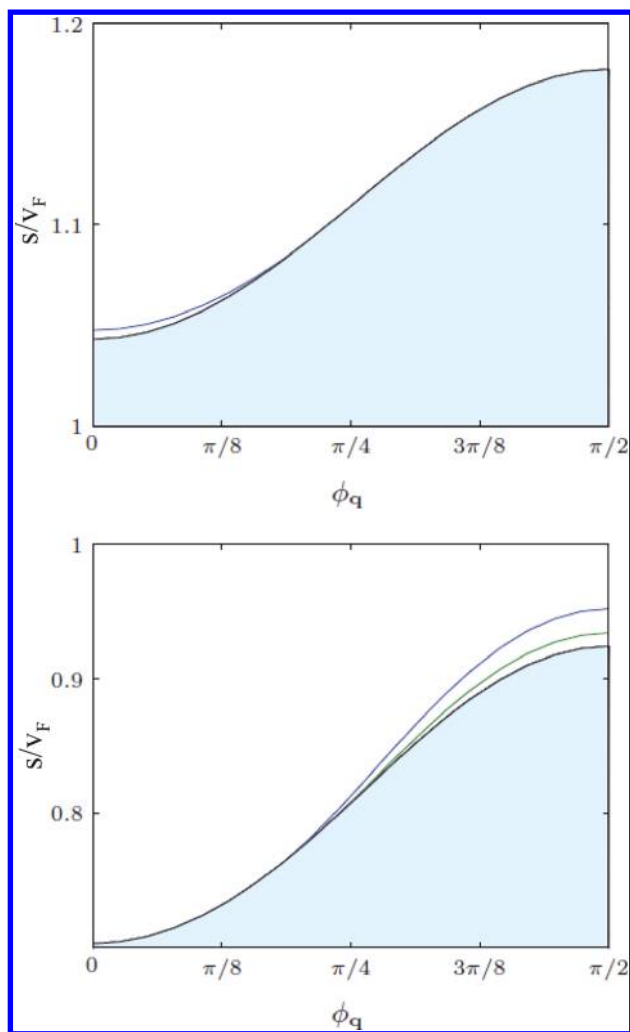


Figure 10. Speed of zero sound in a 2D dipolar Fermi gas as a function of the propagation angle ϕ_q for $a_d k_F = 1$ and $\theta = \pi/4$ (upper panel) and $\theta = \pi/2$ (lower panel). The shaded regions correspond to strong damping. (Taken from ref 97.)

wave pairing as in a two-component fermionic system with an isotropic attractive interaction), and a superfluid state has many peculiar properties that are different from those of conventional superconductors. Indeed, the s -wave (together with other even angular momenta) two-particle interaction channel is forbidden in a single-component Fermi gas by the Pauli principle. On the other hand, the angular part of the matrix element for the dipole–dipole interaction between the states with the angular momentum $L = 1$ (p -wave channel) and its projection on the z -axis $M = 0$ is negative (i.e., corresponding to an attractive interaction):

$$\langle L = 1, M = 0 | -3 \cos^2 \theta | L = 1, M = 0 \rangle = -\frac{4\pi}{5} < 0 \quad (53)$$

and, therefore, can lead to BCS pairing. (The matrix elements between the states with $M = \pm 1$ are positive.) It is easy to see that this pairing should be anisotropic, reaching its maximum amplitude in the direction of dipolar polarization when two dipoles attract each other, and being zero in the perpendicular directions corresponding to repulsive dipole–dipole interaction. As we will see, the dominant contribution has p -wave symmetry.

The Cooper pairing in a polarized single-component dipolar Fermi gas has been discussed in refs 99 and 100 within the BCS approach with the restriction to purely p -wave pairing. An exact value of the critical temperature and the angular dependence of the order parameter for a dilute gas were found in ref 101.

After omitting the contribution of the short-range part of the interparticle interaction, as discussed above, the Hamiltonian of a homogeneous single-component polarized dipolar Fermi gas reads

$$H = \int d\mathbf{r} \hat{\psi}^\dagger(\mathbf{r}) \left[-\frac{\hbar^2}{2m} \nabla^2 - \mu \right] \hat{\psi}(\mathbf{r}) + \frac{1}{2} \int d\mathbf{r} d\mathbf{r}' \hat{\psi}^\dagger(\mathbf{r}) \hat{\psi}^\dagger(\mathbf{r}') V_d(\mathbf{r} - \mathbf{r}') \hat{\psi}(\mathbf{r}') \hat{\psi}(\mathbf{r}) \quad (54)$$

We considered the property of the system with this Hamiltonian in the dilute limit $na_d^3 \ll 1$ and at temperatures T much smaller than the chemical potential μ (or the Fermi energy ε_F), $T \ll \mu = \varepsilon_F \approx (\hbar^2/2m)(6\pi^3n)^{2/3}$, relevant for Cooper pairing. In this case one can neglect the corrections $\delta\mu$ to the chemical potential due to the dipole–dipole interaction because $\delta\mu \sim d^2n \sim \varepsilon_F(na_d^3)^{1/3} \ll \varepsilon_F$.

The BCS pairing corresponds to a nonzero value of the order parameter

$$\Delta(\mathbf{r}_1 - \mathbf{r}_2) = V_d(\mathbf{r}_1 - \mathbf{r}_2) \langle \hat{\psi}(\mathbf{r}_1) \hat{\psi}(\mathbf{r}_2) \rangle$$

which can be viewed as a wave function of Cooper pairs. Because of anticommutativity of the fermionic field operators, $\Delta(\mathbf{r}_1 - \mathbf{r}_2)$ changes sign under the exchange of particles $\mathbf{r}_1 \leftrightarrow \mathbf{r}_2$ forming a pair. As a consequence, the order parameter in momentum space

$$\Delta(\mathbf{p}) = \int d\mathbf{r} \exp(-i\mathbf{p}\mathbf{r}/\hbar) \Delta(\mathbf{r})$$

is also antisymmetric, $\Delta(-\mathbf{p}) = -\Delta(\mathbf{p})$. Because of the anisotropy of the dipole–dipole interaction, the angular momentum L of the relative motion of two particles is not a conserved quantum number, but its projection on the z -axis (in the considered geometry) is. We can therefore write $\Delta(\mathbf{p})$ in the form

$$\Delta(\mathbf{p}) = \sum_{\text{odd } L} \Delta_L(\mathbf{p}) Y_{L0}(\hat{\mathbf{p}}) \quad (55)$$

where $Y_{LM}(\hat{\mathbf{p}})$ are the spherical harmonics and $\hat{\mathbf{p}}$ is the unit vector in the direction of the momentum \mathbf{p} . We keep in the sum only odd angular momentum L following the discussion above and set $M = 0$ in every term. This is because M is conserved and, following eq 53, only for $M = 0$ does one have an attractive interaction.

A nonzero order parameter and, therefore, the superfluid properties in the system appear for temperatures below some temperature T_c , which is the critical temperature of the superfluid transition. This critical temperature and the order parameter Δ for temperatures below T_c can be found from the gap equation^{102,103} (we use the momentum representation and assume the order parameter to be a real function of momentum \mathbf{p})

$$\Delta(\mathbf{p}) = - \int \frac{d\mathbf{p}'}{(2\pi\hbar)^3} V(\mathbf{p}, \mathbf{p}') \frac{\tanh(E(\mathbf{p}')/2T)}{2E(\mathbf{p}')} \Delta(\mathbf{p}') \quad (56)$$

where $E(\mathbf{p}) = [\Delta^2(\mathbf{p}) + (p^2/2m - \mu)^2]^{1/2}$ is the energy of single-particle excitations in the superfluid gas. The effective interparticle interaction is described by the function $V(\mathbf{p}, \mathbf{p}') = V_d(\mathbf{p} - \mathbf{p}') + \delta V(\mathbf{p}, \mathbf{p}')$. Here $V_d(\mathbf{q})$ is the Fourier transform of the bare dipole–dipole interaction potential $V_d(\mathbf{r})$:

$$V_d(\mathbf{q}) = \frac{4\pi}{3} d^2 (3 \cos^2(\theta_q) - 1) \quad (57)$$

with θ_q being the angle between the momentum \mathbf{q} and the z -axis, and $\delta V(\mathbf{p}, \mathbf{p}')$ corresponds to corrections to the bare interparticle interaction V_d resulting from many-body effects. The effective interaction $V(\mathbf{p}, \mathbf{p}')$ describes all scattering processes in the system which transform a pair of particles with momenta \mathbf{p}' and $-\mathbf{p}'$ into a pair with momenta \mathbf{p} and $-\mathbf{p}$. The leading process here is the direct scattering of the two particles on each other [the term $V_d(\mathbf{p} - \mathbf{p}')$], while the many-body corrections $\delta V(\mathbf{p}, \mathbf{p}')$ describe processes of higher order in V_d . The leading terms in δV are second order in V_d (see ref 104) and correspond to scattering processes in which the two colliding particles interact with each other indirectly with an involvement of particle–hole excitations which they create in the system (see more details in ref 101). These processes are important even in the weakly interacting case (although they are of second order in the small parameter) because they result in the pre-exponential factor in the expression for the critical temperature; see eq 59.

The gap equation (eq 56) can be simplified for temperatures just below T_c because for such temperatures the order parameter $\Delta(\mathbf{p})$ is small and, hence, the right-hand-sides of eq 56 can be expanded in powers of $\Delta(\mathbf{p})$. The resulting equation

$$\Delta(\mathbf{p}) = - \int \frac{d\mathbf{p}'}{(2\pi\hbar)^3} V(\mathbf{p}, \mathbf{p}') \times \left[K(p') \Delta(\mathbf{p}') + \frac{\partial K(p')}{\partial \xi'} \frac{\Delta^3(\mathbf{p}')}{2\xi'} \right] \quad (58)$$

where $K(p) = \tanh(\xi/2T)/2\xi$ and $\xi = p^2/2m - \mu$, is equivalent to the Ginzburg–Landau equation for a spatially homogeneous order parameter.

Note that eq 58 always has the trivial solution $\Delta = 0$, which corresponds to a normal phase of the Fermi gas. The Cooper pairing is associated with a nontrivial solution of the gap eq 58 which exists for temperatures $T \leq T_c$. To find the critical temperature T_c it is sufficient to keep only the linear term in the square brackets on the right-hand-side of eq 58 because $\Delta \rightarrow 0$ for $T \rightarrow T_c$. The corresponding linearized gap equation allows also finding the momentum dependence of the order parameter. The absolute temperature dependent value of Δ is determined by the nonlinear term on the right-hand-side of eq 58.

The result for the critical temperature reads (see ref 101 for details)

$$T_c = 1.44 \varepsilon_F \exp\left(-\frac{\pi \varepsilon_F}{12nd^2}\right) \quad (59)$$

For temperatures T close to T_c , the anisotropic order parameter $\Delta(\mathbf{p})$ on the Fermi surface, $p = p_F$, has the form

$$\Delta(p_F \hat{\mathbf{p}}) \approx 2.5 T_c \sqrt{1 - \frac{T}{T_c}} \phi_0(\hat{\mathbf{p}}) \quad (60)$$

where

$$\phi_0(\hat{\mathbf{p}}) = \sqrt{2} \sin\left(\frac{\pi}{2} \cos \theta_p\right) \quad (61)$$

with θ_p being the angle between the vector \mathbf{p} and the z -axis.

For momenta away from the Fermi surface, the order parameter is

$$\Delta(\mathbf{p}) \approx - \frac{\pi}{8d^2} \int \frac{d\mathbf{p}'}{4\pi} V_d(\mathbf{p} - p_F \hat{\mathbf{p}}') \Delta(p_F \hat{\mathbf{p}}')$$

The dependence of the order parameter $\Delta(\mathbf{p})$ on the modulus p of the momentum \mathbf{p} for several values of the angle θ_p is shown in Figure 11.

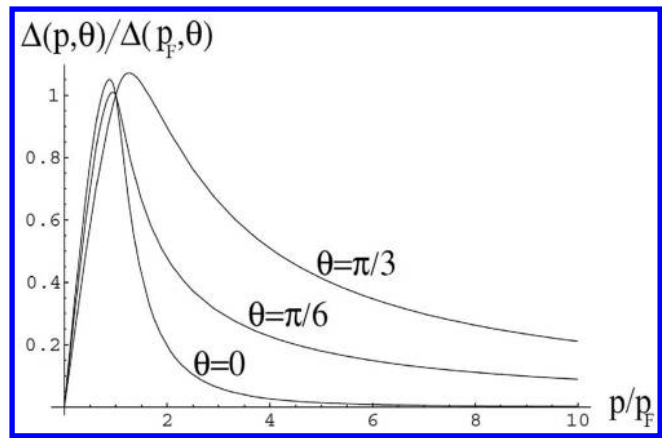


Figure 11. Order parameter $\Delta(p, \theta)$ [in units of $\Delta(p_F, \theta)$] as a function of the momentum p (in units of p_F) for various values of the polar angle θ . (Taken from ref 101.)

This momentum dependence of the order parameter in a dipolar Fermi gas is in contrast to that for pairing (both s - and p -wave) due to a short-range interparticle interaction, in which case the order parameter is a constant for momenta $p \lesssim \hbar/r_0$, where r_0 is the range of the interparticle interaction, and rapidly decays for $p > \hbar/r_0$.

The anisotropy of the order parameter in the momentum space described by the function $\phi_0(\mathbf{n}) = \sqrt{2} \sin[(\pi/2) \cos \theta]$ (see eq 60) provides another difference from the conventional s -wave pairing, say in a two-component Fermi gas with a short-range intercomponent attractive interaction. As a result of this anisotropy, the gap $|\Delta(p_F \hat{\mathbf{p}})|$ in the spectrum of single-particle excitations in a dipolar superfluid gas depends on the direction of momentum $\hat{\mathbf{p}}$: The gap reaches its maximum in the directions parallel to the direction of the dipoles ($\theta_p = 0, \pi$), while it vanishes in the direction perpendicular to the dipoles ($\theta_p = \pi/2$). Similar anisotropy is expected in the properties of collective excitations and, as a result, in the response of the dipolar superfluid dipolar Fermi gas.

The vanishing of the single-particle gap at $\theta_p = \pi/2$ (and arbitrary azimuthal angle ϕ , i.e. on the line on the Fermi surface $p = p_F$) results in the T^2 dependence of the specific heat of the gas at low temperatures $T \ll \Delta_0 \sim T_c$ (the contribution of collective excitations is proportional to T^3). Note that, for the conventional s -wave pairing, the low-temperature specific heat is determined by the contribution of collective modes ($\propto T^3$), while the contribution of single-particle excitations is exponentially suppressed.

The above-mentioned properties of a superfluid dipolar Fermi gas are similar to those of the polar phase of superfluid liquid ^3He . This phase, however, cannot be realized in

experiments because it has higher energy than the experimentally observed *A* and *B* phases (see, e.g., ref 105). Note that several heavy-fermion compounds in a superconducting state (for a review of superconducting phases of heavy-fermion compounds, see, e.g., refs 106, 107, and 108) also have lines of zeros of the order parameter on the Fermi surface and, as a consequence, a T^2 -dependence of the low-temperature specific heat (see, e.g., ref 109).

4.4. BCS Pairing in a Trapped Single-Component Dipolar Fermi Gas

Similar to the bosonic case, the trap geometry strongly influences the BCS pairing in a polarized dipolar Fermi gas as a result of the dipole–dipole interaction. It is natural to expect that cigar-shaped traps are more favorable for pairing than pancake-shaped ones because the dipole–dipole interaction is on average attractive in the former case and repulsive in the latter one. As a result, the critical temperatures in cigar-shaped traps should be higher. This question was addressed in refs 86 and 110.

In a trapped gas, the BCS order parameter

$$\Delta(\mathbf{r}_1, \mathbf{r}_2) = V_d(\mathbf{r}_1 - \mathbf{r}_2) \langle \hat{\psi}(\mathbf{r}_1) \hat{\psi}(\mathbf{r}_2) \rangle \quad (62)$$

depends on both coordinates \mathbf{r}_1 and \mathbf{r}_2 and not only on their difference $\mathbf{r}_1 - \mathbf{r}_2$ as in the spatially homogeneous case, because the translational symmetry is broken by the trapping potential. To find the critical temperature T_{ctrapp} in the trap, it is sufficient to consider the linearized gap equation:

$$\Delta(\mathbf{r}_1, \mathbf{r}_2) = -V_d(\mathbf{r}_1 - \mathbf{r}_2) \int d\mathbf{r}_3 d\mathbf{r}_4 K(\mathbf{r}_1, \mathbf{r}_2; \mathbf{r}_3, \mathbf{r}_4) \Delta(\mathbf{r}_3, \mathbf{r}_4) \quad (63)$$

with the kernel

$$K(\mathbf{r}_1, \mathbf{r}_2; \mathbf{r}_3, \mathbf{r}_4) = \sum_{\nu_1, \nu_2} \frac{\tanh(\xi_{\nu_1}/2T) + \tanh(\xi_{\nu_2}/2T)}{\xi_{\nu_1} + \xi_{\nu_2}} \times \phi_{\nu_1}(\mathbf{r}_1) \phi_{\nu_2}(\mathbf{r}_2) \phi_{\nu_1}^*(\mathbf{r}_3) \phi_{\nu_2}^*(\mathbf{r}_4)$$

where $\xi_\nu = \varepsilon_\nu - \mu$ and $\phi_\nu(\mathbf{r})$ are the eigenenergies (shifted by the chemical potential μ) and the eigenfunctions of the single-particle Schrödinger equation in the trap

$$\left\{ -\frac{\hbar^2}{2m} \Delta + U_{\text{tr}}(\mathbf{r}) \right\} \phi_\nu(\mathbf{r}) = \varepsilon_\nu \phi_\nu(\mathbf{r})$$

where $U_{\text{tr}}(\mathbf{r})$ is given by eq 13. Note that the gap equation (eq 63) does not contain the mean-field Hartree–Fock corrections. They lead to an unimportant change of parameters of the Hamiltonian (eq 54) and, therefore, are not relevant for pairing. The many-body contributions δV to the effective interparticle interaction which are also absent in eq 63 (compare with eq 56) will be taken into account later.

The results of the analysis of eq 63 in ref 110 are the following. When $\omega_\rho \approx \omega_z \ll T_c$ (shallow nearly spherical trap), where T_c is the critical temperature of the BCS transition in a spatially homogeneous gas with the density n equal to the central density n_0 in the trap, it is convenient to perform the Fourier transformation with respect to the relative coordinate $\mathbf{r} = \mathbf{r}_1 - \mathbf{r}_2$,

$$\tilde{\Delta}(\mathbf{R}, \mathbf{p}) = \int d\mathbf{r} \exp(-i\mathbf{p}\mathbf{r}/\hbar) \Delta(\mathbf{R} + \mathbf{r}/2, \mathbf{R} - \mathbf{r}/2)$$

where $\mathbf{r} = (\mathbf{r}_1 + \mathbf{r}_2)/2$ is the coordinate of the center of mass. The characteristic scale of the p -dependence of $\tilde{\Delta}(\mathbf{R}, \mathbf{p})$ is of the order of the Fermi momentum p_F , while for the R -dependence it is of the order of the size of the cloud R_{TF} , which is much larger than the typical size $\xi_0 = p_F/mT_c$ of pairing correlations (coherence length), $R_{TF} \gg \xi_0$. We therefore can write the order parameter on the local Fermi surface as $\tilde{\Delta}[\mathbf{R}, \mathbf{p} = \mathbf{n}p_F(\mathbf{R})] = \tilde{\Delta}(\mathbf{R}) \varphi_0(\mathbf{n})$, where the function $\tilde{\Delta}(\mathbf{R})$ obeys the equation (see ref 110 for details)

$$\left\{ -\frac{7\zeta(3)}{48\pi^2} \left(\frac{p_F}{mT_c} \right)^2 \sum_{\alpha=x,y,z} f_\alpha \nabla_{R_\alpha}^2 + \frac{U_{\text{trap}}(\mathbf{R})}{\mu} \left(1 + \frac{\pi\varepsilon_F}{24nd^2} \right) \right\} \times \tilde{\Delta}(\mathbf{R}) = \ln \frac{T_c}{T_{\text{ctrapp}}} \tilde{\Delta}(\mathbf{R}) \quad (64)$$

with $f_x = f_y = 1 - 3/\pi^2$, $f_z = 1 + 6/\pi^2$. The solution of this equation, which is formally equivalent to the Schrödinger equation for a three-dimensional anisotropic harmonic oscillator, for the lowest eigenvalue gives the following expression

$$\frac{T_c - T_{\text{ctrapp}}}{T_c} \approx \ln \frac{T_c}{T_{\text{ctrapp}}} = \sqrt{\frac{7\zeta(3)}{48\pi^2} \left(1 + \frac{\pi\varepsilon_F}{24nd^2} \right)} \times \left[2 \frac{\omega_\rho}{T_c} \sqrt{1 - \frac{3}{\pi^2}} + \frac{\omega_z}{T_c} \sqrt{1 + \frac{6}{\pi^2}} \right] \quad (65)$$

for the change of the critical temperature due to the presence of the trapping potential. According to this expression, the critical temperature in the trap is always smaller than that in the homogeneous gas. In the considered case, we have $\omega_\alpha/T_c \ll 1$ but $\pi\varepsilon_F/24nd^2 > 1$ (weakly interacting gas). Taking into account that $7\zeta(3)/(48\pi^2) \approx 0.018$, we see that the difference between T_{ctrapp} and T_c is small if $\pi\varepsilon_F/24nd^2$ is not very large.

The order parameter just below T_c is given by the corresponding eigenfunction and has the Gaussian form

$$\tilde{\Delta}(\mathbf{R}) \propto \exp\left(-\sum_{\alpha=x,y,z} R_\alpha^2/2l_{\Delta\alpha}^2\right)$$

where

$$l_{\Delta\alpha} = \frac{p_F}{m\omega_\alpha} \sqrt{\frac{\omega_\alpha}{T_c} \left[\frac{7\zeta(3)f_\alpha}{48\pi^2} \left(1 + \frac{\pi\varepsilon_F}{24nd^2} \right) \right]^{-1/4}}$$

is the characteristic size in the α -th direction. If again the quantity $\pi\varepsilon_F/24nd^2$ is not very large, we have $l_{\Delta\alpha} \ll R_{TF}^{(\alpha)}$, where $R_{TF}^{(\alpha)} = p_F/m\omega_\alpha$ is the Thomas–Fermi radius of the trapped gas cloud in the α -th direction. This means that the pairing takes place only in the central part of the gas.

For a large number of particles, the gas is in the Thomas–Fermi regime (eq 43), and we have the following relation

$$N = \mu(n_0)^3 / 6\omega_z \omega_\rho^2$$

between the total number of particles N in the gas and the density n_0 in the center, where $\mu(n_0) = (6\pi^2 \hbar^3 n_0)^{2/3} / 2m$ is the chemical potential. For a fixed N and n_0 , this gives

$$\frac{T_{\text{trap}} - T_c}{T_c} = -\frac{\bar{\omega}}{T_c} \sqrt{\left(1 + \frac{\pi \varepsilon_F}{24nd^2}\right)} F(l) \quad (66)$$

where $\bar{\omega} = (\omega_z \omega_\rho)^{1/3}$ and $l = (\omega_\rho / \omega_z)^{1/2}$ is the trap aspect ratio. The function $F(l) = [7\zeta(3)/48\pi^2]^{1/2} [2(1 - 3/\pi^2)^{1/2} l^{2/3} + (1 + 6/\pi^2)^{1/2} l^{-4/3}]$ is shown in Figure 12. The minimum of $F(l)$

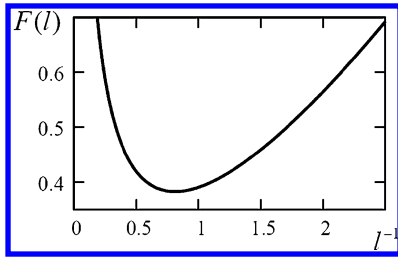


Figure 12. Function F versus the inverse trap aspect ratio l . (Taken from ref 110.)

provides the optimal trap aspect ratio $l^* = 1.23$ (cigar shaped trap, as expected) for the highest critical temperature in the trapped gas with the fixed total number of particles N and the density in the center n_0 (the critical temperature T_c of the homogeneous gas as a function of n_0 is given by eq 59). The optimal value is a result of the competition between the anisotropic dipole–dipole interparticle interaction and the finite-size effects: The former favors larger l (cigar shaped traps) while the latter, due to the zero boundary condition on the order parameter, acts on pairing, destructively imposing an upper limit on l .

The numerical solution of the linearized gap (eq 63) for the case $\mu \gg \omega_z \omega_\rho \approx T_c$ shows the existence of a critical trap aspect ratio l_c for a given interaction strength $\Gamma = 36n(0)d^2/\pi\mu$ and a number of particles N . This critical aspect ratio corresponds to zero critical temperature, $T_{\text{trap}} = 0$, such that no pairing is possible in traps with $l < l_c$. Alternatively, for fixed values of the trap aspect ratio l and the number of particles N , BCS pairing takes place if the interaction parameter Γ is large enough, $\Gamma > \Gamma_c$. The existence of the critical values l_c and Γ_c can be understood as follows: Due to the fact that the order parameter changes sign when the direction of the z -axis is reversed, single-particle states involved in forming the order parameter should have different (by an odd integer) quantum numbers n_z . As a result, these states have different energies (the minimum difference is ω_z) and can be paired only if the energy gain due to pairing (which is of the order of the critical temperature T_c) exceeds this difference. In the limiting case of an infinite pancake trap with the confinement only in the z -direction, this results in the appearance of a critical trap frequency $\omega_{zc} = 1.8T_c^{86}$ with no pairing possible in traps with $\omega_z > \omega_{zc}$.

The dependence of the critical interaction strength Γ_c on the trap aspect ratio l for different N is shown in Figure 13. As expected, the critical interaction strength Γ_c decreases with increasing l . On the other hand, with increasing number of particles N , the interaction parameter becomes larger, $\Gamma \sim N^{1/6}$, and the critical aspect ratio l_c decreases.

The order parameter $\Delta_0(\mathbf{r})$ for a cigar shaped trap with $l = 2.2$ (see Figure 14) exhibits a nonmonotonic behavior with the distance from the trap center. This is to be compared with the monotonic behavior of the BCS order parameter in a two component Fermi gas with a short-range attractive interaction^{111,112} under similar conditions. (It should be noted,

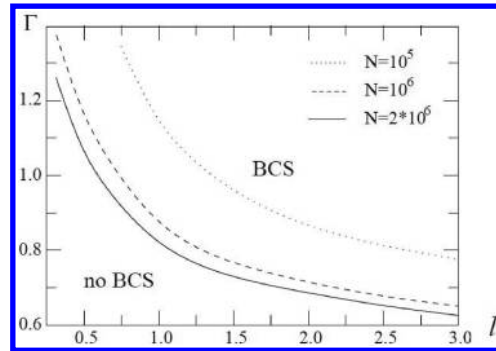


Figure 13. Critical lines Γ_c versus the aspect ratio l for different numbers of particles N . The BCS pairing takes place above the depicted curves. (Taken from ref 110.)

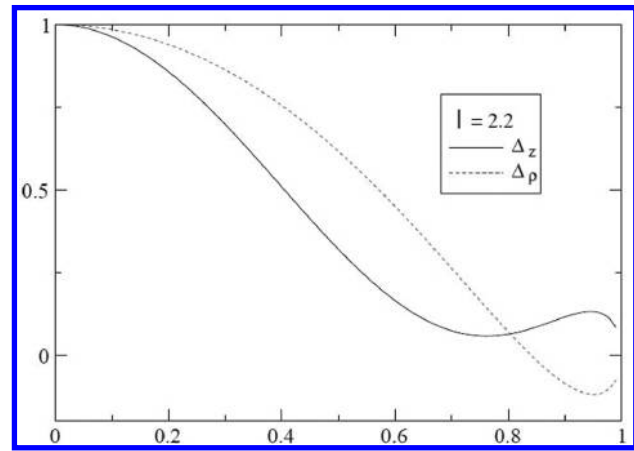


Figure 14. Order parameter for the aspect ratio $l = 2.2$ (cigar shaped trap). The solid line shows $\Delta(z, \rho=0)$, and the dotted line corresponds to $\Delta(z=0, \rho)$. (Taken from ref 110.)

however, that oscillating and highly nonmonotonic behaviors of the order parameter in a two component Fermi gas were obtained in ref 113 in the regime of an intershell pairing $T_c \ll \omega$.)

4.5. BCS Pairing in a Two Component Dipolar Fermi Gas

Adding the second component in a dipolar Fermi gas opens the possibility for a singlet interspecies pairing (equivalent to the s -wave pairing in a two component atomic Fermi gas), in addition to the triplet intraspecies pairing considered in section 4.3, and competition between them. Assuming chemical stability of a mixture of two species of polarized dipolar particles with equal masses, concentrations, and dipole moments (a mixture of fermionic polar molecules with two different hyperfine states, for example), this problem was considered in ref 114. The corresponding Hamiltonian reads

$$H = \sum_{\alpha} \int d\mathbf{r} \hat{\psi}_{\alpha}^{\dagger}(\mathbf{r}) \left[-\frac{\hbar^2}{2m} \nabla^2 - \mu \right] \hat{\psi}_{\alpha}(\mathbf{r}) + \frac{1}{2} \sum_{\alpha, \alpha'} \int d\mathbf{r} d\mathbf{r}' \hat{\psi}_{\alpha}^{\dagger}(\mathbf{r}) \hat{\psi}_{\alpha'}^{\dagger}(\mathbf{r}') V_{\alpha\alpha'}(\mathbf{r} - \mathbf{r}') \hat{\psi}_{\alpha'}(\mathbf{r}') \times \hat{\psi}_{\alpha}(\mathbf{r})$$

where $\alpha = \pm$ denotes two different species, the intraspecies interaction $V_{\alpha\alpha}(\mathbf{r})$ is the dipole–dipole one, $V_{\alpha\alpha}(\mathbf{r}) = V_d(\mathbf{r})$, while the interspecies interaction $V_{\alpha\alpha'}(\mathbf{r})$ for $\alpha' \neq \alpha$ contains a short-range part $V_s(\mathbf{r}) = (4\pi a_s/m)\delta(\mathbf{r})$ in addition to the

dipole–dipole interaction, $V_{\alpha\alpha'}(\mathbf{r}) = V_d(\mathbf{r}) + V_s(\mathbf{r})$, parametrized by the s -wave scattering amplitude a_s .

The order parameter of singlet interspecies pairing

$$\Delta_s(\mathbf{r}_1 - \mathbf{r}_2) = V_{-+}(\mathbf{r}_1 - \mathbf{r}_2) \langle \hat{\psi}_-(\mathbf{r}_1) \hat{\psi}_+(\mathbf{r}_2) \rangle$$

in momentum space is now a sum of all partial waves with even angular momentum L and zero azimuthal quantum number M ,

$$\Delta_s(\mathbf{p}) = \sum_{\text{even } L} \Delta_{sL}(p) Y_{L0}(\hat{\mathbf{p}}) \quad (67)$$

The corresponding gap equation is similar to eq 56 with $V(\mathbf{p}, \mathbf{p}') = V_d(\mathbf{p} - \mathbf{p}') + 4\pi a_s/m + \delta V(\mathbf{p}, \mathbf{p}')$.

In the BCS approach, when one neglects many-body contributions including the deformation of the Fermi-sphere in momentum space, the critical temperature of the singlet superfluid transition is (see ref 114)

$$T_c^{(s)} \approx \varepsilon_F \exp\left(-\frac{\varepsilon_F}{\pi n d^2 |\lambda_s|}\right) \quad (68)$$

and the corresponding order parameter on the Fermi surface reads [compare with eq 61]

$$\Delta_s(p_F \hat{\mathbf{p}}) \approx \cos[\cos \theta_p \sqrt{3/|\lambda_s|}] \quad (69)$$

where $|\lambda_s|$ is the largest positive root of the equation

$$t + \left(1 + \frac{2a_s k_F}{\pi} \frac{\varepsilon_F}{\pi n d^2}\right) \sqrt{\frac{t}{3}} \tan \sqrt{\frac{3}{t}} = 0$$

The order parameter (eq 69) is now a symmetric function under $\mathbf{p} \rightarrow -\mathbf{p}$, as it should be for a singlet pairing.

With the deformation of the Fermi surface taken into account, the problem was solved numerically (see ref 114 for details). It turns out that without contact interaction ($a_s = 0$) the critical temperature of the triplet intraspecies pairing is always higher and, therefore, the system undergoes the transition into the triplet intraspecies BCS state; see section 4.3. The ground state in this case is a mixture of two intraspecies triplet superfluids. However, switching on an attractive contact interaction ($a_s < 0$), one can increase the critical temperature of the singlet pairing and make it larger than that for the triplet one, such that the ground state corresponds to an interspecies singlet superfluid. The critical value of $a_s k_F$ as a function of $D = n d^2 / \varepsilon_F$ and the corresponding phase diagram are shown in Figure 15.

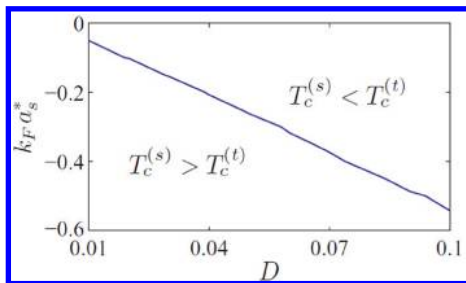


Figure 15. Dependence of the critical scattering length a_s^* on the strength of the dipole interaction $D = n d^2 / \varepsilon_F$, and the resulting superfluid phase diagram. (Taken from ref 114. Copyright 2010 American Physical Society.)

4.6. BCS Pairing in a Dipolar Monolayer

Let us now consider the possibility for superfluid pairing in a polarized dipolar monolayer—a polarized single-component dipolar gas confined to a (quasi)2D geometry by a harmonic trapping potential $V(z) = m\omega_z^2 z^2/2$, assuming $\hbar\omega_z \gg \varepsilon_F$, where $\varepsilon_F = p_F^2/2m$ is the Fermi energy of a Fermi gas with the 2D density $n_{2D} = p_F^2/4\pi\hbar^2$. An important parameter of the problem is the angle θ between the z -axis (normal to the 2D motion plane) and the direction of the dipole polarization; see Figure 16. The effective 2D interaction between dipoles is given by eqs

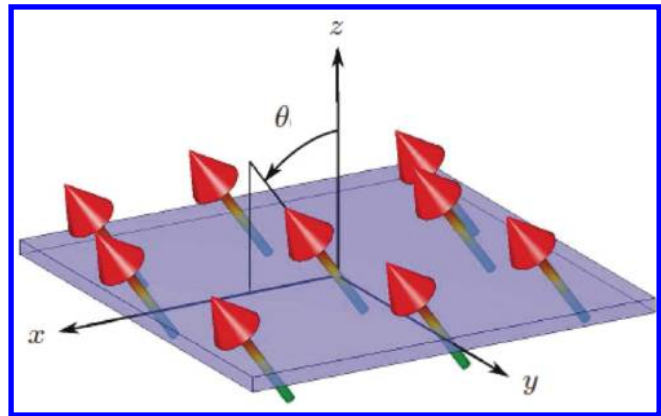


Figure 16. Fermionic monolayer: Fermionic dipoles are confined to the xy -plane. The dipoles are aligned in the xz -plane and form an angle θ with the z -axis.

49, 50, and 51. To see the possibility of BCS pairing, one has to look at the component in the p -wave channel. Straightforward but lengthy calculations¹¹⁵ show that it becomes negative when $\sin \theta > 2/3$, and, therefore, the system becomes unstable against BCS pairing. Note that the critical value $\theta_c = \arcsin 2/3 = 0.73$ (42°) is larger than the value $\arcsin 1/\sqrt{3} = 0.62$ (35°) of the angle θ , above which the dipole–dipole interaction has attractive directions in the (x, y) -plane.

Due to the anisotropy of the effective interaction (for $\theta > 0$), the azimuthal quantum number is no longer a conserving quantity and, therefore, the superfluid order parameter contains all odd harmonics in the azimuthal angle ϕ . In momentum space,

$$\Delta(\mathbf{k}) = \sum_{n=1}^{\infty} \Delta_n(k) \cos[(2n - 1)\phi_{\mathbf{k}}]$$

with the components $\Delta_n(k)$ coupled to each other through the gap equation. With only the $n = 1$ component taken into account, the problem was solved in ref 115, in which it was also found that the Fermi surface deformation due to anisotropy of the effective interaction does not play any significant role in the pairing problem and only slightly decreases the critical angle θ_c when the strength of the interaction increases. This result was confirmed by the analysis of ref 97, in which all components of $\Delta(\mathbf{k})$ were taken into account. It appears that the critical angle remains practically the same, and higher components of $\Delta(\mathbf{k})$ with $n > 1$ are visible only at angles very close to θ_c . For larger values of θ , one has $\Delta_{n>1}/\Delta_1 \lesssim 10^{-2}$ such that the pairing has indeed the p -wave character, $\Delta(\mathbf{k}) \approx \Delta_1(k) \cos \phi_{\mathbf{k}}$.

The critical temperature for the BCS pairing reads⁹⁷

$$T_c = \frac{2e^\gamma}{\pi} \varepsilon_F \exp \left[\frac{3\pi}{4k_F a_d} \frac{1}{(9/4)\sin^2 \theta - 1} \right] F_1(\theta) F_2(k_F l_z, \theta),$$

$$\theta > \theta_c = \arcsin 2/3 \quad (70)$$

where

$$F_1(\theta) = \frac{0.52 - 2.47 \sin^2 \theta + 2.83 \sin^4 \theta}{0.18 - 0.81 \sin^2 \theta + 0.91 \sin^4 \theta}$$

and

$$F_2(\eta, \theta) = \eta^{f(\theta)}, f(\theta) = \frac{0.25 - 1.13 \sin^2 \theta + 1.28 \sin^4 \theta}{0.18 - 0.81 \sin^2 \theta + 0.91 \sin^4 \theta}$$

The two functions $F_1(\theta)$ and $F_2(k_F l_z, \theta)$ in eq 70 describe deviations from the simplest BCS approach (with no account of the Fermi surface deformation): The exponent in eq 70 is simply the p -wave component of the effective dipole–dipole interaction on the undeformed Fermi surface. These deviations result from many-body corrections to the interparticle interaction and Fermi-liquid effects, as well as from the second order contribution to the two-body quasi-2D scattering amplitude. The latter includes virtual transitions to intermediate states which are not necessarily limited to the ground state of the transverse confinement. The virtual transitions to excited states of the transverse confinement, together with many-body contributions (those include corrections to the interparticle interaction, Fermi surface deformation, and Fermi-liquid effects—effective mass), contribute to the function $F_1(\theta)$. The virtual transitions to the states with ground state motion in the transverse confining potential contribute to both functions $F_1(\theta)$ and $F_2(k_F l_z, \theta)$ (see ref 97 for details). The latter transitions provide the second order Born term to the purely 2D scattering amplitude on the effective potential (eq 49), which has the so-called anomalous scattering contribution $\sim k^2$ in k (see more discussions below) due to long-range power decay of the potential. This anomalous contribution gives rise to the function $F_2(k_F l_z, \theta)$. Equation 70 predicts a rapid growth of T_c with increasing of the angle θ from the critical value $\theta_c = \arcsin 2/3$ to the values of the order of tens of nanokelvin for realistic experimental parameters; see Figure 17.

We obtain our results for the superfluid critical temperature using the mean-field approach. However, as it is well-known, this approach in two dimensions is only applicable at zero

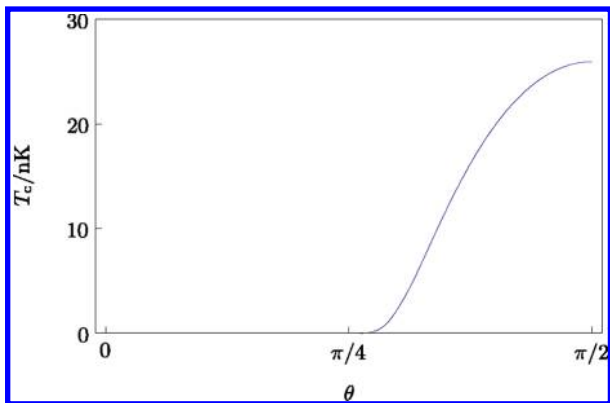


Figure 17. The critical temperature as a function of the tilting angle θ for $a_d k_F = 2.5$ and $k_F l \approx 0.2$. These values correspond to a gas of fermionic $^{15}\text{ND}_3$ molecules with the density $n_{2D} = 10^8 \text{ cm}^{-2}$ and $\omega_z = 2\pi \times 100 \text{ kHz}$. (Taken from ref 97.)

temperature, while at finite temperature the long-range order is destroyed by phase fluctuations and, therefore, the mean-field order parameter is zero. In this case, the transition into the superfluid phase follows the Berezinskii–Kosterlitz–Thouless (BKT) scenario,^{116,117} and ref 118. In the weak coupling limit, however, as it was pointed out by Miyake,¹¹⁹ the difference between the critical temperature calculated within the mean-field approach T_c and the critical temperature of the BKT transition T_{BKT} can be estimated as $T_c - T_{\text{BKT}} \sim T_c^2/\mu$ and, therefore, is small as compared to T_c . As a result, our mean-field calculations provide a reliable answer for the critical temperature in the considered weak coupling regime $a_d k_F < 1$.

Another interesting possibility to create a topologically nontrivial superfluid state in a monolayer was considered in refs 120 and 121, in which the authors consider a monolayer with fermionic dipoles oriented perpendicular to the plane ($\theta = 0$) and use the RF-dressing technique discussed in section 2.2.1 to create an effective (time-averaged) attractive potential $V_{\text{eff}}(\rho \rightarrow \infty) \approx -d_{\text{eff}}^2/\rho^3$. At short distances, the potential $V_{\text{eff}}(\rho)$ has a repulsive core that prevents low-energy particles from approaching each other and, therefore, suppresses inelastic collisions resulting in losses. The leading p -wave 2D scattering amplitude for identical fermions was found¹²¹ to be

$$f_1(k) = \int_0^\theta J_1(k\rho) V_{\text{eff}}(\rho) \psi_k^{(+)}(\rho) 2\pi\rho \, d\rho$$

$$\approx -\frac{8}{3} \frac{\hbar^2}{m} k r_* + \frac{\pi}{2} \frac{\hbar^2}{m} (k r_*)^2 \ln(C k r_*) \quad (71)$$

where $J_1(z)$ is the Bessel function, $\psi_k^{(+)}(\rho)$ is the radial wave function of the p -wave relative motion, the constant C is determined by the behavior of the potential at short distances, and the length scale $r_* = m d_{\text{eff}}^2/\hbar^2$ depends on the details of the RF-dressing (for BCS pairing, r_* has to be positive; for more details, see ref 121). The first term in eq 71 corresponds to the p -wave Born amplitude for the potential $V_{\text{eff}}(\rho) = -(\hbar/m)r_*\rho^{-3}$ while the second term contains both the anomalous scattering due to the dipole–dipole tail of the interparticle interaction and the short-range contribution.

For $k r_* \ll 1$, the first term in eq 71 is negative and, therefore, leads to a p -wave superfluid transition. The most stable low-temperature p -wave superfluid phase in 2D has $p_x + i p_y$ symmetry, $\Delta_{\mathbf{k}} = \Delta(k) \exp(i\varphi_{\mathbf{k}})$, because this is the only p -wave superfluid phase with a nonzero energy gap on the entire Fermi sphere. The numerical solution of the gap equation^{120,121} shows that $\Delta(k)$ rises linearly for $k \lesssim k_F$ and approaches a constant $\pi e^{-\gamma} T_c$ for $k \gtrsim k_F$. The critical temperature T_c reads

$$T_c = \varepsilon_F \frac{\kappa}{(k_F r_*)^{9\pi^2/64}} \exp \left[-\frac{3\pi}{4k_F r_*} \right]$$

where

$$\kappa \approx 0.16 \exp \left(-\frac{9\pi^2}{64} A \right)$$

with the numerical coefficient A determined by the short-distance behavior of the interparticle interaction. Note that the value of the critical temperature is very sensitive to the short-range part of the effective potential $V_{\text{eff}}(\rho)$ and, by modifying it, can be varied within a few orders of magnitude, reaching the values of the order of tens of nanokelvin for realistic experimental parameters that correspond to the lifetime of

the system of the order of seconds; see ref 121 for details and discussions.

The resulting $p_x + ip_y$ superfluid pairing spontaneously breaks time-reversal invariance (the degenerate time-reversal partner is the $p_x - ip_y$ state). This phase belongs to the class of the so-called topological superconductors and can exist in one of two topologically distinct phases, depending on the sign of the chemical potential μ .¹²² The phase with $\mu < 0$ is topologically trivial (may be continuously deformed to the vacuum state), while the phase with $\mu > 0$ is topologically nontrivial (cannot be continuously deformed to the vacuum) and has several very interesting properties. One of the most interesting of them is that the vortices in this superfluid carry localized zero-energy states, described by a Majorana fermion. These Majorana states obey non-Abelian exchange statistics^{123,124} and can possibly be used for topologically protected quantum information processing.¹²⁵ In the considered case of the superfluid state of dipoles in a monolayer, the chemical potential is positive, $\mu > 0$, and the resulting superfluid phase is topologically nontrivial.

4.7. BCS Pairing in a Bilayer Dipolar System

The single-component fermionic bilayer dipolar system (see Figure 18) provides an example of a relatively simple many-

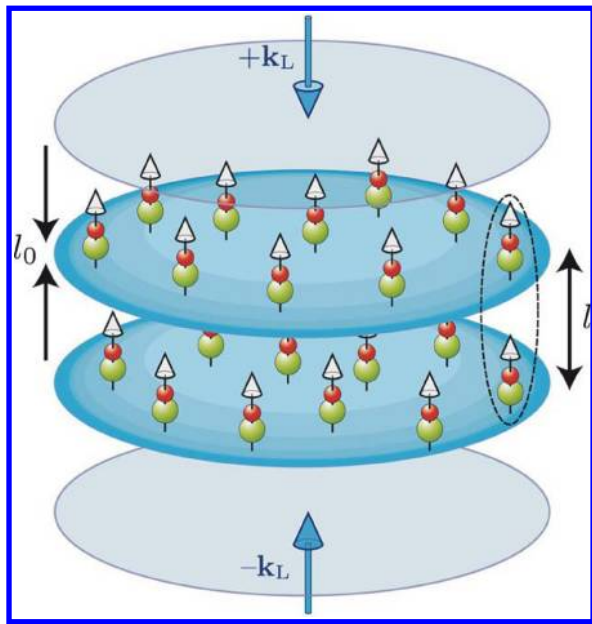


Figure 18. Setup of the dipolar bilayer system: Two layers with the thickness l_0 of a 1D optical lattice formed by two counterpropagating laser waves with wavevectors \mathbf{k}_L and $-\mathbf{k}_L$ are filled with dipoles oriented perpendicular to the layers. The interlayer distance l is π/k_L . An interlayer Cooper pair or molecule.

body system in which an entire range of nontrivial many-body phenomena are solely tied to the dipole–dipole interparticle interaction with its unique properties: long-range and anisotropy. The long-range character provides an interparticle interaction in single-component Fermi gases inside each layer that otherwise would remain essentially noninteracting. For the considered setup, this intralayer interaction is always repulsive and gives rise to the crystalline phase for a large density of particles (see section 2.2.3). More importantly, the long-range dipole–dipole interaction couples particles from different layers, allowing them to interact in the s -wave channel that is

dominant at low energies, allowing formation of bound states and BCS pairing.^{126,127} The Hamiltonian of the system reads

$$H = \sum_{\alpha=\pm} \int d\mathbf{r} \hat{\psi}_{\alpha}^{\dagger}(\mathbf{r}) \left\{ -\frac{\hbar^2}{2m} \Delta + \frac{1}{2} m \omega_z^2 z_{\pm}^2 - \mu' \right\} \hat{\psi}_{\alpha}(\mathbf{r}) + \frac{1}{2} \sum_{\alpha,\beta} \int d\mathbf{r} d\mathbf{r}' \hat{\psi}_{\alpha}^{\dagger}(\mathbf{r}) \hat{\psi}_{\beta}^{\dagger}(\mathbf{r}') V_d(\mathbf{r} - \mathbf{r}') \hat{\psi}_{\beta}(\mathbf{r}') \hat{\psi}_{\alpha}(\mathbf{r}) \quad (72)$$

where $\alpha = \pm$ is the layer index, $z_{\pm} \equiv z \pm l/2$, with l being the layer separation, $\hat{\psi}_{\alpha}(\mathbf{r})$ with $\mathbf{r} = (\rho, z)$ is the field operator for fermionic dipolar particles ($\rho = x\mathbf{e}_x + y\mathbf{e}_y$) on the corresponding layer α , $\Delta = \Delta_{\rho} + \partial^2/\partial z^2$ is the Laplace operator, ω_z is the confining frequency in each layer such that $l_z = (\hbar/m\omega_z)^{1/2}$, and μ' is the chemical potential. The last term describes the intra- ($\alpha = \beta$) and interlayer ($\alpha \neq \beta$) dipole–dipole interparticle interactions. Assuming a strong confinement, $\hbar\omega_z \gg \mu', T$, where T is the temperature, we can write $\hat{\psi}_{\alpha}(\mathbf{r}) = \hat{\psi}_{\alpha}(\rho) \phi_0(z_{\alpha})$ and, therefore, reduce the Hamiltonian (eq 72) to

$$H_{2D} = \sum_{\alpha=\pm} \int d\rho \hat{\psi}_{\alpha}^{\dagger}(\rho) \left\{ -\frac{\hbar^2}{2m} \Delta_{\rho} - \mu \right\} \hat{\psi}_{\alpha}(\rho) + \frac{1}{2} \sum_{\alpha,\beta} \int d\rho d\rho' \hat{\psi}_{\alpha}^{\dagger}(\rho) \hat{\psi}_{\beta}^{\dagger}(\rho') V_{\alpha\beta}(\rho - \rho') \hat{\psi}_{\beta}(\rho') \times \hat{\psi}_{\alpha}(\rho) \quad (73)$$

for a two-component fermionic field $\hat{\psi}_{\alpha}(\rho)$, $\alpha = \pm$, with shifted chemical potential $\mu = \mu' - \hbar\omega_z/2$. The intracomponent (intralayer) interaction $V_{\alpha\alpha}(\rho)$ coincides with $V_d^{2D}(\rho)$ in eq 49 for $\theta = 0$, and the intercomponent (interlayer) interaction is

$$V_{+-}(\rho) = V_{-+}(\rho) \equiv V_{2D}(\rho) \approx d^2 \frac{\rho^2 - 2l^2}{(\rho^2 + l^2)^{5/2}} \quad (74)$$

The considered system is characterized by three characteristic lengths: the dipolar length $a_d = md^2/\hbar^2$, the interlayer separation l , and the mean interparticle separation inside each layer $\sim k_F^{-1}$, with $k_F = \sqrt{4\pi n}$ being the Fermi wave vector for a 2D single-component fermionic gas with the density n . Therefore, the physics of the system is completely determined by two dimensionless parameters which are independent ratios of the above lengths. The first parameter $g = a_d/l$ (the ratio of the dipolar length and the interlayer separation) is a measure of the interlayer interaction strength relevant for pairing. In experiments with polar molecules, the values of the dipolar length a_d are of the order of 10^2 – 10^4 nm: for a $^{40}\text{K}^{87}\text{Rb}$ with currently available $d \approx 0.3$ D, one has $a_d \approx 170$ nm (with $a_d \approx 600$ nm for the maximum value $d \approx 0.566$ D), and for $^6\text{Li}^{133}\text{Cs}$ with the tunable dipole moment from $d = 0.35$ D to $d = 1.3$ D in an external electric field ~ 1 kV/cm, the value of a_d varies from $a_d \approx 260$ nm to $a_d \approx 3500$ nm. For the interlayer separation $l = 500$ nm, these values of a_d correspond to $g \lesssim 10$. The second parameter $k_F l$ measures the interlayer separation in units of the mean interparticle distance in each layer. This parameter can also be both smaller (dilute regime) and of the order or larger (dense regime) than unity for densities $n = 10^6$ – 10^9 cm^{-2} (for example, for $l = 500$ nm, one has $k_F l = 1$ for $n \approx 3 \times 10^7$ cm^{-2}). The two parameters g and $k_F l$ determine the regime of interlayer scattering at typical energies of particles (\sim Fermi energy $\varepsilon_F = \hbar^2 k_F^2/2m$), and their product, $gk_F l = a_d k_F$, as usual, controls the perturbative expansion in the system and, therefore, many-body effects.

The interlayer interaction has a very specific form resulting from the anisotropy of the interaction: Two particles from different layers attract each other at short and repel each other at large distances, respectively, as a result of different mutual orientations of their relative coordinate and of their dipole moments. A peculiar property of $V_{2D}(\rho)$ is

$$\int d\rho V_{2D}(\rho) = 0$$

This means that its Fourier transform

$$\tilde{V}_{2D}(\mathbf{q}) = \int d\rho V_{2D}(\rho) e^{-i\mathbf{q}\rho} = -\frac{2\pi\hbar^2}{m} gql e^{-q} \quad (75)$$

vanishes for small q ,

$$\tilde{V}_{2D}(\mathbf{q} \rightarrow 0) \approx -\frac{2\pi\hbar^2}{m} gql \rightarrow 0$$

The potential well at short distances is strong enough to support at least one bound state for any strength of interlayer coupling. For a weak coupling between layers ($g \ll 1$), the bound state is extremely shallow and has an exponentially large size¹²⁷ (see also ref 128):

$$E_b \approx \frac{4\hbar^2}{ml^2} \exp\left[-\frac{8}{g^2} + \frac{128}{15g} - \frac{2521}{450} - 2\gamma + O(g)\right] \quad (76)$$

for the binding energy and

$$R_b = \sqrt{\hbar^2/mE_b} \approx l \exp(4/g^2) \gg l$$

for the size, respectively. However, in the intermediate and strong coupling cases ($g \lesssim 1$) the size of the deepest bound state becomes comparable with the interlayer separation:

$$E_b = (\hbar^2/ml^2) 2g(1 - \sqrt{6/g})$$

and

$$R_b \approx l(6g)^{-1/4}$$

respectively.

The specific properties of the interlayer potential (eq 75): It decays exponentially for large momenta $k \gg l^{-1}$, while it is proportional to k for $k \gg l^{-1}$, leading to different regimes of scattering and, therefore, of the BCS pairing, depending on the relation between g and $k_F l$. This can be conveniently formulated in terms of the vertex function $\Gamma(E, \mathbf{k}, \mathbf{k}')$, where the arguments E , \mathbf{k} , and \mathbf{k}' are independent of each other. This function satisfies the following integral equation¹²⁹

$$\Gamma(E, \mathbf{k}, \mathbf{k}') = V_{2D}(\mathbf{k} - \mathbf{k}') + \int \frac{d\mathbf{q}}{(2\pi)^2} \tilde{V}_{2D}(\mathbf{k} - \mathbf{q}) \times \frac{1}{E - \hbar^2 q^2/m + i0} \Gamma(E, \mathbf{q}, \mathbf{k}') \quad (77)$$

The 2D scattering amplitude $f_k(\varphi)$, where φ is the angle between \mathbf{k} and \mathbf{k}' , corresponds to $(m/\hbar^2)\Gamma(E, \mathbf{k}, \mathbf{k}')$ with $E = \hbar^2 k^2/m = \hbar^2 k'^2/m$. The solution of this equation^{127,128} reads as follows:

For $g < k_F l \lesssim 1$, the leading contribution to scattering is given by the first Born term

$$\Gamma(E, \mathbf{k}, \mathbf{k}') \approx -\frac{2\pi\hbar^2}{m} g|\mathbf{k} - \mathbf{k}'| \quad (78)$$

For $\exp(-1/g^2) \ll kl < g < 1$, the scattering is dominated by the second order Born contribution

$$\Gamma(E, \mathbf{k}, \mathbf{k}') \approx -\frac{2\pi\hbar^2}{m} \frac{g^2}{4} \quad (79)$$

which is momentum and energy independent and, hence, is equivalent to a pseudopotential $V_0(\rho) = -(2\pi\hbar^2/m)(g^2/4)\delta(\rho)$.

For $\exp(-1/g^2) \lesssim kl \ll g < 1$, higher order contributions become important and one has to sum leading contributions from the entire Born series. The result of this summation is

$$\Gamma(E, \mathbf{k}, \mathbf{k}') \approx \frac{2\pi\hbar^2}{m} \frac{2}{\ln(E_b/E) + i\pi} \quad (80)$$

where E_b is the energy of the bound state from eq 76. This expression recovers the standard energy dependence of the 2D low-energy scattering and has a pole at $E = -E_b$, as it should be. The real part of the scattering amplitude, being zero at $E = E_b$, changes from negative to positive values for $E > E_b$ and $E < E_b$, respectively. Note that, within the lowest order terms, a unique expression for the scattering amplitude can be written as

$$\Gamma(E, \mathbf{k}, \mathbf{k}') \approx -\frac{2\pi\hbar^2}{m} \left[g|\mathbf{k} - \mathbf{k}'| - \frac{2}{\ln(E_b/E) + i\pi} \right]$$

As one can see, the interlayer scattering amplitude is negative in the s -wave channel [for the case $\exp(-1/g^2) \lesssim kl \ll g < 1$; this requires $E \sim \varepsilon_F \gg E_b$, which is realistic in the limit $g < 1$]. This means that, at sufficiently low temperatures, the bilayer fermionic dipolar system undergoes a BCS pairing transition into a superfluid state with interlayer s -wave Cooper pairs, characterized by an order parameter $\Delta(\mathbf{p}) \sim \langle \hat{\psi}_-(\mathbf{p}) \hat{\psi}_+(-\mathbf{p}) \rangle$, with $\hat{\psi}_\alpha(\mathbf{p})$ being the field operator in the momentum space, which is independent of the azimuthal angle φ , $\Delta(\mathbf{p}) = \Delta(p)$.

The analysis of the corresponding gap equation was performed in refs 126 and 127 (the latter includes many-body effects), and we present here only the results for the critical temperature T_c in the experimentally most interesting case $k_F l \sim 1$ and $g < 1$, such that $gk_F l = a_d k_F < 1$ (results for other cases can be found in ref)

$$T_c = \frac{2e^\gamma}{\pi} \varepsilon_F \exp\left[-\frac{1}{3\gamma(k_F l)} - \left(\frac{\pi}{4}\right)^2 \frac{f(k_F l)}{\gamma(k_F l)^2}\right] \times \exp\left[-\frac{\pi}{4gk_F l \gamma(k_F l)} \frac{1}{1 - (4/\pi)gk_F l \gamma(k_F l)\Omega(k_F l)}\right] \equiv \frac{2e^\gamma \mu}{\pi} \tau(g, k_F l)$$

where

$$\gamma(x) = \frac{1}{2} \int_0^\pi d\varphi \sin(\varphi) e^{-x \sin(\varphi)} = \frac{\pi}{4} [\mathbf{L}_{-1}(2x) - \mathbf{I}_1(2x)]$$

$\mathbf{L}_n(z)$ and $\mathbf{I}_n(z)$ being the modified Struve and Bessel functions, respectively,

$$\Omega(x) = \frac{1}{2} \int_0^\infty ds \ln|1 - s^2| \operatorname{sign}(s - 1) \frac{d}{dx} [V(s, x)^2]$$

with

$$V(s, x) = \int_0^\pi d\varphi \sqrt{1 + s^2 - 2s \cos \varphi} e^{-x \sqrt{1 + s^2 - 2s \cos \varphi}}$$

and the function $f(x)$ is shown in Figure 19. The dependence of the function $\tau(g, k_{Fl})$ on k_{Fl} for several values of g is shown in

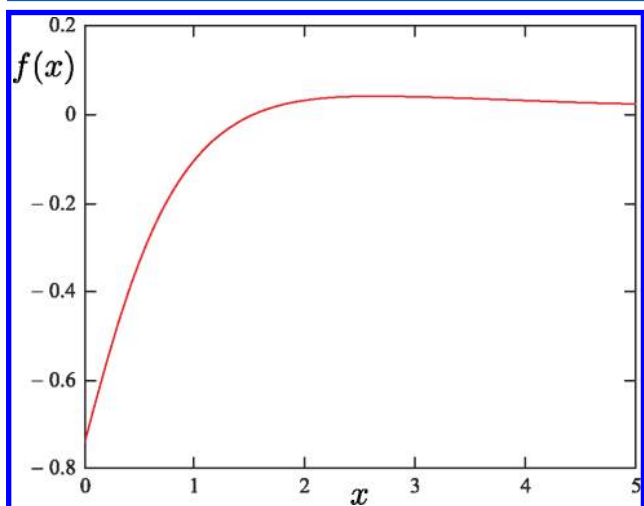


Figure 19. The function $f(x)$. (Taken from ref 127.)

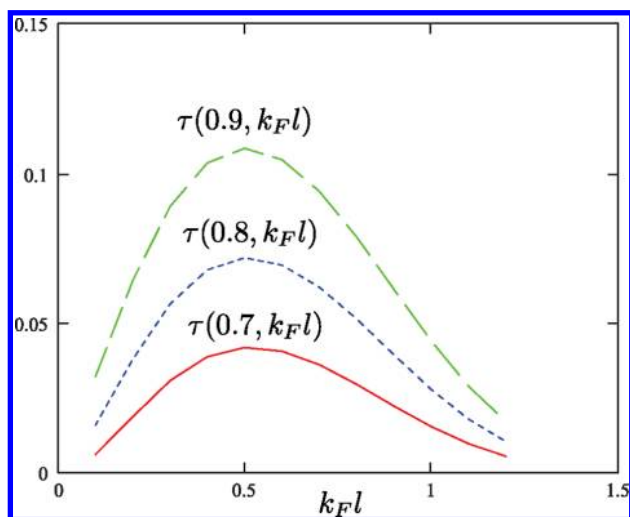


Figure 20. The function $\tau(g, x)$ for $g = 0.7$ (solid line), $g = 0.8$ (short-dashed line), and $g = 0.9$ (long-dashed line). (Taken from ref 127.)

Figure 20. We see that the critical temperature decreases very rapidly for $k_{Fl} > 1$ due to the fast decay of the scattering amplitude. The optimal value of k_{Fl} is around 0.5, with the critical temperature reaching values of the order of 0.1μ for $g \approx 0.9$, which corresponds to $gk_{Fl} \approx 0.45 < 1$.

This BCS state with interlayer Cooper pairs occurs in the weak (interlayer) coupling regime when the size of the bound state is larger than the interparticle separation (in other words, the Fermi energy is larger than the binding energy). With increasing interlayer coupling, the BCS state smoothly transforms into a BEC state of tightly bound interlayer molecules when the interparticle separation is larger than the size of the bound state; see, for example, refs 126 and 130. Of course, the BEC regime and BEC-BCS crossover are possible only when the mean interparticle separation in each layer is larger than the distance between the layers.

Let us now discuss possible physical realizations of the interlayer pairing. In the experiments with polar molecules, the

values of the dipolar length a_d are of the order of 10^2 – 10^4 nm: for a $^{40}\text{K}^{87}\text{Rb}$ with currently available $d \approx 0.3$ D, one has $a_d \approx 170$ nm (with $a_d \approx 600$ nm for the maximum value $d \approx 0.566$ D), and for $^6\text{Li}^{133}\text{Cs}$ with a tunable dipole moment from $d = 0.35$ D to $d = 1.3$ D (in an external electric field ~ 1 kV/cm), the value of a_d varies from $a_d \approx 260$ nm to $a_d \approx 3500$ nm. For the interlayer separation l of the order of a few hundred nanometers, the corresponding values of the parameter g can be both smaller and larger than unity ($g \lesssim 10$).

The values of the parameter k_{Fl} are also within this range for densities $n = 10^6$ – 10^9 cm^{-3} (for example, one has $k_{Fl} = 1$ for $l = 500$ nm and $n \approx 3 \times 10^7$ cm^{-3}). Note, however, that the optimal values of this parameter are around $k_{Fl} \sim 0.5$ (see Figure 20), and hence, the optimum value of the interlayer separation is related to the density, which, in turn, should be large enough to provide a substantial value for the Fermi energy. For $^{40}\text{K}^{87}\text{Rb}$ molecules at the density $n \approx 4 \times 10^8$ cm^{-3} , in each layer one has $\epsilon_F \approx 100$ nK and $k_F =$. Therefore, the interlayer separation l should be relatively small, $l \lesssim 150$ nm, to meet the optimal conditions. For $l = 150$ nm one then has $g \approx 1.1$ (with current $d \approx 0.3$ D), $k_{Fl} \approx 1$, and $T_c \approx 0.1\epsilon_F \approx 10$ nK. Note that strictly speaking these values of parameters g and k_{Fl} do not correspond to the weak coupling regime considered in this paper, but rather to the intermediate regime of the BCS-BEC crossover. However, based on the experience with the BEC-BCS crossover in two-component atomic fermionic mixtures, in which the critical temperature continues to grow when approaching the crossover region from the BCS side, we could expect that the above value of the critical temperature provides a good estimate for the onset of the superfluidity in the intermediate coupling regime.

4.8. Stability of Fermionic Dipolar Systems

As we have already mentioned, a polarized homogeneous fermionic dipolar gas becomes unstable for strong dipole-dipole interaction ($a_d k_F > 1$). Unfortunately, for this strongly interacting regime, the usage of the Hartree-Fock approximation could not be rigorously justified. It is commonly accepted, however, that the Hartree-Fock method is able to provide a correct qualitative picture even in this regime, although its quantitative results should be taken with care.

The simplest way to get quantitative insight into the instability region for a 3D dipolar gas is to use the variational ansatz (eq 46) to calculate the compressibility. It turns out^{93,94} that the compressibility of a homogeneous gas becomes negative for $a_d k_F > 9.5$, signaling the instability of the gas and leading to a collapse.

For a trapped gas with N particles,⁹² the ansatz (eq 46) for the momentum distribution has to be generalized to the ansatz for the Wigner distribution function

$$n(\mathbf{r}, \mathbf{p}) = \theta \left[p_F(\mathbf{r})^2 - \frac{1}{\alpha} (p_x^2 + p_y^2) - \alpha^2 p_z^2 \right]$$

where $p_F(\mathbf{r})^2 = p_F^2 - \lambda^2 l_{\omega}^{-4} [\beta(x^2 + y^2) - \beta^{-2} z^2]$ is the position-dependent square of the Fermi momentum, λ and β are variational parameters, $p_F = (48N)^{1/6} \lambda^{1/2} \hbar / l_{\omega}$, and $l_{\omega} = (\hbar / m\omega)^{1/2}$ with $\omega = (\omega_{\rho}^2 \omega_z)^{1/3}$. Minimization of the energy with respect to the variational parameters α , β , and λ gives equilibrium density and local momentum distribution for a given value of the trap aspect ratio $l = (\omega_{\rho} / \omega_z)^{1/2}$. The calculation of the compressibility shows that it becomes negative for any value of the trap aspect ratio l provided the value of the parameter $N^{1/6} a_d / l_{\omega}$, which measures the strength

of interparticle interaction, is sufficiently large. The dependence of the critical value of $N^{1/6}a_d/l_\omega$ on the trap aspect ratio l is shown in Figure 21. Note that the critical aspect ratio found in

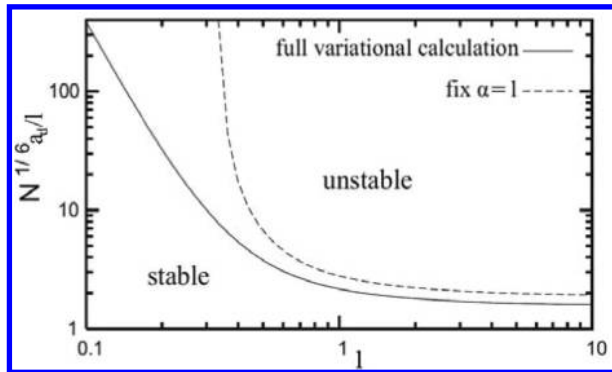


Figure 21. Critical value of $N^{1/6}a_d k_F$ as a function of the trap aspect ratio l . The solid line represents the full variational calculation, while the dashed line is obtained by forcing $\alpha = 1$. (Taken from ref 92. Copyright 2008 American Physical Society.)

ref 131, $l_c = 0.19$, below which the trapped gas is stable for any value of $N^{1/6}a_d/l_\omega$ is an artifact of the approximation used in this paper resulting from neglecting the deformation of the local momentum distribution; see discussion in ref 92.

In a dipolar monolayer, the calculations of the compressibility in ref 115 show that the collapse of the system takes place for $a_d k_F \approx 1$ for $\theta = \pi/2$ (dipoles are oriented parallel to the plane) but for rapidly increasing values of $a_d k_F$ when the angle between the dipole polarization and the plane increases. More careful analysis of both long wavelength (collapse) and finite wavelength (density wave) instabilities of a dipolar monolayer can be performed by looking at the stability of the collective modes: A collective mode becomes unstable when its frequency tends to zero. The corresponding equation valid for a general wave vector \mathbf{k} of the collective mode reads

$$\gamma_{\mathbf{k}}(\mathbf{p}) = \int \frac{d\mathbf{p}'}{(2\pi\hbar)^2} \tilde{\Gamma}(\mathbf{k}, \mathbf{p}, \mathbf{p}') \times \frac{n(\mathbf{p}') - n(\mathbf{p}' + \hbar\mathbf{k})}{\hbar\omega + \varepsilon(\mathbf{p}') - \varepsilon(\mathbf{p}' + \hbar\mathbf{k})} \gamma_{\mathbf{k}}(\mathbf{p}') \quad (81)$$

where $\tilde{\Gamma}(\mathbf{k}, \mathbf{p}, \mathbf{p}') = V_d^{2D}(\hbar\mathbf{k}) - V_d^{2D}(\mathbf{p} - \mathbf{p}' + \hbar\mathbf{k})$ for our case. [Note that eq 52 follows from eq 81 after taking the limit $k \rightarrow 0$ and using the relation $\kappa(\mathbf{p}) = [\omega - \mathbf{k} \cdot \nabla_{\mathbf{p}} \varepsilon(\mathbf{p})] \gamma_{\mathbf{k}}(\mathbf{p})$]. As a result, an instability occurs when the equation

$$\gamma_{\mathbf{k}}(\mathbf{p}) = \int \frac{d\mathbf{p}'}{(2\pi\hbar)^2} \tilde{\Gamma}(\mathbf{k}, \mathbf{p}, \mathbf{p}') \frac{n(\mathbf{p}') - n(\mathbf{p}' + \hbar\mathbf{k})}{\varepsilon(\mathbf{p}') - \varepsilon(\mathbf{p}' + \hbar\mathbf{k})} \gamma_{\mathbf{k}}(\mathbf{p}') \quad (82)$$

has a nontrivial solution for some value of \mathbf{k} . Note that, for $\tilde{\Gamma}(\mathbf{k}, \mathbf{p}, \mathbf{p}') = V_d^{2D}(\hbar\mathbf{k})$ (when only the direct interaction is taken into account and the exchange one is neglected), $\gamma_{\mathbf{k}}(\mathbf{p})$ is \mathbf{p} -independent and eq 81 reduces to

$$1 - V_d^{2D}(\hbar\mathbf{k}) \Pi(\omega, k) = 0 \quad (83)$$

where

$$\Pi(\omega, k) = \int \frac{d\mathbf{p}'}{(2\pi\hbar)^2} \frac{n(\mathbf{p}') - n(\mathbf{p}' + \hbar\mathbf{k})}{\hbar\omega + \varepsilon(\mathbf{p}') - \varepsilon(\mathbf{p}' + \hbar\mathbf{k})}$$

is the 2D polarization operator. Equation 83 is used to study long wavelength ($k \rightarrow 0$) plasmon oscillations in electrically charged systems (see, for example, ref 132). Although keeping only direct interaction in the long wavelength limit is legitimate for Coulomb systems (because of divergence of the Coulomb interaction, while the exchange one is finite due to nonzero momentum transfer, $|\mathbf{p} - \mathbf{p}'| \sim p_F$), this approximation gives physically incorrect results in a Fermi system with a finite Fourier component of the interparticle interaction for small momentum transfer (like in the considered case of a dipolar monolayer). In this case, the direct and the exchange contributions are of the same order and keeping only the former results in unphysical results. Actually, for a short-range interparticle interaction (with a momentum-independent Fourier component), the two contributions cancel each other, as it should be in a single-component Fermi gas. Similar considerations are also applied to the analysis of instabilities in dipolar systems on the basis of eq 82: Keeping the exchange contribution in this equation is essential in order to obtain correct results consistent with fermionic statistics of particles..

For $k \rightarrow 0$, eq 82 is equivalent to the Pomeranchuk criterion^{91,90} formulated in the framework of a Landau Fermi-liquid. Numerical solution of this equation (for $k = 0$)⁹⁷ shows that the instability of the system for $\theta \gtrsim 3\pi/8$ corresponds to mostly isotropic with some addition of the quadrupole ($\sim \cos 2\varphi$) deformation of the Fermi surface, i.e. to the collapse, that takes place for $a_d k_F \gtrsim 1$ (see Figure 22)

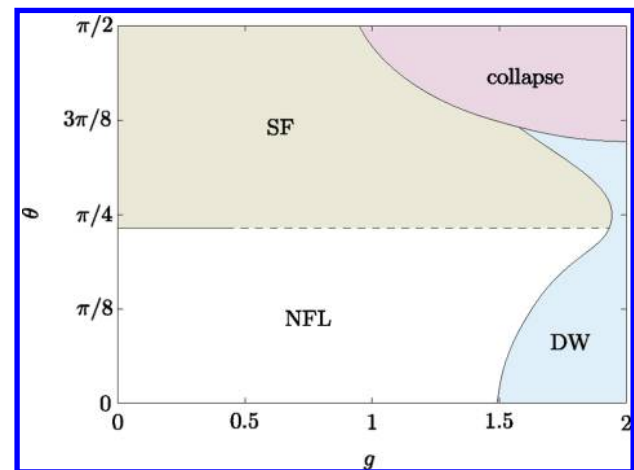


Figure 22. Phase diagram of the 2D dipolar Fermi gas at $T = 0$. For $0 \leq a_d k_F \lesssim 1.5$ and small tilting angles θ , the system is a normal Fermi liquid (NFL). The transition to the superfluid state (SF) occurs at the critical angle $\theta_c = 0.72$. At moderately strong interactions, the system either collapses or undergoes the transition into the density-wave phase (DW). (Taken from ref 97.)

For $\theta \lesssim 3\pi/8$, the leading instability corresponds to the p -wave ($\sim \sin \varphi$) deformation of the Fermi surface. However, this instability is unobservable because for these values of the tilting angle θ the system undergoes a density-wave instability at smaller values of $a_d k_F$.¹³³ This instability corresponds to a nontrivial solution of eq 82 with finite k and takes place for $a_d k_F \gtrsim 1.5$. For $0 < \theta \lesssim 3\pi/8$, the corresponding vector \mathbf{k} is along the y -axis ($\phi_{\mathbf{k}} = \pm\pi/2$) and has a modulus that is twice larger than the Fermi wave-vector in the y -direction, $\mathbf{k} = \hbar^{-1} 2p_F(\pi/2) \mathbf{e}_y$. For $\theta = 0$ (isotropic case), the instability vector \mathbf{k} has no preferable directions and the system is believed to become

unstable against formation of a crystalline state with a triangular lattice.

5. DIPOLAR MULTILAYER SYSTEMS

Let us now briefly discuss known results on dipolar multilayer systems. The stability against formation of inhomogeneous (density wave) phases in a fermionic dipolar multilayer system was discussed in ref 134 for a particular choice of the tilting angle $\theta = \arccos 1/\sqrt{3}$ and in ref 135 for an arbitrary θ . The analysis of these papers show that inclusion of exchange interactions tends to stabilize the homogeneous state, resulting in higher values of critical dipolar interaction strength as compared to the simple random-phase-approximation (RPA) approach. On the other hand, for multiple layers, this critical dipolar interaction strength decreases with the number of layers.

Another interesting feature of multilayer systems of dipoles is the formation of many-body bound states in the form of a chain (or filament) made of one dipole in each layer.^{136–139} (It was argued in ref 138 that bound states involving two molecules from the same layer do not exist.) The binding energy of such chains increases with the number of involved molecules (or layers). As a result, the ground state contains chains of maximum length, while, at finite temperatures, the competition between entropy that favors shorter chains and energy preferring longer ones results in a nonmonotonic dependence of the distribution on the length of the chains. For bosonic dipoles, quantum fluids of such self-assembled chains (dipolar chains fluid) and superfluidity of dipolar chains was considered in ref 136. For fermionic dipoles, the situation is even more interesting because chains with an even number of dipoles are bosons, while those with an odd number of dipoles are fermions. In this case, even at zero temperature, there is an interplay between the Fermi statistics, in the form of a Pauli principle giving rise to a finite kinetic energy of a filled Fermi sphere, and the binding energy; see ref 137, where a Bose–Fermi mixture of self-assembled noninteracting chains was considered for the simple case of a three-layer system of fermionic polar molecules oriented perpendicular to the layers. For a more general case for both bosonic and fermionic dipoles, which also includes interactions between chains, see ref 139.

The superfluidity in fermionic dipolar multilayer systems was addressed in ref 140. The interlayer character of Cooper pairs in this case leads to the competition for pairing among adjacent layers resulting in a dimerized superfluid state as the ground state, in which the system can be viewed as a stack of bilayers with interlayer pairing correlations inside each bilayer and no such correlations between layers belonging to different bilayers. This state is characterized by a quasi-long-range superfluid order in every bilayer. At some finite critical temperature, this phase undergoes a phase transition into a dimerized “pseudogap” phase with only short-range superfluid correlations. These correlations disappear above the second critical temperature, and the system is in the normal phase (see details and proposals for experimental detections of the phases and phase transitions in ref 140).

6. STRONGLY INTERACTING DIPOLAR GAS

Strong correlations are at the core of a number of fundamental phenomena in many-body physics, ranging from the formation of self-assembled ionic crystals to exotic phases such as high- T_c superconductivity and spin liquids. The regime of strong

correlations between particles in a gas is generally obtained when the strength of the interparticle interactions becomes comparable to, or larger than, the average kinetic energy. There are two main avenues to achieve this regime of strong correlations: (i) the first is to decrease the kinetic energy by placing particles on a lattice—which in the case of a dilute gas has the effect of increasing the effective mass—and (ii) the second is to increase the relative strength of interactions. In gases of dipolar particles, strong correlations can be achieved either way. In the following, we first discuss the phase diagram for dipoles confined to 2D with tunable interactions (section 6.1), and then we review several works on exotic many-body phases for interacting dipoles trapped in an optical lattice; section 6.2.

6.1. Two-Dimensional Dipoles: Phase Diagram

The conceptually simplest example, although remarkably rich from a physics point of view, is a system of cold polar molecules in a dc electric field under strong transverse confinement. The setup is illustrated in Figure 2a. A weak dc field along the z -direction induces a dipole moment d in the ground state of each molecule. These molecules interact via the effective dipole–dipole interaction $V_{\text{eff}}^{\text{DD}}(r) = D(r^2 - 3z^2)/r^5$ according to their induced dipoles, with $D = d^2$. For molecules confined to the x,y -plane perpendicular to the electric field, this interaction is purely repulsive. For molecules displaced by $z > r/\sqrt{3}$, the interaction becomes attractive, resulting in few-body and many-body instabilities. As discussed in section 2.2, these instabilities can be suppressed by a sufficiently strong 2D confinement with the potential $V_{\text{trap}}(z_i)$ along z , due to, for example, an optical force induced by an off-resonant light field.⁶⁴

The 2D dynamics in this pancake configuration is described by the Hamiltonian

$$H_{\text{eff}}^{2\text{D}} = \sum_i \frac{p_{\rho i}^2}{2m} + \sum_{i < j} V_{\text{eff}}^{2\text{D}}(\rho_{ij}) \quad (84)$$

which is obtained by integrating out the fast z -motion. Equation 84 is the sum of the 2D kinetic energy in the x,y -plane and the repulsive 2D dipolar interaction

$$V_{\text{eff}}^{2\text{D}}(\rho) = d^2/\rho^3 \quad (85)$$

with $\rho_{ij} \equiv (x_j - x_i, y_j - y_i)$ a vector in the x,y -plane (solid line in Figure 3a). The distinguishing feature of the system described by the Hamiltonian (eq 84) is that tuning the induced dipole moment d drives the system from a weakly interacting gas (a 2D superfluid in the case of bosons or a 2D Fermi liquid¹⁴²) to a crystalline phase in the limit of strong repulsive dipole–dipole interactions. This transition and the crystalline phase have no analog in the atomic Bose gases with short-range interactions modeled by a pseudopotential of a given scattering length.

A crystalline phase corresponds to the limit of strong repulsion where particles undergo small oscillations around their equilibrium positions, which is a result of the balance between the repulsive long-range dipole–dipole forces and an additional (weak) confining potential in the x,y -plane. The relevant parameter is

$$r_d \equiv \frac{E_{\text{pot}}}{E_{\text{kin}}} = \frac{d^2/a^3}{\hbar^2/ma^2} = \frac{d^2 m}{\hbar^2 a} = \frac{a_d}{a} \quad (86)$$

which is the ratio of the interaction energy and the kinetic energy at the mean interparticle distance a . This parameter is tunable as a function of d from small r_d to large. A crystal forms

for $r_d > 1$, when interactions dominate, which for a dipolar crystal is the limit of large densities. This density dependence is different from that in Wigner crystals with $1/r$ -Coulomb interactions, as realized, e.g., with laser cooled trapped ions.¹⁴³ In the latter case, $r_c = [(e^2/a)/\hbar^2]/ma^2 \sim a$, and the crystal forms at low densities. In addition, the charge e is a fixed quantity, while d can be varied as a function of the dc field.

Figure 23 shows a schematic phase diagram for a dipolar gas of bosonic molecules in 2D as a function of r_d and temperature

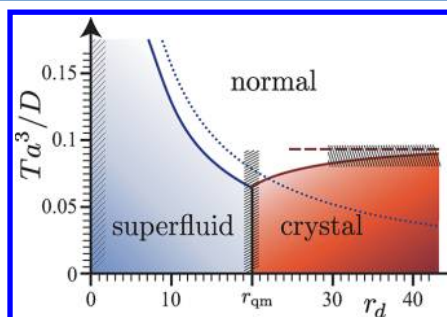


Figure 23. Tentative phase diagram for bosonic dipoles in 2D (see setup in Figure 2) in the T - r_d plane: crystalline phase for interactions $r_d > r_{QM}$ and temperatures below the classical melting temperature T_m (dashed line).¹⁴¹ The superfluid phase appears below the upper bound $T < \pi\hbar^2 n/2m$ (dotted line).^{116,117} The crossover to the unstable regime for small repulsion and finite transverse confinement Ω for polar molecules is indicated (hatched region). Hatched regions for $r_d \sim r_{qm}$ and at the crystal-normal phase transitions correspond to the existence of possible exotic phases (see the Open Questions section in the text). (Adapted from ref 64.)

T . In the limit of weak interactions $r_d < 1$, the ground state is a superfluid (SF) with a finite (quasi-)condensate. The SF is characterized by a superfluid fraction $\rho_s(T)$, which depends on temperature T , with $\rho_s(T=0) = 1$. A Berezinskii-Kosterlitz-Thouless transition^{116,117} from the superfluid to a normal fluid occurs at a finite temperature $T_{KT} = \pi\rho_s\hbar^2 n/2m$, as expected in two dimensions. Recent numerical results in ref 144 obtained with an exact Path-Integral Monte Carlo technique (PIMC)¹⁴⁵ have shown that the superfluid fraction $\rho_s(T)$, and thus T_{KT} , has a nonmonotonic behavior as a function of the interaction strength r_d , reaching a maximum of about $\rho_s(T_{KT}) = 0.9$ at $r_d \simeq 1$.

In the opposite limit of strong interactions $r_d \gg 1$, the polar molecules are in a crystalline phase for temperatures $T < T_m$ with $T_m \approx 0.089D/a^3$; see ref 141. The configuration with minimal energy is a triangular lattice with excitations given by acoustic phonons, with characteristic Debye frequency $\hbar\omega_D/(h^2/ma^2) \dots 7.9\sqrt{r_d}$. The intermediate strongly interacting regime with $r_d > 1$ has been investigated using several numerical, especially quantum Monte Carlo, techniques in refs 64 and 146–149. Using an exact PIMC technique, a quantum melting transition from the crystalline to the superfluid phases has been determined to occur at a critical interaction strength $r_{QM} = 18 \pm 4$.⁶⁴

Confined Geometries. The addition of an in-plane parabolic confinement of frequency ω_{\parallel} as realized in experiments with magnetic or optical traps introduces a term $\sum_i m\omega_{\parallel}^2 r_i^2/2$ in eq 84. The strength of interactions is now characterized by the dimensionless ratio $\tau = (a_d/l)^2$, with $l = (\hbar/m\omega_{\parallel})^{1/2}$ the harmonic oscillator length. The physics of classical mesoscopic crystals with $\tau \gg 1$ and dominant thermal

fluctuations has been first discussed in the context of excitonic materials.^{151–154} It was found that small dipolar clusters with $N < 40$ particles confined to parabolic potentials may not crystallize in a triangular lattice, but rather arrange in shell-like structures. Finite- T melting of these structures would usually proceed through two separate (nonsmooth) transitions, corresponding to the loss of rotational and radial order.

Motivated by dipolar molecular and atomic gases, the focus has now shifted toward the low-temperature regime of dominant quantum fluctuations.^{150,152,155–159} For bosons, it was recently determined^{156,150} that the quantum melting of mesoscopic crystals ($\tau \gg 1$) into a superfluid ($\tau \lesssim 1$) is a sharp crossover involving two intermediate phases: these are ring-crystals, with vanishing superfluid fraction, and mesoscopic superfluids with a modulated (e.g., nonhomogeneous) density. Snapshots of quantum Monte Carlo simulations for $N = 13$ particles are shown in Figure 24 for all of these quantum phases.

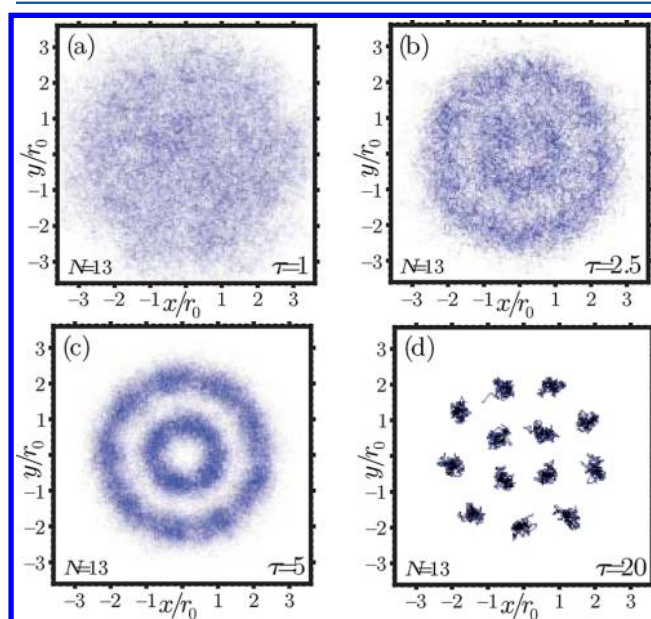


Figure 24. (a–d) Monte Carlo snapshots of the density of particles in all mesoscopic phases for $N = 13$ dipoles, as a function of the effective mass τ : (a) superfluid; (b) supersolid; (c) ringlike crystals; (d) classical crystal. (Image taken from ref 150. Copyright 2010 American Physical Society.)

Having determined the low-temperature phase-diagram both in the homogeneous situation and in confined geometries, the remaining question is whether these phases, and in particular the crystalline phase emerging at strong dipole-dipole interactions, are in fact accessible with polar molecules. As discussed in section 2.2, stable 2D configurations for the molecules exist in the parameter region where the combination of strong dipole-dipole interactions and transverse (optical) trapping confines the particles' motion to the large distance region with $a > l_{\perp}$, with $l_{\perp} \dots (12d^2/m\Omega^2)^{1/5}$ the position of the saddle points in Figure 3b (white circles). For a given induced dipole d , the ground-state of an ensemble of polar molecules is thus a crystal for mean interparticle distances $l_{\perp} < a < a_{max}$ where $a_{max} \equiv d^2m/\hbar^2r_{QM}$ corresponds to the distance at which the crystal melts into a superfluid. For SrO (RbCs) molecules with permanent dipole moment $d = 8.9$ D ($d = 1.25$ D), $a_{min} \dots 200$ nm (100 nm), while a_{max} can be several micrometers. Since

for large enough interactions the melting temperature T_m can be of the order of several microkelvin, the self-assembled crystalline phase should be accessible for reasonable experimental parameters using cold polar molecules.

Open Questions. Remarkably, there are still important open questions concerning the phase diagram of two-dimensional dipoles and, in particular, the order of the phase transitions between the solid and liquid phases at zero and finite temperature. While, as often happens,³ numerical results are usually consistent with direct first order transitions, exotic intermediate phases may occur in either case: (i) *At finite $T \dots T_m$* , an intermediate *hexatic* phase characterized by a short-range positional and a quasi-long-range orientational (6-fold) order may exist between the solid and the isotropic liquid phases. Evidence for this hexatic phase, originally proposed by Kosterlitz, Thouless, Halperin, Nelson, and Young,^{117,160,161} has been recently found numerically in ref 162. (ii) *At low-temperature*, theoretical results suggest the presence of an intermediate *microemulsion bubble phase* between the superfluid and the solid. First introduced in the context of 2D electron gases in Si MOSFETs by Spivak and Kivelson¹⁶³ and never observed so far (however, see below), a microemulsion should prevent a first order transition in two dimensions. The observation of either phase with cold dipolar gases would constitute a breakthrough for condensed matter theory.

Strong correlations can also occur in weakly interacting dipolar gases subject to rotation,^{164–168} which, as extensively reviewed in ref 32, represents a key element to engineer effective magnetic fields in ultracold atomic and molecular gases. Strongly correlated phases similar to the Laughlin quantum Hall states have been proposed in ref 165 for dipolar bosons and for in ref 169 for dipolar fermions, while the transition from the Laughlin liquid state to a dipolar crystal state was addressed in ref 170. Recent work¹⁷¹ has now provided quantitative estimates for the realization of Abelian and non-Abelian gauge fields with polar molecules.

6.2. Optical Lattices

Hubbard Hamiltonians are model Hamiltonians describing the low-energy physics of interacting fermionic and bosonic particles in a lattice.¹⁷² They have the general tight-binding form

$$H = - \sum_{i,j,\sigma} J_{ij}^{\sigma\sigma'} b_{i,\sigma}^\dagger b_{j,\sigma} + \sum_{i,j,\sigma,\sigma'} \frac{U_{ij}^{\sigma\sigma'}}{2} n_{i,\sigma} n_{j,\sigma'} \quad (87)$$

Here $b_{i,\sigma}$ ($b_{i,\sigma}^\dagger$) are the destruction (creation) operators for a particle at site i in the internal state σ , $J_{ij}^{\sigma\sigma'}$ describes coherent hopping of a particle from site i to site j (typically the nearest neighbor), and $U_{ij}^{\sigma\sigma'}$ describes the onsite ($i = j$) or offsite ($i \neq j$) two-body interactions between particles, with $n_{i,\sigma} = b_{i,\sigma}^\dagger b_{i,\sigma}$. Hubbard models have a long history in condensed matter physics, where they have been used as tight-binding approximations of strongly correlated systems. For example, for a system of electrons in a crystal hopping from the orbital of a given atom to that of its nearest neighbor, σ represents the electron spin. A (fermionic) Hubbard model comprising electrons in a 2D lattice with interspecies, on-site interactions are thought to be responsible for the high-temperature superconductivity observed in cuprates.¹⁷³

In recent years, Hubbard models have been shown to provide excellent *microscopic* descriptions of the low-energy physics of interacting bosonic and fermionic atoms trapped at the bottom

of an optical lattice.^{174,175} Since the interactions between cold atoms are short-ranged, in these systems the Hubbard Hamiltonian typically has *on site* interactions only ($U_{ii}^{\sigma\sigma'}$ in eq 87). This is readily shown for the simple case of single-species ($\sigma = \sigma'$) bosonic atoms with contact interactions, such as ¹³³Cs atoms prepared in their absolute internal (hyperfine, fine, ...) ground state, and trapped in the lowest band of an optical lattice. In the limit in which all energies involved in the system dynamics are small compared to excitation energies to the second band and neglecting the often-small overlap beyond nearest neighboring densities, the microscopic many-body Hamiltonian reduces to one of the form of eq 87 with nearest-neighbor hopping energy $J = J_{i,i+1}^{\sigma}$ and on-site interactions $U = U_{ii}^{\sigma\sigma}$ ¹⁷⁴ with

$$J = - \int w_i^*(r) \left(-\frac{\hbar^2 \Delta}{2m} + V_0(r) \right) w_{i+1}(r) d^3r, \\ U = \frac{4\pi a_s \hbar^2}{m} \int |w_i(r)|^4 d^3r \quad (88)$$

Here, $\{w_i(\mathbf{r})\}$ is a complete set of single-particle basis functions, known as *Wannier* functions, which are linear combinations of exact solutions of the Schrödinger equation in the periodic optical potential $V_0(r) = \sum_{\alpha=1,3} V_{0,\alpha} \sin^2(k_\alpha x_\alpha)$ (known as Bloch functions) and are localized at individual sites j (here we focus on the lowest lattice band only). The optical lattice has a depth $V_{0,\alpha}$ proportional to the intensity of the confining laser beams, with wavevector k_α . In atomic systems, the Hamiltonian parameters in eq 88 can then be accurately controlled independently using external (optical, magnetic) fields: by increasing the intensity of the lattice laser light, J decreases exponentially, while U can be broadly tuned, e.g., by varying the scattering length a_s using magnetic Feshbach resonances.³

The resulting Bose–Hubbard Hamiltonian (BHH) has been extensively studied in condensed matter physics.^{3,176} When the atom number is commensurate with the number of lattice sites, the BHH predicts a zero-temperature phase transition from a superfluid (SF) phase to a Mott insulator (MI) with an increasing ratio of the on site interaction U (due to repulsion of atoms) to the tunneling matrix element J . In the MI phase, the density (occupation number per site) is pinned at an integer value $n = 1, 2, \dots$, and the excitation spectrum shows a gap of the order of U , corresponding to particle–hole excitations. When the density is not integer, the low-energy phase is superfluid for all strengths of the ratio J/U . The associated phase diagram is sketched in Figure 25 as a function of the chemical potential μ and the ratio J/U , the lobes denoting MI regions of constant density.

Spectacular experiments with ultracold atoms have led to the first observation and characterization of this superfluid/Mott-insulator quantum phase transition for bosonic atoms,^{177–179} by looking at the interference of the expanded cloud, the measurement of the gapped excitations, and the (lack of) conductivity in the Mott phase. Further experimental work with fermions may resolve the phase diagram of the fermionic Hubbard model in 2D by performing an *analog quantum simulation* of eq 87 with two-species of cold fermions.^{180–182}

6.2.1. Dipoles on a 2D Lattice Monolayer. The long-range and anisotropic character of dipole–dipole interactions adds to the Bose–Hubbard model new possibilities to observe quantum phases of fundamental interest. The simplest case is that of an ensemble of single-species dipoles ($\sigma = \sigma'$) which are all polarized perpendicular to the lattice plane, resulting in

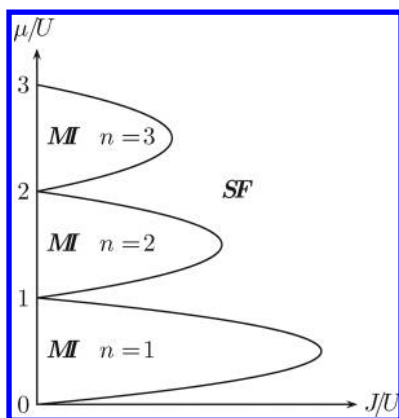


Figure 25. (a) Sketch of the phase diagram of the Bose–Hubbard model at $T = 0$ in the plane μ/U vs J/U . The regions MI denote Mott insulator phases, with an integer average onsite density n . (Adapted from ref 34. Copyright 2009 IOP Publishing.)

isotropic in-plane interactions. This adds to the BH Hamiltonian terms of the kind $\sum_{i<j} U_{ij}^{\sigma\sigma} n_i^{\sigma} n_j^{\sigma}$, with $U_{ij}^{\sigma\sigma} = V/r_{ij}^3$.

Extended Hubbard models have been extensively studied in the literature. It has been predicted that in 2D lattices the presence of finite range interactions gives rise to novel quantum phases, like the charge-density wave (checkerboard), which is an insulating phase with modulated density, and the supersolid (SS) phase, with coexistence of superfluidity and of a periodic spatial modulation of the density, different from the one of the lattice.¹⁸⁴ This latter phase has a particularly interesting and storied history. First proposed in the context of the search for the ground state of helium, it has been the subject of extended theoretical and experimental investigations for almost 40 years. While recent experiments may have spotted it in bulk solid helium, its very own existence in free-space, that is in the absence of an underlying periodic potential, is a matter of active research and debate. With few exact theoretical tools available in the strongly interacting regime, quantum Monte Carlo (QMC) methods have so far established SS behavior in free-space to be based on defects and disorder mechanisms, such as the presence of superfluid dislocations and grain boundaries.¹⁸⁵ Crucially, any commensurate bulk solid (including ^4He) should be insulating,¹⁸⁶ notwithstanding recent theoretical proposals.¹⁸⁷

Several theoretical studies have demonstrated SS behavior in tight-binding lattice models.^{183,184,188–198} Model systems with nearest-neighbor (NN) or next-neighbour-neighbor (NNN) interactions have been generally considered. The variety of theoretical models and techniques which have been used has resulted in a zoo of predictions. A general conclusion is that SS behavior seems to be favored by finite-range interactions as well as finite on-site interactions, $U_{ii}^{\sigma\sigma} > J_{i,i+1}^{\sigma}$. Quantum Monte Carlo methods have determined the SS to occur for the following models: (i) *hard-core bosons* (infinitely large $U_{ii}^{\sigma\sigma}$) on a triangular lattice with NN interactions only, for densities comprised between $1/3 < n < 2/3$; (ii) *hard-core bosons* on a square lattice with NN and NNN interactions for $n < 0.25$ and $0.25 < n < 0.5$ between a “star” and a “stripe” solid at half filling; (iii) *soft-core bosons* (finite value of the ratio $U_{ii}^{\sigma\sigma} > J_{i,i+1}^{\sigma}$) on a square lattice with NN and $n > 0.5$. *Phase separation*, characterized by a negative compressibility, has been predicted to occur in several models, for example in the latter case (iii) with NN interactions and $n < 0.5$. However, its origin can be traced back to the finite-range character of the interactions (NN) considered in that

specific model, and thus, phase-separation may be expected to disappear in the case of the infinite-range interactions considered below.

Dipolar atomic and molecular gases trapped in optical lattices can provide physical systems where the dynamics is *microscopically* described by extended-Hubbard Hamiltonians with long-range, anisotropic, interactions,¹⁹⁹ with Hamiltonian parameters tunable with external fields. In particular, polar molecules in optical lattices can provide for strong offsite dipolar interactions, of the order of hundreds of kHz, decaying with distance as $1/r^3$. Due to these strong interactions, two molecules cannot hop onto the same site, and thus, the particles may be treated as effectively “hard-core” (soft-core particles may be realized with dipolar magnetic atoms). For a lattice of 2D polarized hard-core dipoles, the microscopic extended Bose–Hubbard Hamiltonian in the presence of long-range interactions is

$$H = -J \sum_{\langle i,j \rangle} b_i^\dagger b_j + V \sum_{i<j} \frac{n_i n_j}{r_{ij}^3} - \mu \sum_i n_i \quad (89)$$

The phase diagram of eq 89 has been recently computed for 2D triangular¹⁹¹ and square¹⁸³ lattices using exact QMC methods and no cutoff in the range of interactions. The zero-temperature phase diagram on a square lattice is shown in Figure 26. For large enough J/V , the low-energy phase is

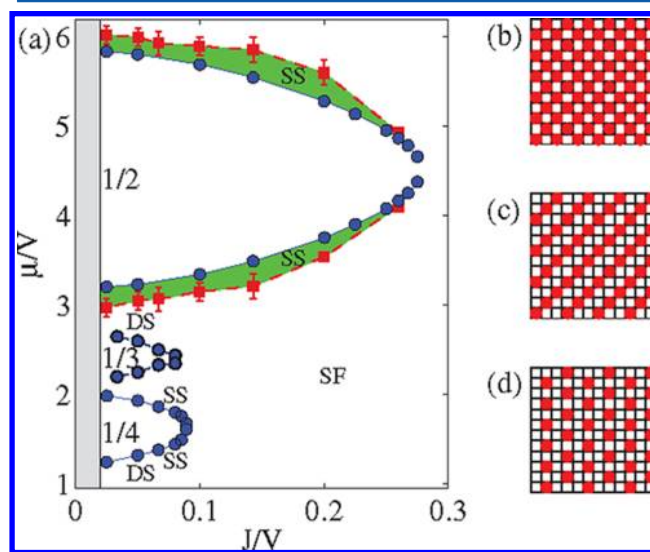


Figure 26. (a) Phase diagram of the microscopic extended Bose–Hubbard Hamiltonian (eq 89) at $T = 0$. Lobes: Mott solids (densities indicated): SS, supersolid phase; SF, superfluid phase; DS, devil’s staircase. Panels b–d: sketches of the ground state configuration for the Mott solids in panel a, with densities $n = 1/2$, $1/3$, and $1/4$, respectively. (Image adapted from ref 183. Copyright 2010 American Physical Society.)

superfluid, for all μ . For finite J , three main solid Mott lobes emerge with densities $n = 1/2$, $1/3$, and $1/4$. These are the checkerboard (CB), stripe, and star solids, respectively, with the corresponding ground state configurations being sketched in panels b–d. Analogous to the standard Mott insulating phases of Figure 25, these lattice solids at fractional filling factor exist in some low-tunneling region of the μ vs J phase diagram.

Interestingly, it was found that a supersolid phase can be stabilized in a broad range of parameters by doping the checkerboard and star Mott solids *with either vacancies*

(removing particles) or *interstitials* (adding extra particles), in accordance with Andreev–Lifshitz’s scenario of defect-induced supersolidity.²⁰⁰ For example, a vacancy SS is present for densities $0.5 > n \gtrsim 0.43$, roughly independent of the interaction strength. In contrast to, e.g., case (iii) above, the long-range interactions prevent phase separation from occurring below filling $n = 1/2$ in this microscopic model. This offers interesting prospects for the first observation of this exotic phase using polar molecules.

Both the solid/supersolid and supersolid/superfluid quantum phase transitions are second-order. By increasing T , the SS melts into a featureless normal fluid via a two-step transition, with the intermediate phase being a normal fluid with finite density modulations, similar to a liquid crystal.¹⁸³

Devil’s Staircase and Metastable Many-Body States. The large Mott lobes with $n = 1/2$, $1/3$, and $1/4$ are robust in the presence of a confining harmonic potential and moderately finite $T/J \sim 1$, and thus, they are relevant to experiments. Interestingly, for small-enough hopping $J/V \ll 0.1$, the low-energy phase is found to be incompressible ($\partial n/\partial \mu = 0$) for most values of μ . This parameter region is labeled as DS in Figure 26, and it corresponds to a finite- J version of the classical *Devil’s staircase*. First discussed in the context of atomic monolayers adsorbed on solids,²⁰¹ the latter consists of a succession of incompressible ground states, dense in the interval $0 < n < 1$, with a spatial structure commensurate with the lattice for all rational fillings.^{201,202} This behavior, which has no analogue for shorter range interactions, is shown in Figure 27a,b, where the particle density n is plotted as a function of the

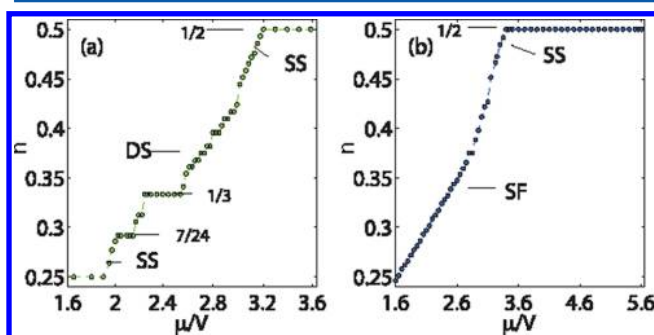


Figure 27. n vs μ : (a) Solids and SS for a system with linear size $L = 12$ and $J/V = 0.05$. Some n are indicated. (b) Superfluid and vacancy-SS for $L = 16$ and $J/V = 0.1$. (Image adapted from ref 183. Copyright 2010 American Physical Society.)

chemical potential μ . In the figure, a continuous increase of n as a function of μ signals a compressible phase, while a solid phase is characterized by a constant n . The main plateaux in panel a corresponds to the Mott lobes of Figure 26, while the other steps are incompressible phases, with a fixed, *integer*, number of particles, indicating the Devil’s-like staircase. We will come back to this point in the discussion of one-dimensional models.

Determining the exact ground state geometry and periodicity of the solid for a given set of Hamiltonian parameters in the DS region is however a computationally daunting task, since (i) for many rational fillings (e.g., $n = 7/24$ in Figure 28a) it would require consideration of system sizes much larger than those accessible with reasonable numerical resources, and (ii) the long-range interactions determine the presence of numerous low-energy *metastable* states,²⁰³ which for finite T can result in the presence of defects or in disordered structures. The stability

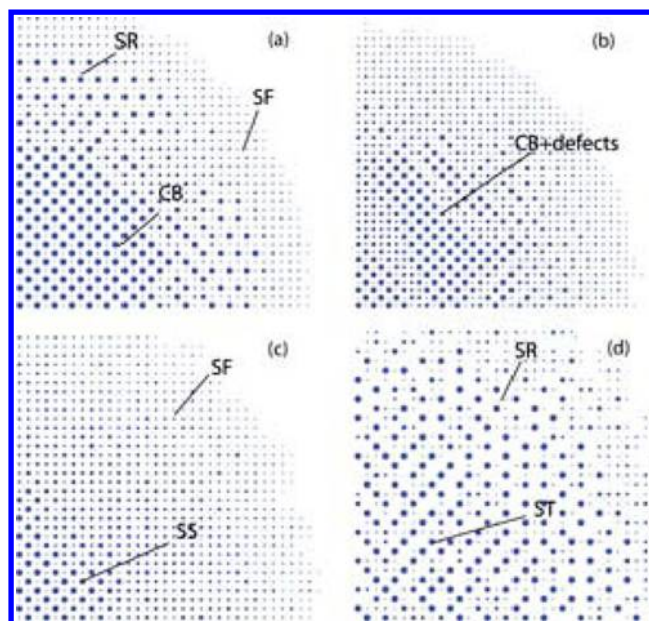


Figure 28. Spatial density profile in 2D for $N \approx 1000$ particles in a harmonic potential. Phases are indicated (CB, SR, and ST stand for checkerboard, star, and stripe solids, respectively). (a–b) $V/J = 15$, $\mu/J = 55$, $\Omega/J = 0.05$, and $T/J = 0.0377$, with temperature annealing performed in panel a; (c) $V/J = 5$, $\mu/J = 19$, $\Omega/J = 0.01$, and $T/J = 0.1$; (d) $V/J = 20$, $\mu/J = 51$, $\Omega/J = 0.04$ and $T/J = 0.25$. (Adapted from ref 183.)

of low-energy metastable states has been thoroughly studied in refs 203 and 204, where it is found that, especially in larger lattices, two metastable configurations might differ by the occupation of just a few lattice sites. Thus, because of the presence of these metastable states, in an experiment, it will be very difficult to reach the ground state or a given metastable configuration. This is directly reflected in the numerics: Figure 28 shows snapshots of the spatial density distribution in the lattice in the presence of a realistic harmonic confinement (shown is a single quadrant). Each circle corresponds to a different site, and its radius is proportional to the local density. In panels a and b, μ is chosen such that particles at the trap center are in the CB phase, with very small T . The density profile shows a wedding-cake structure, with concentric Mott-lobes with density $n = 1/2$ and $1/4$, analogous to the shells with contact interactions.^{205,206} However, while the system parameters are the same in both figures, panel a shows regular CB and star patterns, while in panel b extended defects are present in the CB phase and the star is barely visible. This is due to the different preparation of the states in panels a and b. In fact, in panel a temperature annealing of the system prior to taking the snapshot was performed in order to eliminate defects, while this was not done in panel b. Defects in panel b reflect the existence of a large number of low-energy metastable states, which are a direct consequence of the long-range nature of the interactions.

Additional Exotic Phases. Interestingly, the possibilities offered by polarized dipoles in a 2D are not exhausted by the phases above. In ref 191, the first numerical evidence has been proposed for a *bosonic* lattice version of the “microemulsion” phase¹⁶³ introduced in section 6.1, for a system of polarized hard-core dipoles on a *triangular* lattice. This is shown in Figure 29, where an emulsion phase is indicated as separating the Mott lobe at $n = 1/3$ from a low-density superfluid, suggesting a qualitative difference between the behavior of this complex

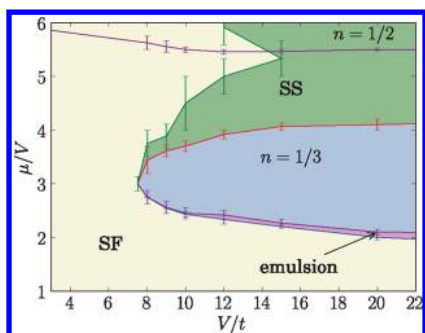


Figure 29. Ground state phase diagram for the Hamiltonian eq 89 on a triangular lattice in 2D, around $n = 1/3$. The phases are a superfluid “SF”, a supersolid “SS”, and a commensurate solid at density $n = 1/3$. A transition region of the Spivak–Kivelson bubble type (emulsions) is indicated with the double line, gradually going over to a region of incommensurate, floating solids with increasing interaction strength. For large interaction strength, and starting around half filling, the supersolid phase is suppressed by emerging solid ordering (stripes at half filling and incommensurate; floating solids at other fillings). (Adapted from ref 191. Copyright 2010 American Physical Society.)

strongly interacting system above and below the Mott lobe. In view of future experiments with ultracold atomic gases with comparatively large magnetic dipolar moments, such as Cr, Dy, and Er atoms, it is an exciting prospect to investigate how finite on-site interactions, which usually favor superfluid and supersolid behavior, will modify this picture.

Fermi Gases. A conclusive determination of the phase diagram of 2D fermionic dipoles has been so far hampered by the lack of exact theoretical tools for the study of the strongly interacting regime. The experiments with dipolar gases have motivated several theoretical works, which use different approximate, often complementary, techniques. In analogy with Coulomb systems, for dipolar gases polarized perpendicular to the 2D plane (e.g., with isotropic in-plane interactions as discussed before), the existence of both crystal-like^{207–209} and quantum liquid crystal phases^{210,211} (with interactions cutoff at NNN) has been recently discussed. In particular, using a mean-field-theory approach, ref 207 has focused on determining the complex structure of phases and phase-transitions of charge-density waves with different lattice unit cells. References 212 and 213 have discussed quantum liquid crystal phases, which may be obtained for anisotropic interactions. Analogous to the case of classical liquid crystals,²¹⁴ these phases are classified as being *nematic* and *smectic* according to their symmetry breaking associated with the deformation of the Fermi surface as compared to the isotropic case. In the nematic phase, the rotational symmetry is broken so the typical Fermi surface has a cigar-like shape; that is, it is stretched in one direction and shrunk in other directions. In the smectic phase, the system is effectively in a reduced dimension; accordingly, the Fermi surface is divided into disconnected pieces. Experiments with atomic and molecular dipoles will offer an enticing opportunity to test these predictions.

6.2.2. Polarized Dipoles on a Bilayer Optical Lattice.

As discussed in section 3, polarized dipoles trapped in a bilayer configuration can form a paired superfluid phase (PSF), which originates from the interlayer attraction due to dipole–dipole interactions, when tunneling between the two layers is suppressed. The addition of an in-plane optical lattice in the two layers makes this situation even more rich from a physical point of view: in ref 215, it was shown that the presence of

strong enough intralayer repulsion and interlayer attraction for bosonic particles allows for the realization of a novel phase, named a pair-supersolid phase (PSS), which is defined as a supersolid phase of composite particles. Using a model Hamiltonian with finite on-site intralayer interactions U and NN intralayer interactions and within a mean-field analysis, it was shown that the existence of the PSS phase relies on second order tunneling of (composite) dipoles in parameter regimes close to insulating Mott phases of (composite) dipoles, similar to the discussion of section 6.2.1. One example is given in Figure 30. The existence of this exotic phase had been

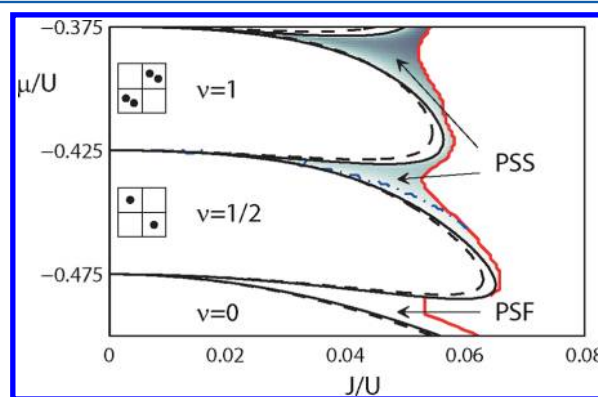


Figure 30. Phase diagram of the effective Hamiltonian of ref 215 describing bosonic dipoles trapped in a 2D two-layer configuration. The model Hamiltonian has an extended Bose–Hubbard form with $U_{ii+1}^{\sigma\sigma} = 0.025U_{ii}^{\sigma\sigma}$, $U_{ii+1}^{\sigma\sigma'} = -0.95U_{ii}^{\sigma\sigma}$. Here, σ and σ' label the two layers. The black full lines are semianalytic solutions indicating the boundaries of the insulating lobes for the checkerboard ($n = 1/2$) and the doubly occupied checkerboard ($n = 1$). The shaded area is the PSS phase predicted within a Gutzwiller mean-field approach. PSS indicates a pair-supersolid-phase, and PSF a pair-superfluid-phase see text. (Adapted from ref 215. Copyright 2009 American Physical Society.)

previously discussed for anisotropic t – J models,¹⁹² but no evidence was found. It remains an open question whether exact (e.g., QMC) calculations will confirm this prediction for realistic models with long-range interactions and, e.g., onsite hard-core constraint.

6.3. Advanced Hamiltonian Design with Polar Molecules

The quantum phases of section 6.2.1 are based on interactions of the dipole–dipole type (see eq 1) and are thus present for any dipolar gas. For polar molecules, the techniques described in section 2.2 for modifying the *shape* of interaction potentials allow for an advanced engineering of microscopic Hamiltonians. This offers new opportunities to explore exotic many-body phases in these systems. In the following we review recent progress by discussing situations where pure *three-body* effective interactions can dominate the dynamics (section 6.3.1), and the use of internal degrees of freedom for each molecule in addition to rotational ones can provide toolboxes for the simulation of condensed matter models of interest, including exotic lattice spin models (section 6.3.2).

6.3.1. Three-Body Interactions. In section 2.2, techniques were introduced for the modification of the shape of the effective interaction potentials using external dc electric and ac microwave fields coupling rotational excitations of the molecules. In particular, for a circularly polarized ac field, the attractive time-averaged interaction due to the rotating dipole moments of the molecules has been shown to allow a strong

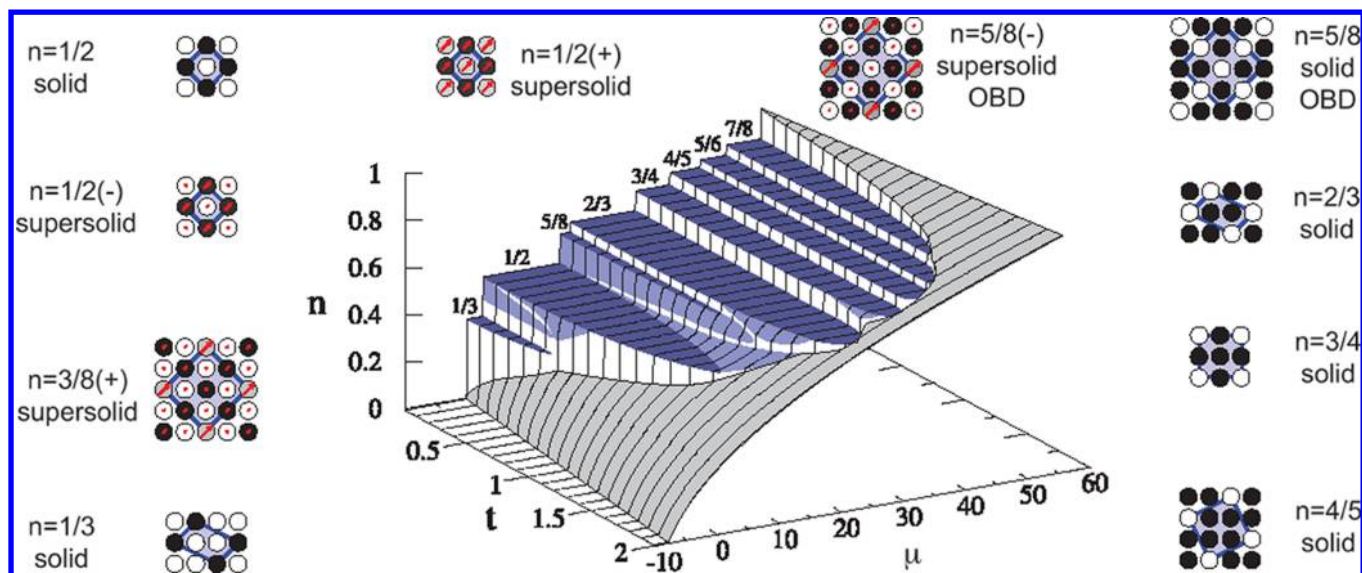


Figure 31. Central plot: phase diagram of the minimal model obtained within the semiclassical approach as a function of the chemical potential μ and the nearest-neighbor hopping amplitude J . Gray (white) regions are superfluid (phase separated), and light (dark) blue denotes supersolids (solids). Surrounding plots: schematic representation of the nature of some of the solid and supersolid phases. The gray scale of the circles represents the filling (white = empty, black = full), while the length and the direction of the red arrows denote the amplitude and the phase of the superfluid component. The blue lines highlight the unit cell of the different structures. (Adapted from ref 220. Copyright 2008 American Physical Society.)

reduction, and even a cancellation, of the total dipole–dipole interaction. In a dense ensemble of molecules, this can lead to the realization of systems where the effective *three-body* interaction $W^{3D}(\mathbf{r}_i, \mathbf{r}_j, \mathbf{r}_k)$ of eq 5 dominates over the two-body term $V^{3D}(\mathbf{r}_i - \mathbf{r}_j)$ and determines the properties of the system in the ground state. We note that, as always, direct particle–particle interaction involve two particles only, while few-body interactions emerge as an effective low-energy interaction after the high-energy degrees of freedom are traced out.

Model Hamiltonians with strong three-body and many-body interactions are strong candidates for exhibiting exotic ground state properties. This is exemplified by the fractional quantum Hall states described by Pfaffian wave functions which appear as ground states of a Hamiltonian with three-body interactions.^{216–218} These topological phases support anionic excitations with nonabelian braiding statistics. The possibility of realizing a Hamiltonian where the two-body interaction can be manipulated independently of the three-body term has been studied in ref 219. There, it is shown that a stable system of particles interacting via purely repulsive three-body potentials can be realized by combining the setup above with a tight optical confinement provided by an optical lattice. The latter ensures collisional stability of the setup and defines a characteristic length scale (the lattice spacing) where an exact cancellation of the two-body term can occur. The resulting extended Hubbard-like Hamiltonian has the form

$$H = -J \sum_{\langle ij \rangle} b_i^\dagger b_j + \sum_{i \neq j} \frac{U_{ij}}{2} n_i n_j + \sum_{i \neq j \neq k} \frac{W_{ijk}}{6} n_i n_j n_k \quad (90)$$

where $W_{ijk} n_i n_j n_k$ is an offsite three-body term. The latter is tunable independently of the two-body term $U_{ij} n_i n_j$ to the extent that it can be made to dominate the dynamics and determine the properties of the system in the ground state. This is in contrast to the common approach to derive effective many-body terms from Hubbard models involving two-body interactions, which are obtained in the $J \ll U$ perturbation limit and are thus necessarily small.²²¹

The phase diagram for bosonic particles on a 2D lattice with three-body interactions has been recently investigated in ref 220 (see Figure 31), where a rich variety of superfluid, solid, supersolid, and phase separated phases have been found. In particular, several solid phases at fractional filling factor are found to evolve upon doping into supersolid phases with complex spatial structures. For example, the checkerboard supersolid at filling factor $1/2$, which is unstable for hardcore bosons with nearest neighbor two-body interaction, is found to be again stable in a wide range of tunneling parameters, similar to the case of pure dipolar interactions discussed above.

The phase diagram for bosonic particles on a 1D lattice has been studied in ref 222, with the corresponding phases being discussed in section 7.

6.3.2. Lattice Spin Models and Quantum Magnetism.

Lattice spin models are ubiquitous in condensed matter physics, where they are used to describe the characteristic behavior of complicated interacting physical systems. Recent works have focused on realizing an effective spin Hamiltonian for the simulation of lattice spin models of fundamental interest in condensed-matter, obtained by considering several internal states of each molecule.

Reference 223 has shown that cold gases of polar molecules can be used to construct in a natural way a *complete toolbox* for any permutation symmetric two spin- $1/2$ (qubit) interaction, based on techniques of interaction engineering which are extensions of those discussed in section 2.2. The main ingredient of this (and related) proposal is the dipole–dipole interaction: it couples strongly the rotational motion of the molecules, it can be designed by means of microwave fields, and it can be made spin-dependent, exploiting the spin-rotation splitting of the molecular rotational levels.

The basic building block in ref 223 is a system of two polar molecules strongly trapped at given sites of an optical lattice, where the spin- $1/2$ (or qubit) is represented by a single unpaired electron outside a closed shell of a $^2\Sigma_{1/2}$ heteronuclear molecule in its rotational ground state, as

provided, e.g., by alkaline-earth monohalogenides. Rotational excitations are described by the Hamiltonian

$$H_m = BN^2 + \gamma \mathbf{N} \cdot \mathbf{S} \quad (91)$$

with \mathbf{N} the rotational angular momentum of the nuclei, and \mathbf{S} the dimensionless electronic spin (assumed to be $S = 1/2$ in the following). Here B denotes the rotational constant and γ is the spin-rotation coupling constant. The typical values of B are a few tens of GHz, and γ is usually in the hundred MHz regime. The interaction describing the internal degrees of freedom is $H_{in} = V_{dd} + \sum_{i=1}^2 H_{im}^i$, where H_{dd} is the dipole–dipole interaction.

The molecules are assumed to be trapped in the optical lattice with a separation $\Delta \sim zr_\gamma \equiv (2d^2/\gamma)^{1/3}$, where the dipole dipole interaction is $d^2/r_\gamma^3 = \gamma/2$ (Figure 32). In this regime the rotation of the molecules is strongly coupled to the spin and the excited states are described by Hund's case (c) states in analogy to the dipole–dipole coupled excited electronic states of two atoms with fine-structure. Thus, while the two-particle ground states are essentially spin independent, effective spin-dependent interactions in the ground states can be obtained by dynamically mixing dipole–dipole coupled excited states into the ground states using a microwave field $\mathbf{E}(\mathbf{x}, t)$ with properly chosen polarization, frequency ω_F and Rabi-frequency Ω , which is tuned near resonance with the $N = 0 \rightarrow N = 1$ transition.

The effective interactions in the lowest-energy states are obtained by diagonalizing the $H_{BO} = H_m - \sum_{i=1,2} d_i \mathbf{E}$ potential, as described in section 2.2. In second-order perturbation theory, they read

$$V_{\text{eff}}^{3D}(r) = \sum_{i,f} \sum_{\lambda(r)} \frac{\langle g_f | H_{mf} | \lambda(r) \rangle \langle \lambda(r) | H_{mf} | g_i \rangle}{\hbar\omega_F - E(\lambda(r))} |g_f\rangle \langle g_i| \quad (92)$$

where $\{|g_i\rangle, |g_f\rangle\}$ are ground states for two molecules with $N_1 = N_2 = 0$ and $\{|\lambda(r)\rangle\}$ are excited eigenstates of H_{in} with $N_1 + N_2 = 1$ and with excitation energies $\{E(\lambda(r))\}$. The reduced interaction in the subspace of the spin degrees of freedom is then obtained by tracing over the motional degrees of freedom. For molecules trapped in the ground motional states of isotropic harmonic wells with rms width z_0 , the wave function is separable in the center of mass and relative coordinates, and the effective spin–spin Hamiltonian is $H_{\text{spin}} = \langle H_{\text{eff}}(r) \rangle_{\text{rel}}$.

The effective Hamiltonian eq 92 can in general be rewritten as²²³

$$H_{\text{eff}}(r) = \frac{\hbar|\Omega|}{8} \sum_{\alpha,\beta=0}^3 \sigma_1^\alpha A_{\alpha,\beta}(r) \sigma_2^\beta \quad (93)$$

where $\{\sigma^\alpha\}_{\alpha=0}^3 \equiv \{1, \sigma^x, \sigma^y, \sigma^z\}$ and A is a real symmetric tensor. Equation 93 describes a generic permutation symmetric two qubit Hamiltonian. The components $A_{0,s}$ describe a pseudo-magnetic field which acts locally on each spin, and the components $A_{s,t}$ describe two qubit coupling.

For a given field polarization, tuning the frequency near an excited state induces a particular spin pattern on the ground states. These patterns change as the frequency is tuned through multiple resonances at a fixed intermolecular separation. For example, the anisotropic spin model $H_{XYZ} = \lambda_x \sigma^x \sigma^x + \lambda_y \sigma^y \sigma^y + \lambda_z \sigma^z \sigma^z$ can be simulated using three fields: one polarized along \hat{z} tuned to $0_u^+(3/2)$, one polarized along \hat{y} tuned to $0_g^-(3/2)$, and one polarized along \hat{x} tuned to $0_g^+(1/2)$. The strengths λ_j can be tuned by adjusting the Rabi frequencies and detunings of the three fields.

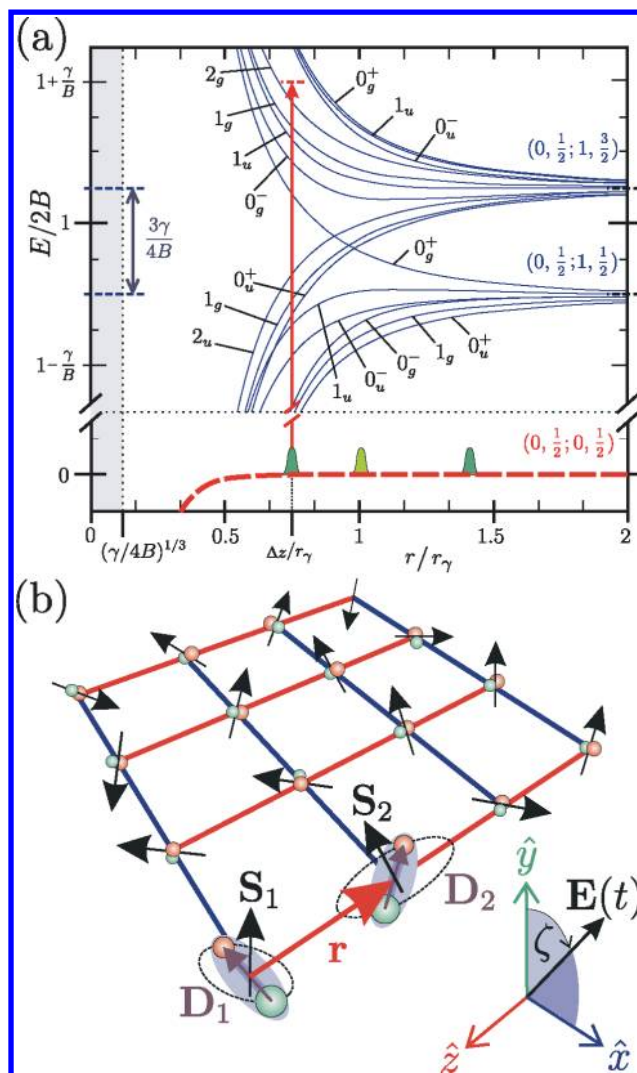


Figure 32. (a) Potentials for a pair of molecules as a function of their separation r . The symmetries $|Y_\sigma^\pm\rangle$ of the excited manifolds are indicated, as are the asymptotic manifolds $(N_i J_i; N_j J_j)$. Here the quantum numbers are the following: $Y = M_N + M_S$, where $M_N = M_{N1} + M_{N2}$ and $M_S = M_{S1} + M_{S2}$ are the total rotational and spin projections along the intermolecular axis; parity eigenvalues $\sigma = \pm 1$ are denoted as g (u) for gerade (ungerade); reflection symmetry $R = \pm$ of all electronic and rotational coordinates through a plane containing the intermolecular axis. (b) Example anisotropic spin models that can be simulated with polar molecules trapped in optical lattices: Square lattice in 2D with nearest neighbor orientation dependent Ising interactions along \hat{x} and \hat{z} . Effective interactions between the spins \mathbf{S}_1 and \mathbf{S}_2 of the molecules in their rovibrational ground states are generated with a microwave field $\mathbf{E}(t)$ inducing dipole–dipole interactions between the molecules with dipole moments \mathbf{d}_1 and \mathbf{d}_2 , respectively. (Adapted from ref 223.)

Of particular interest is the possibility of realizing highly anisotropic spin models such as the following one

$$H_{\text{spin}}^{(l)} = \sum_{i=1}^{l-1} \sum_{j=1}^{l-1} J(\sigma_{i,j}^z \sigma_{i,j+1}^z + \cos \zeta \sigma_{i,j}^x \sigma_{i+1,j}^x) \quad (94)$$

which was first introduced by Douçot et al.²²⁴ in the context of Josephson junction arrays. This model (for $\zeta \neq \pm\pi/2$) admits a 2-fold degenerate ground subspace that is immune to local noise up to l -th order and, hence, is a good candidate for

storing a topologically protected qubit for applications in quantum computing. Other Hamiltonians that can be realized include the famous Kitaev model.

References 225–227 have recently focused on the realization of tunable Heisenberg-type models for unit filling of the optical lattice. Effective spin degrees of freedom are encoded in internal, e.g. rotational, states of the molecules, and molecular interactions are tuned by a combination of dc and ac fields, using techniques similar to those of section 2.2. In refs 226 and 227 it is found that doping the lattice with vacancies (that is, removing particles from a few sites) leads to a tunable generalization of the so-called t - J model, which is relevant in the context of high-temperature superconductivity.²²⁸ Typical Hamiltonian terms which are found in addition to eq 87 are of the form

$$H_1 = \frac{1}{2} \sum_{i \neq j} [J_z S_i^z S_j^z + \frac{J_{\perp}}{2} (S_i^+ S_j^- + S_i^- S_j^+) + V n_i n_j + W n_i S_j^z] / (\mathbf{r}_i - \mathbf{r}_j)^3 \quad (95)$$

where the operators $S_j^z = (n_{j\sigma} - n_{j\sigma'})/2$, $S_j^+ = c_{j\sigma}^\dagger c_{j\sigma'}$, and $S_j^- = (S_j^+)^\dagger$ are spin- $1/2$ angular momentum operators on site j describing a two-level dressed rotor degree of freedom σ (e.g., the lowest two $N_z = 0$ states of the molecule in the presence of a dc electric field along \hat{z}) and satisfying $[S_j^z, S_j^\pm] = \pm S_j^\pm$. By intuitively thinking of the ground state as a (classical) dipole $\mu_0 = \mu_0 \hat{z}$ oriented along the dc field (i.e., $\mu_0 > 0$) and of the excited state as a dipole $\mu_1 = \mu_1 \hat{z}$ oriented against the dc electric field (i.e., $\mu_1 < 0$), the terms $J_z = (\mu_0 - \mu_1)^2$, $V = (\mu_0 + \mu_1)^2/4$, and $W = (\mu_0^2 - \mu_1^2)/2$ derive from rewriting the direct dipole–dipole interaction, while the term $J_{\perp} = 2 \mu_{01}^2$ comes from the transition dipole moment μ_{01} , describing the exchange of a microwave excitation between the molecules. One difference with the derivation of the effective spin models of ref 223 described above is that the dipole–dipole interactions in eq 95 are used in first order, rather than second order, which can allow for stronger interactions.

We note that the design of extended Hamiltonians with terms as in eq 95 is in fact a hot topic of research in atomic and molecular systems: for example, refs 229 and 230 have discussed the derivation of similar terms for trapped neutral atoms and molecules at unit filling, while refs 231 and 232 have focused on ionic particles. The $J_z = 0$ case is also studied in the context of molecules in ref 233. In ref 234, a similar Hamiltonian describes the dynamics of exciton-like interactions with impurities in gases of polar molecules. There, the authors considered first a clean system with one particle per site, subject to a very deep optical lattice potential in order to prevent particle tunneling: in this regime, dipole–dipole interactions induce collective excitonic modes, in sharp contrast with individual rotational excitations of short-range interacting atoms. After substituting a small number of initial components with a different kind of molecule still strongly confined by the optical potential, the system displays an exciton–impurity interaction between the original excitonic modes and the new particles, which may be treated as effective impurities, leading to a disordered background potential with both diagonal and off-diagonal contributions. Such a setup represents an ideal platform to investigate the effect of disorder and interaction induced localization in excitonic gases in 1, 2, and 3D.

Reference 235 has considered an ensemble of $^2\Sigma$ molecules in the rotationally ground state trapped on an optical lattice and

has shown that collective spin excitations can be controlled using external electric and magnetic fields, in the context of the formation of Frenkel excitons.^{236,237} This system may be used for the quantum simulation of spin excitation transfer in many-body crystals without phonons. In ref 238 a similar Hamiltonian has been studied in the context of molecular self-assembled crystals for quantum memory applications.

The inclusion of more internal states for the particles, such as hyperfine levels, offers extensions to spin systems with larger spin.^{225–227,239} For example, the design of a large class of spin-1 interactions for polar molecules has been shown in ref 239, which allows, e.g., for the realization of a generalized Haldane model in 1D, using a strategy of interaction-engineering similar to those described above. Recent work in ref 225 has started exploring the nonequilibrium dynamics of molecules trapped in optical lattices in the presence of several internal states, including, e.g., the rich hyperfine structure often present in the ground state rotational manifolds. In particular, it was shown that the number of effective degrees of freedom participating to the dynamics may be indeed dynamically changed for each molecule using external electric and magnetic fields, similar to the discussion above. This raises interesting prospects for the study of nonequilibrium dynamics in these complex systems. In section 7, we discuss some of the intriguing scenarios opened up in the many-body context by the accurate fine-tuning of interactions presented here, for the particular case of polar molecules trapped in 1D.

6.3.3. Hubbard Models in Self-Assembled Dipolar Lattices. In Hubbard models with cold atoms or molecules in optical lattices, there are no phonon degrees of freedom corresponding to an intrinsic dynamics of the lattice, since the back action on the optical potentials is typically negligible. Thus, the simulation of polaronic materials²⁴⁰ where the presence of crystal phonons affects strongly the Hubbard-like dynamics of particles remains largely a challenge. References 241 and 242 have shown that a self-assembled floating lattice of molecules as discussed in section 6.1 can provide a periodic trapping potential for extra atoms or molecules, whose dynamics can be described in terms of a Hubbard model with phonons, the latter corresponding to vibrations of the dipolar lattice.

The Hamiltonian for extra atoms or molecules in a self-assembled dipolar lattice is

$$H = -J \sum_{\langle i,j \rangle} c_i^\dagger c_j + \frac{1}{2} \sum_{i,j} V_{ij} c_i^\dagger c_j^\dagger c_j c_i + \sum_q \hbar \omega_q a_q^\dagger a_q + \sum_{q,j} M_q e^{iq \cdot R_j^0} c_j^\dagger c_j (a_q + a_{-q}^\dagger) \quad (96)$$

Here, the first and second terms define a Hubbard-like Hamiltonian for the extra-particles of the form of eq 87, where the operators c_i (c_i^\dagger) are destruction (creation) operators of the extra-particles. However, the third and fourth terms describe the acoustic phonons of the crystal [a_q destroys a phonon of quansimomentum \mathbf{q} in the mode λ] and the coupling of the extra-particles to the crystal phonons, respectively. Tracing over these phonon degrees of freedom in a strong coupling limit provides effective Hubbard models for the extra-particles dressed by the crystal phonons

$$\tilde{H} = -\tilde{J} \sum_{\langle i,j \rangle} \tilde{c}_i^\dagger \tilde{c}_j + \frac{1}{2} \sum_{i,j} \tilde{V}_{ij} \tilde{c}_i^\dagger \tilde{c}_j^\dagger \tilde{c}_j \tilde{c}_i \quad (97)$$

The hopping of a dressed extra-particle between the minima of the periodic potential occurs at a rate \tilde{J} , which is exponentially suppressed due to the copropagation of the lattice distortion, while onsite particle–particle interactions \tilde{V}_{ij} are now a combination of direct particle–particle interactions and interactions mediated by the coupling to phonons, as given by polaronic dynamics.²⁴³ Figure 33 shows two implementa-

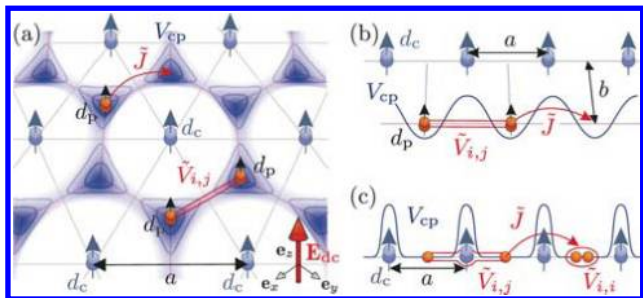


Figure 33. Floating lattices of dipoles: A self-assembled crystal of polar molecules with dipole moment d_c provides a 2D periodic honeycomb lattice V_{cp} (darker shading corresponds to deeper potentials) for extra molecules with dipole $d_p \ll d_c$ giving rise to a lattice model with hopping \tilde{J} and long-range interactions \tilde{V}_{ij} .

tions of this idea in two- and quasi-one-dimensional configurations (panels a and b–c, respectively). The distinguishing features of this realization of lattice models are the tunability of interactions among crystal dipoles and of the particle–phonon couplings. In addition, the lattice spacings are tunable with external control fields, ranging from a micrometer down to the hundred nanometer regime, i.e. potentially smaller than for optical lattices. Compared with optical lattices, for example, a small scale lattice yields significantly enhanced hopping amplitudes, which set the relevant energy scale for the Hubbard model, and thus also the temperature requirements for realizing strongly correlated quantum phases. Phonon-mediated interactions can be quite long-ranged, decaying with distance as $1/r^2$ in 1D.

7. DIPOLAR GASES IN ONE- AND QUASI-ONE-DIMENSIONAL GEOMETRIES

In reduced dimensionality, the effects of quantum fluctuations are so relevant that the standard Fermi-liquid picture breaks down due to the emergence of several strongly correlated states of matter. The addition of interaction with a long-range, anisotropic tail such as the dipolar one leads to the stabilization of a very rich phase diagrams in both purely 1D systems and coupled ones such as ladders and planar arrays. In the following, we will first review the basic physics of the single tube configuration and then illustrate recent results on two-leg and multileg ladders.

7.1. Dipolar Gases in a Single Tube

We now consider a system of dipolar particles confined in a one-dimensional (1D) geometry by a sufficiently deep optical lattice with frequency ω_{\perp} , so that their dynamics is purely 1D. In order to ensure collisional stability, we will consider all dipole moments aligned perpendicularly to the wire direction by an external field in such a way that the interparticle interaction is always repulsive. Defining m the mass of the particles and C_3 the strength of the dipolar interaction, a proper description for, e.g., a gas of polar molecules in the long-

distance regime (see section 2) is encoded in the following model Hamiltonian:

$$H = \int dx \psi^{\dagger}(x) \left[-\frac{\hbar^2}{2m} \partial_x^2 \right] \psi(x) + \frac{1}{8\pi} \int dx dx' \psi^{\dagger}(x) \psi^{\dagger}(x') \frac{C_3}{|x-x'|^3} \psi(x') \psi(x) \quad (98)$$

where $\psi(x)$, $\psi^{\dagger}(x)$ are annihilation/creation operators with bosonic or fermionic statistics. For a polar molecule gas, $C_3 = d^2/\epsilon_0$, where ϵ_0 is the vacuum permeability and d the dipole moment induced by a dc electric field. After a proper rescaling of all quantities, the only relevant parameters are the ratio between the dipolar length $R_3^{-1} = 2\pi\hbar^2/(mC_3)$ and the linear density ρ_0 and, as such, we expect all thermodynamic properties to depend only on $\rho_0 R_3$. While statistical properties are expected not to play a major role in this setup since bosons are subject to an effective hard-core condition due to the infinite short-distance repulsion, some properties of the system are still affected by statistics; thus, we will at first consider a bosonic gas and then comment on the fermionic case at the end of the section. Qualitative features of eq 98 are obtained using the bosonization technique, which allows mapping the original interacting problem into a free one via the following identities:^{244–247}

$$\psi_{B/F}^{\dagger}(x) \simeq \sqrt{\rho_0 + \frac{\partial_x \vartheta(x)}{\pi}} e^{i\varphi(x)} \times \sum_m^{\text{odd/even}} \exp[im(\vartheta(x) + \pi\rho_0 x)] \quad (99)$$

$$n(x) = \left(\rho_0 + \frac{\partial_x \vartheta(x)}{\pi} \right) \times \left[\sum_{m=-\infty}^{\infty} \exp[i2m(\vartheta(x) + \pi\rho_0 x)] \right] \quad (100)$$

Here, the field φ and ϑ represent density and phase fluctuations of the original field, and satisfy bosonic commutation relations $[\partial_x \vartheta(x), \varphi(y)] = i\pi\delta(x-y)$. As long as the long-range tail of the interaction potential decays faster than Coulomb-like interactions,^{248,249} $1/|x-x'|$, as in the dipolar case, the Hamiltonian in eq 98 is mapped into the so-called Tomonaga–Luttinger liquid (TLL):²⁴⁴

$$H = \frac{\hbar v}{2\pi} \int dx [(\partial_x \vartheta(x))^2/K + K(\partial_x \varphi(x))^2] \quad (101)$$

which is a purely quadratic Hamiltonian with a linear dispersion relation at small momenta, $\omega(k) \simeq vk$; the excitations in the system are sound waves of the density with correspondent sound velocity v , whereas the factor K , known as the Tomonaga–Luttinger liquid parameter, is related to the compressibility of the system C via $K = v\pi C$, and in Galilean invariant systems satisfies $K = v_F/v$, $v_F = \hbar\rho_0\pi/m$. The TLL picture (Figure 34) captures the entire low-energy physics of the original model and represents the substitute of the Landau–Fermi liquid scenario in 1D; analogously, the parameters v, K play a similar role to the Landau parameters in higher dimensions. In addition, the long-distance decay of correlation functions is completely captured by K , so that after the bosonization mapping one gets

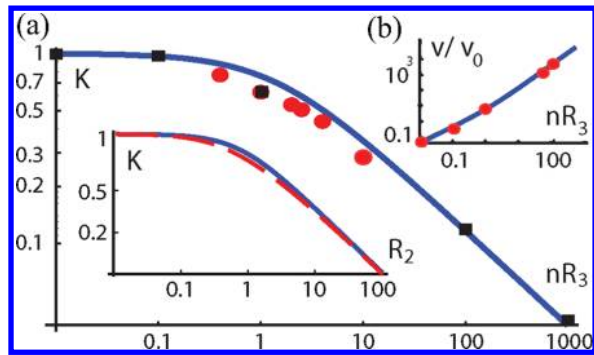


Figure 34. Panel a: TLL parameter K in a dipolar wire as a function of the dimensionless interaction strength $\rho_0 R_3$ (here, $\rho_0 \equiv n$). The blue line is eq 107, while red points and black squares are QMC results from refs 257 and 254, respectively. The inset shows a similar prediction with inverse-square interaction (blue line) compared with the exact result (red dashed line). Panel b: sound velocity to Fermi velocity ratio v/v_F ($v_0 \equiv v_F$) as a function of $\rho_0 R_3$; the blue line and red points are analytical and QMC results from refs 258 and 254, respectively. Image taken from ref 258.

$$B(x) = \langle \psi^\dagger(x) \psi(y) \rangle \simeq \frac{1}{|x - y|^{1/2K}} \quad (102)$$

for the one-body density matrix, also known as the *superfluid* (SF) correlation, and

$$D(x) = \langle n(x) n(y) \rangle - \rho_0^2 \simeq \frac{1}{|x - y|^2} + \frac{\cos(2\pi(x - y)\rho_0)}{|x - y|^{2K}} \quad (103)$$

for the correlated part of the density–density, or *charge–density–wave* (CDW), correlation function. The possibility of qualitatively describing the asymptotic decay of correlations is remarkable. Since spontaneous symmetry breaking is not allowed in many 1D models because of the Mermin–Wagner–Hohenberg theorem,^{250,251} correlation functions encode the necessary information to distinguish between different phases in low dimensional geometries; the slowest decaying correlation is usually referred to as *dominant order*, corresponding to the more diverging susceptibility in the system.^{246,245} From eqs 102 and 103, we thus expect a transition from dominant SF correlations to CDW ones at a precise value of the TLL parameter, $K = 1/2$, where the two decay exponents coincide.

While, in principle, all information regarding the quantum phases in 1D is encoded in the LL parameters, the bosonization techniques sketched above do not allow, in general, establishment of a relation between the microscopic quantities in eq 98 and K , as the latter has to be regarded as a phenomenological parameter to be determined by comparisons with experiments or numerical results. Before discussing the general case, let us comment on some relevant situations. In the weakly interacting limit, $\rho_0 R_3 \ll 1$, the dipolar interaction is relevant only at very short distances, and thus, the system behaves very similarly to a Tonks–Girardeau gas,^{252,253} for which $K_{TG} = 1$; as such, we expect $K^{(wc)} \simeq 1$ in the weakly interacting regime. In the strongly interacting case, $\rho_0 R_3 \gg 1$, it has been noticed in refs 254 and 255 that, approximating the system as a classical crystal where particles are quasi-localized at equally spaced distances, one has an energy per particle $e_0 = \zeta(3)[\rho_0 R_3/(2m)]$ (where ζ is the Riemann ζ function), and deriving from it the

compressibility C , the resulting TLL parameter in the strong coupling regime reads as follows:

$$K(\rho_0 R_3 \gg 1) = (0.73 \rho_0 R_3)^{-1/2} \quad (104)$$

Away from these two limits, the mapping of K into the microscopic parameters of eq 98 has to be performed using nonperturbative techniques. Numerical QMC simulations based on reptation, diffusion, and Worm algorithm have been performed,^{254,256,257} allowing estimation of the TLL parameter from the so-called static structure factor

$$S(k) = \int_0^L dx e^{-ikx} \langle n(x) n(0) \rangle \quad (105)$$

and from the long-distance decay of $B(x)$ (see Figure 34). Moreover, QMC also allows quantitative estimation of the momentum distribution

$$n(k) = \frac{1}{L} \int_0^L dx B(x) e^{ikx} \quad (106)$$

which is directly measurable in experiments and, according to TLL theory, displays a clear signature of the SF/CDW transition, as the typical peak of quasi-condensation at $k = 0$ disappears just across from the phase boundary between the SF and CDW phases. Typical QMC results for $n(k)$ are shown in Figure 35 just across the phase boundary, as can be argued from

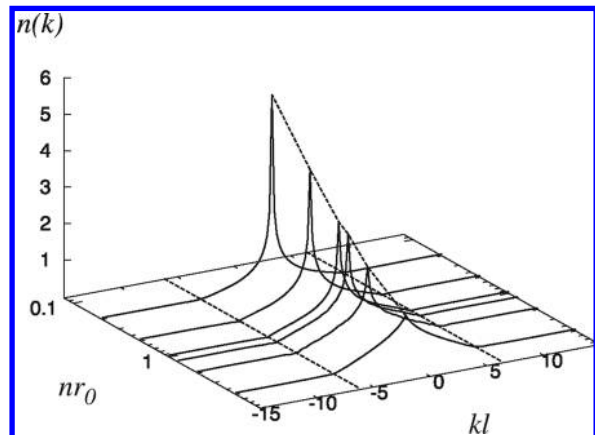


Figure 35. Momentum distribution as a function of the interaction strength in a single tube as obtained from QMC simulation;²⁵⁷ the quasi-condensation peak at $k = 0$ smoothens out with increasing repulsion according to TLL theory. Here, $n = \rho_0$, $r_0 = R_3$ fix the notations, and l is the system size. Image taken from ref 257. Copyright 2010 IOP Publishing.

the sharp decrease of $n(0)$ when the interaction is increased. Moreover, analytical results obtained through approximate methods lead to the following expression:²⁵⁸

$$K = \left(1 + \frac{6\zeta(3)}{\pi^2} \rho_0 R_3 \right)^{-1/2} \quad (107)$$

which compares favorably with numerical simulations, as can be seen in Figure 34, and recovers the limit in eq 104 at strong coupling.

Let us briefly discuss the relationship between a dipolar interacting gas and a bosonic one with a contact repulsive interaction, the Lieb–Liniger model.²⁵⁹ Besides sharing the same low-energy universality class (TLL), which allows a description of the thermodynamical properties of both systems

on the same footing, there are quantitative and qualitative differences between the two cases. The former is related to the very different domain spanned by the TLL parameter, that is, $0 < K < 1$ for dipoles but $K \geq 1$ for contact interactions. In addition to the momentum distribution, such a feature can, in principle, be detected by investigating the so-called breathing mode, which, as shown in ref 260 displays a remarkably different behavior. Qualitative differences are not only captured by the fact that nonlocal interactions allow crossing the SF-CDW transition; another very important feature is the response to a periodic potential, which changes qualitatively when considering nonlocal repulsion, as we will see in the next section. As a final remark, we resume the main differences between bosonic and fermionic dipolar wires: while the TLL picture remains quantitatively the same between the two, single particle correlation functions are slightly different from eq 102, and since no superfluid instability may occur, the dominant correlation in the fermionic case is always a CDW.

7.1.1. Bosonic and Fermionic Gases in an Shallow Optical Lattice. The effects of dipolar interactions become even more relevant in the presence of external perturbations such as an underlying periodic potential, as realized, e.g., by an optical lattice along the direction of the tube.³ In this configuration, long-range interactions compete with both kinetic energy and the periodic lattice potential, which in 1D has the following form:²⁶¹

$$H_{OL} = U \int dx \psi^\dagger(x) \sin^2(2\pi x/\lambda) \psi(x) \quad (108)$$

where λ is the laser wavelength, $U_L = U/E_R$ the dimensionless depth of the lattice potential, and $E_R = \hbar^2/(2m\lambda^2)$ the recoil energy. In the limit of a very shallow lattice, $U_L \ll 1$, the periodic potential may be considered as a perturbation on the TLL Hamiltonian, eq 101, and its effects may be investigated using a sine–Gordon description.^{246,258,261} The phase diagram, and thus the influence of the underlying potential, sharply depends on the ratio between the mean interparticle distance $1/\rho_0$ and the lattice spacing $\lambda/2$; when such a ratio is an integer, $2/(\lambda\rho_0) = p \in \mathbb{N}$, and for large enough interactions, the system undergoes a Berezinskii–Kosterlitz–Thouless (BKT) transition^{116,117} from a gapless (e.g., SF or CDW) to a crystalline phase, characterized by a gap in the excitation spectrum and broken translational symmetry with one particle pinned every p lattice sites. On the contrary, if $2/(\lambda\rho_0) \notin \mathbb{N}$, the system is always gapless regardless of the dipolar interaction strength. This remarkable behavior suggests the following argument: when there is an allowed configuration where particles can, at the same time, sit on the minima of the underlying potential and maintain a constant interparticle distance, the dipolar interactions and the lattice potential can pin the gas, as both lattice and dipolar potential energy contributions may be minimized by the crystalline configuration. In the opposite case, the frustration between the long-range repulsion, which tries to keep interparticle distance constant, and the periodic potential does not allow for any stabilization of crystalline structure.

The sine–Gordon model, combined with eq 107, allows quantitative predictions on the BKT transition in the regime of a shallow lattice potential where lattice bands are formed (which usually corresponds to $U/E_R \lesssim 2$).²⁴⁶ Typical phase diagrams for bosonic gases are plotted in Figure 36; the fermionic case is obtained by substituting the superfluid phase with a CDW. A Luttinger staircase, that is, a series of insulating

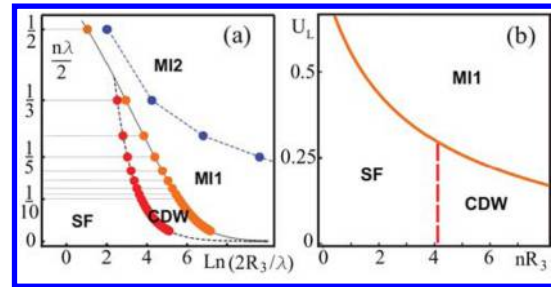


Figure 36. Panel a: commensurate phase diagram for bosons with dipolar interactions in a shallow lattice with depth $U_L = 0.1$. Physical configurations correspond to commensurate fillings $\rho_0\lambda/2 \equiv 1/p$, with $p \in \mathbb{N}$ (horizontal lines are guides to the eye for $p \leq 10$). Quantum phase transitions from a TLL to an insulating Mott insulator (MI) occur for each $1/p$ at the position of the dots on the continuous line, while red and blue dots on dashed lines indicate crossovers. MI1 and MI2 indicate MI with different low-energy spectra (see ref 258 for further details). Panel b: phase diagram at commensurate filling $1/p = 1/3$ in the U_L vs ρR_3 plane. Continuous line: quantum phase transition between a TLL and a MI. The phase diagram for fermions is identical to the one for bosons, except the TLL is always a CDW. In both panels, $n \equiv \rho_0$; image taken from ref 258. Copyright 2010 American Physical Society.

states with commensurate density satisfying $2/(\lambda\rho_0) = p \in \mathbb{N}$, appears as a function of the interaction strength at a fixed U_L .²⁵⁸

7.1.2. Bosonic Gases in a Deep Optical Lattice: Extended Bose–Hubbard Models. As discussed in the previous section, when all energy scales involved in the system dynamics are much smaller than the lattice bandwidth, both bosonic and fermionic gases are properly described in the context of Hubbard-like models. In the bosonic, single species case, the resulting extended Bose Hubbard Hamiltonian (EBHH)

$$H_{db} = -J \sum_{i=1}^L (b_i^\dagger b_{i+1} + h. c.) + V \sum_{i < j} \frac{n_i n_j}{|i - j|^3} + \sum_i \left[\frac{U}{2} n_i (n_i - 1) + \mu n_i \right] \quad (109)$$

contains kinetic energy (J), local (U), and dipolar (V) interaction terms. The corresponding phase diagram has been studied in the grand-canonical ensemble in ref 262, where a Devil’s staircase structure has been shown to appear in both the hard-core (e.g., infinitely large U) and soft-core (e.g., finite U) limits. Moreover, close to rational fillings, supersolid behavior has been suggested via both numerical and analytical methods, in particular close to the half-filled case, for both nearest-neighbor^{263,264} and dipolar interactions,²⁶⁵ whereas low and incommensurate filling fraction are still described by TLLs with both CDW and SF dominant orders.²⁶⁶

Hidden Order. In the special case of unit filling, that is, when the number of particles is equal to the number of lattice sites, an additional instability may occur. When dipolar and local interactions are much larger than the hopping rate $J \ll U, V$, the competition between U and V gives rise to two different states of matter: a Mott insulator phase when $U \gtrsim 2V$, where double occupancies are suppressed, and a density wave (DW) when $2VU \gtrsim U$, where particles rearrange in a periodic structure in order to minimize the nonlocal repulsion (see Figure 37). While these phases are separated by a first order phase transition line at strong coupling, in the intermediate

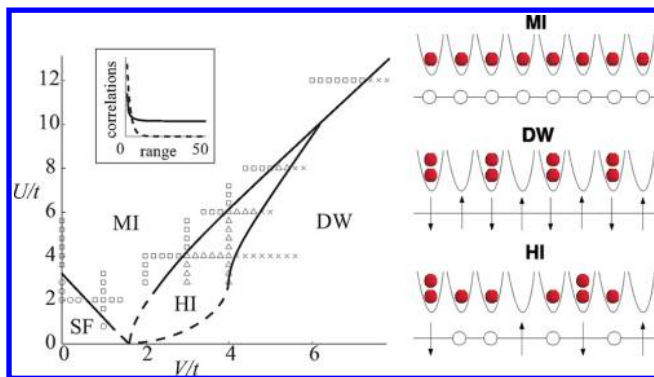


Figure 37. Left panel (Image taken from ref 267. Copyright 2006 American Physical Society.): numerical phase diagram of dipolar bosons at unit filling: the Haldane insulator is stable close to the $U \approx 2V$ line up to relatively strong magnitude of U . Inset: string (solid line) and density wave (dashed line) correlation functions in the HI phase as a function of $i - j$. Right panels: cartoons of the magnetic phases at filling one, in both bosonic and spin-1 representations.

interaction regime, it has been shown that an additional state of matter, the so-called *Haldane insulator* (HI), can emerge between the two.²⁶⁷ The HI is gapped and characterized in real space by a nonregular density pattern, where doubly occupied and empty sites are spatially separated by strings of singly occupied sites of uneven length (see the corresponding cartoon in Figure 37). The occurrence of such magnetic-like order (between two doubly occupied sites there is always one and only one empty site) together with positional disorder (the length of the strings is not constant) is encoded into a *string order parameter*:

$$O_{\text{string}}(j - k) = \langle \delta n_j \exp[i\pi \sum_{j < l < k} \delta n_l] \delta n_k \rangle \quad (110)$$

which approaches a constant value at large distances, $|i - j| \gg 1$; here $\delta n_j \equiv n_j - 1$. In addition, the density wave order parameter, $O_{\text{DW}}(j - k) = \langle \delta n_j \delta n_k \rangle$, which is constant in the DW phase, decays exponentially in the HI. Numerical simulations based on the density-matrix-renormalization-group (DMRG)^{268,269} algorithm have quantitatively determined how this phase persists up to relatively large values of the interaction strength $U \approx 8$ close to the $U \approx 2V$ line.²⁶⁷ In such a regime, where local occupations with $n_j \geq 3$ are strongly suppressed, the bosonic Hamiltonian can be mapped into a spin-1 problem where the spin component along the z -direction satisfies $S_j^z = 1 - n_j$, and the J -, V -, and U -terms play the role of spin-exchange, dipolar interaction along the z -axis, and on-site anisotropy (Figure 37). The system thus resembles the so-called Heisenberg model with single ion-anisotropy, or $\lambda - D$ model, the only qualitative difference being the presence of a full dipolar tail instead of nearest-neighbor interaction, establishing a strong connection between the HI and the Haldane phase extensively studied in the context of magnetic systems.^{270,271} An exact correspondence between the bosonic and spin problem can be obtained in the case of strong three-body losses,²⁷² where the on-site Hilbert space is truncated up to doubly occupied states and the HI phase appears at smaller values of the dipolar interaction.²⁷³ The existence of such HI has been established even at higher integer fillings by mapping the problem to integer spin chains with spin $s > 1$.²⁷⁴

Three-Body Interactions. Additional interesting states of matter can be found in the 1D version of Hamiltonians already

treated in 2D in the previous section. As an example, it has been shown how to engineer three-body interactions with polar molecules, leading to the effective Hamiltonian in eq 90. In 1D, the three-body term is responsible for the stabilization of an insulating phase at filling $2/3$, which is driven by the fact that, above a certain ratio of W/J , particles will minimize their potential energy by sitting in a periodic pattern at the expenses of the kinetic one. Such a phase transition belongs to the same universality class of the pinning one described in the shallow lattice case, and the critical value of the TLL parameter $K_c = 2/9$ at the tip of the lobe is obtained from general considerations.²²² The addition of a weak nearest neighbor repulsion $V/J \approx 1$ can also stabilize an insulating state at filling $1/2$ when $W/J \gg 1$; remarkably, the further addition of a next-nearest neighbor repulsion induces a competition between density wave and bond order wave, as the BOW phase broadens thanks to the three-body repulsion with respect to the $W = 0$ case.²⁷⁵

7.2. Two-Species Mixtures

The high degree of control over internal states of ultracold dipolar gases²⁷⁶ has opened the way toward the theoretical investigation of multispecies Hubbard-like models with additional dipolar interactions. While such specific models were not considered in standard condensed matter literature, Hamiltonians with nearest-neighbor interactions (which are, in many respects, similar to a dipolar one close to half-filling) such as the *extended Hubbard model*²⁴⁵ have been shown to present a richer plethora of phases with respect to systems with contact interactions only. The theoretical advantage of multispecies 1D systems with long-range interactions stems from the fact that one can understand their basic physical properties employing the same low-energy formalism used for models with contact interactions only.^{245,246} In the following, we will present an overview of theoretical results on two-species models with dipolar interactions, with both Fermi and Fermi–Bose statistics.

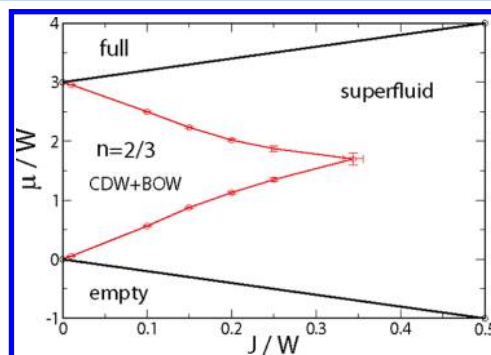


Figure 38. Phase diagram of hard-core bosons with three-body interactions in the grand canonical ensemble. In the insulating phase at $J/W \lesssim 0.3$, CDW and bond order coexist. Image taken from ref 222. Copyright 2009 American Physical Society.

7.2.1. Fermi–Fermi Mixtures. Contrary to their two-dimensional counterparts, fermionic dipolar mixtures in 1D may be theoretically investigated with the same accuracy as bosonic ones. Defining as $c_{i,\sigma}^\dagger$, $c_{i,\sigma}$ the creation/annihilation operators at the site i of the species σ (we take here $\sigma = \uparrow, \downarrow$), Fermi–Fermi mixtures in a deep optical lattice are usually described by the following Hamiltonian:

$$H_{FF} = -t \sum_{i,\sigma} (c_{i,\sigma}^\dagger c_{i+1,\sigma} + h. c.) + U \sum_i n_{i,\uparrow} n_{i,\downarrow} - \sum_{i,\sigma} \mu_\sigma n_{i,\sigma} + \frac{1}{2} \sum_{i \neq j, \sigma, \delta} \frac{V_{\sigma\delta}}{|i-j|^3} n_{i,\sigma} n_{j,\delta} \quad (111)$$

where the first two terms are hopping and on-site interaction, the third one is a species-dependent chemical potential, and the last one represents the dipolar contribution. When dealing with strong onsite two-body losses, the effective Hamiltonian has to be projected onto a constrained Hilbert space without double occupancies:

$$H^{(eff)} = \mathcal{P} H_{FF} \mathcal{P} \quad (112)$$

where $\mathcal{P} = \prod_i (1 - n_{i,\uparrow} n_{i,\downarrow})$. Such a picture, which reduces the on-site Hilbert space to just three states, is connected with the spin-1 chains (once $S_i^z = c_{i,\downarrow}^\dagger c_{i,\downarrow} - c_{i,\uparrow}^\dagger c_{i,\uparrow}$ is defined) already discussed in the context of the Haldane insulator phase for single species dipolar bosons; however, differently with respect to spin models, the key conserved quantity is $\sum_i (S_i^z)^2$, as can be inferred by performing a rigorous spin mapping.²⁷⁷ The phase diagram of eq 112 has been investigated at the mean field level and via numerical simulations based on the infinite time-evolving block decimation (iTEBD)²⁷⁸ algorithm in ref 277 considering equal chemical potentials and intraspecies interactions, $\mu_\uparrow = \mu_\downarrow, V_{\uparrow\uparrow} = V_{\downarrow\downarrow} = V$, and varying the interspecies one $V_{\uparrow\downarrow} = -V \cos(\chi)$. This setup can be realized by, e.g., applying a pair of ac microwave fields close to the resonance of both internal states.²⁷⁷ In the repulsive case, $V > 0$, the ground state is expected to show a dilute antiferromagnetic order of the form $\dots \uparrow 000 \downarrow 00 \uparrow \downarrow 00 \uparrow \dots$, where, between molecules of the same species, there is always one and only one molecule of the other species, in addition to two strings of empty sites. Such configurations display long-range order in the string correlation function

$$O_{string}^z(|k-j|) = -\langle S_k^z \exp[i\pi \sum_{k<l<j} S_l^z] S_j^z \rangle \quad (113)$$

and can be distinguished into two different cases: when $V \cos(\chi) > t - \mu/2$, all sites are occupied, and the ground state is an antiferromagnetic insulator (AFM); otherwise, the string order is dilute, the ground state is compressible, and the so-called Haldane liquid (HL) phase is stabilized. The mean field phase diagram presenting such competition is shown in Figure 39 and has been supported by numerical iTEBD results, which show how, while both the AFM and the HL have long-range

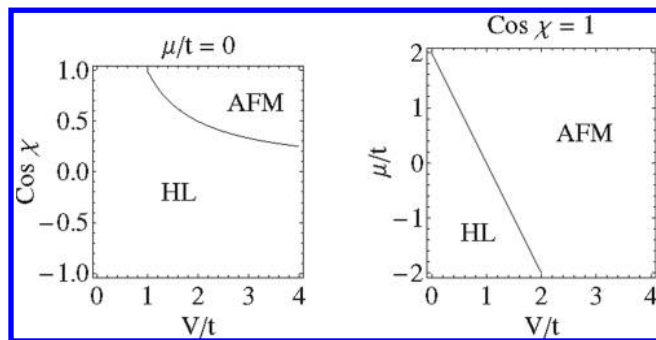


Figure 39. Mean field phase diagram for eq 112 with $\mu_\uparrow = \mu_\downarrow$ and $V_{\uparrow\uparrow} = V_{\downarrow\downarrow} = V = -V_{\uparrow\downarrow}/\cos(\chi)$. Image taken from ref 277. Copyright 2011 American Physical Society.

order in O_{string}^z other quantities such as standard spin-spin correlation functions have remarkably different behaviors,²⁷⁷ and in the HL phase may be qualitatively described by mapping the low-energy physics to a spinless TLL.

Using a combination of both dc and microwave external fields, as discussed in section 8, it is also possible to engineer a t - J -like Hamiltonian with dipolar spin-exchange interactions, as described by the t - J - V - W Hamiltonian:

$$H_{tJVW} = -t \sum_{i,\sigma} (c_{i,\sigma}^\dagger c_{i+1,\sigma} + h. c.) + \sum_{i \neq j} |R_i - R_j|^{-3} \times \left[\frac{J_\parallel}{2} S_i^+ S_j^- + \frac{J_z}{2} S_i^z S_j^z + \frac{V}{2} n_{i,j} + W n_i S_j^z \right] \quad (114)$$

where $S_i^z = (n_{i,\uparrow} - n_{i,\downarrow})$ and $S_i^+ = c_{i,\uparrow}^\dagger c_{i,\downarrow}$. A complete investigation of the phase diagram of eq 114 is still lacking; nevertheless, the special case with $V = W = J_z = 0$, one of the simplest experimental realizations, has been numerically investigated in ref 227 by means of DMRG calculations; in this case, the main difference with respect to the standard t - J model resides in the long-range nature of the spin-exchange interactions, which are limited to nearest-neighbor in the t - J itself. At small values of J , the ground state is a spin-density wave (SDW) at all densities, resembling the ground state physics of the strongly repulsive Hubbard model.²⁴⁵ Then, increasing J , one enters first a region of singlet superfluidity (SS) with a finite spin gap (SG) and, finally, phase separation. In the SS region, interparticle attraction is encoded into the TLL parameter of the density (or charge²⁴⁵) sector $K_\rho > 1$. The main difference with the phase diagram of the t - J model, which is reported in the upper panel of Figure 40, is the presence of a larger gapped region;

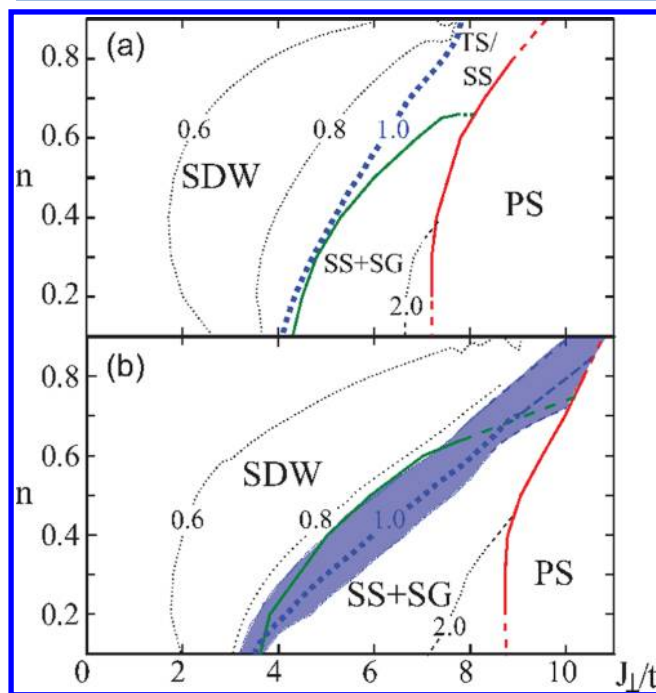


Figure 40. DMRG phase diagrams of the t - J (upper panel) and $tJVW$ (for $V = W = J_z = 0$, lower panel) models: blue dashed line denotes $K_\rho = 1$, and green thick line separates spin gapped (SS + SG) and gapless (SDW or SS/TS) regions. In the lower panel, the blue shaded region displays a charge Luttinger parameter $K_\rho = 1 \pm 0.15$ within numerical accuracy and, as such, may contain a gapless superfluid phase TS/SS. Image taken from ref 227. Copyright 2011 American Physical Society.

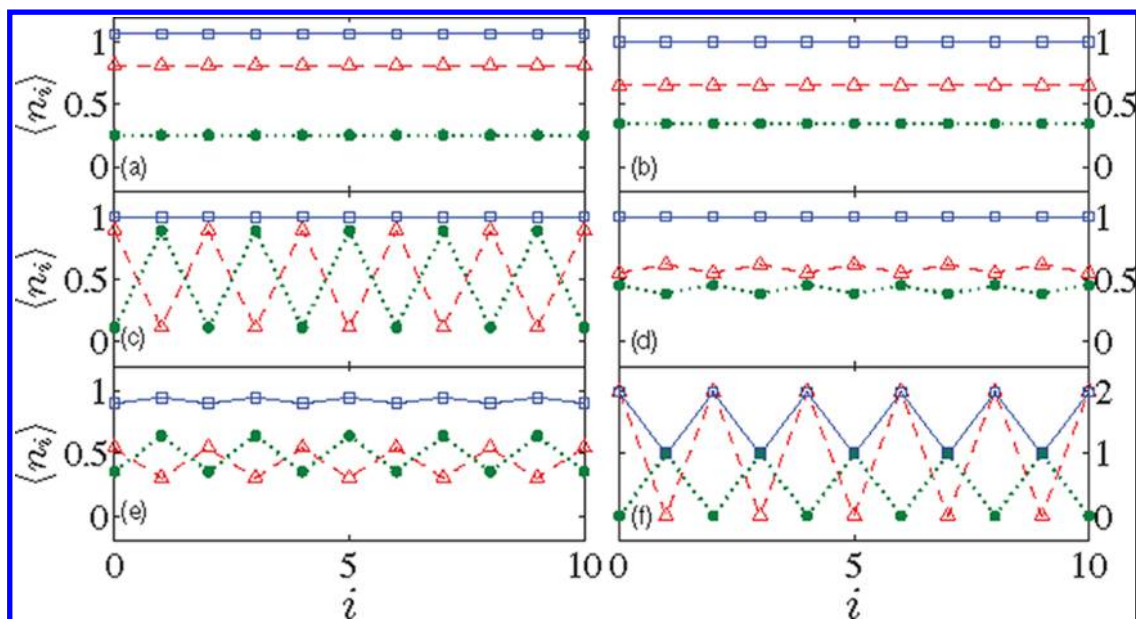


Figure 41. Density distribution n_B (triangles), n_F (filled circles), and $n_B + n_F$ (squares) for various phases as realized with dipolar Bose–Fermi mixtures: (a) BF liquid; (b) BF Mott insulator; (c and f) BF solids with different bosonic fillings; (d) density-wave BF Mott; (e) density-wave BF liquid. Results have been obtained by means of numerical iTEBD simulations. Image taken from ref 279. Copyright 2010 American Physical Society.

besides, the absence of a superfluid region with no spin gap (denoted as TS/SS) cannot be completely ruled out, as the broad blue region may indeed present such instability.

The realization of the $tJVW$ model with polar molecules presents two main advantages for the purpose of exploring the physics of the $t-J$ model with ultracold gases: first, the accessible regions are not limited to small exchange couplings $J \ll t$, and second, the spin gap in the superfluid region is twice larger, making such a phase more stable against thermal fluctuations.²²⁷

7.2.2. Bose–Fermi Mixtures. Multispecies gases with different statistics, that is Bose–Fermi (BF) mixtures, have been the subject of numerous theoretical and experimental efforts in the field of cold atoms, and they are currently being investigated even in the presence of dipolar interactions. In 1D, the effective Hamiltonian of such systems when confined in a deep optical lattice is as follows:

$$\begin{aligned}
 H_{BF} = & - \sum_{i,\sigma=B/F} [J_{\sigma}(a_{i,\sigma}^{\dagger}a_{i+1,\sigma} + h. c.) - \mu_{\sigma}n_{i,\sigma}] \\
 & + \sum_i n_{i,B} \left[U_{BF}n_F + \frac{U_{BB}}{2}(n_{i,B} - 1) \right] \\
 & + \sum_{\sigma,\delta} \sum_{i < j} \frac{V_{\sigma\delta}}{|i-j|^3} n_{i,\sigma} n_{j,\delta}
 \end{aligned} \quad (115)$$

where $a_{i,\sigma}^{\dagger}$ are creation operators obeying bosonic/fermionic statistics with $\sigma = B/F$, respectively, the first line contains both hopping and chemical potential terms, and the last two lines contain on-site and off-site interactions. The insulating instabilities of this Hamiltonian occurring close to half filling have been investigated in ref 279 by means of numerical simulations based on the iTEBD algorithm by truncating the dipolar interactions up to nearest-neighbors and considering several combinations in the broad parameter space of $\{J_{\sigma}U_{\sigma\delta}V_{\sigma\delta}\}$. In addition to gapless liquid and density-wave phases (a BF liquid, Figure 41a, and a BF density wave, Figure 41e), BF Mott phases with and without density oscillations are

present (a BF Mott insulator, Figure 41b, and a BF Mott density wave, Figure 41d). Finally, in the special case of half filling for both species, a BF solid, an incompressible phase with an alternating density pattern (Figure 41c and f), is also stable in the strongly interacting regime $U_{\sigma\delta} \gg J_{\sigma}$. Such a phase displays true-long-range order and, differently from the Néel antiferromagnetic case realized with purely contact interactions, is stable even when considering equal tunneling rates $J_B = J_F$; moreover, it displays very different melting processes as the interactions are increased depending on the relative value of V_{BB}/V_{FF} .²⁷⁹

7.3. Quasi-1D Physics: Coupling between Tubes

The long-range nature of dipolar interactions is well suited to create hybrid systems with purely 1D dynamics but 2D interactions, such as arrays of coupled tubes divided by very deep optical lattices preventing intertube tunneling together with a proper tuning of the external dc electric fields in order to manipulate the intertube interaction, as seen in section 2. Such systems establish a deep connection between the physics of several condensed matter systems, such as, e.g., spin compounds²⁴⁵ and ultracold dipolar gases which cannot be explored with contact interactions only. In the following, we first present recent results on the two-tube case, or *two-leg ladder*, and then consider the 2D limit where a large number of tubes, a *planar array*, is taken into account.

7.3.1. Two-Leg Ladders. Dipolar ladders allow investigation of rich physical phenomena by matching the advantages of reduced loss rates typical of 1D confinement with the possibility of considering multispecies physics, where the physical species index is represented by the wire one. (The case of multispecies gases confined in quasi-1D geometries, which allows treatment of problems with even more degrees of freedom, has attracted little attention so far.) In this respect, the special case of two-coupled tubes has been widely investigated. The effective Hamiltonian of such systems, in case an optical lattice in the tube direction is applied, is very similar to the case of a two-species gas,

$$H_L = -\sum_{\alpha,i} t_{\alpha} (c_{\alpha,i}^{\dagger} c_{\alpha,i+1} + h. c.) + \mu \sum_{\alpha,i} n_{i,\alpha} + \sum_{\alpha,\beta} \sum_{i,j} \mathcal{V}_{\alpha,\beta}(i,j) n_{i,\alpha} n_{j,\beta} \quad (116)$$

with the remarkable difference that here the anisotropic nature of the dipole–dipole interaction plays a prominent role. Here, $\alpha = 1, 2$ is the wire-index, and the specific shape of $\mathcal{V}_{\alpha\beta}(r)$ depends on both the interwire distance g and the angle between the dipole moments and the plane the ladder lies on. Moreover, for bosonic particles, an additional term $\sum_{i,\alpha} U n_{i,\alpha} (n_{i,\alpha} - 1)/2$ denotes the on-site interaction.

Bosonic Ladders. As a first step, it is worth considering if and how phases typical of 1D setups such as Mott insulators, superfluids, and Haldane insulators are changed in ladder geometries. In the case of interwire attraction, both MI and SF phases appear in the limit of small ($J/U \ll 1$) and large ($J/U \gg 1$) intrawire tunneling, respectively, and a pair superfluid phase (PSF), that is, a superfluid ground state of composite particles made of one boson on each tube, is stabilized at intermediate values of U/J .²⁸⁰ The Mott lobes close to the PSF phase have remarkably different excitations, that is, particle–hole are substituted by creation/annihilation of composite particles, further increasing the re-entrant shape of the Mott lobes, as can be seen in Figure 42. The evolution of the HI phase in ladder

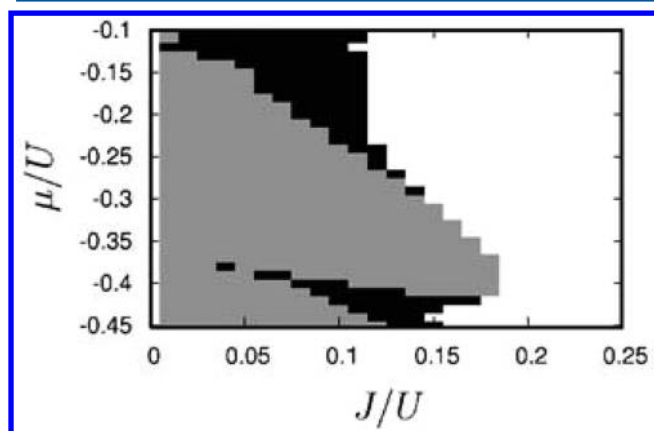


Figure 42. Numerical phase diagram of bosonic two-leg ladders with interwire nearest-neighbor attraction $\mathcal{V}_{12}(0)/U = -0.75$: white, gray, and black regions represent SF, PSF, and MI phases, respectively. Image taken from ref 280. Copyright 2007 American Physical Society.

setups is indeed more tantalizing, as in the case of spin-1 chains, it has been shown that the string order of the Haldane phase is unstable toward weak antiferromagnetic interchain exchange perturbations.²⁸¹ In the case of bosonics coupled tubes, combining TLL theory with renormalization group arguments, it has been shown²⁸² that, while a small intertube repulsion $\mathcal{V}_{12}(0)/J \ll 1$ changes only quantitatively the shape of the phase diagram, interchain tunneling terms of the type

$$H_{\perp} = J_{\perp} \sum_i (c_{i,1}^{\dagger} c_{i,2} + h. c.) \quad (117)$$

open an additional gapless, superfluid phase between the two: a schematic view of such changes is presented in Figure 43 and has been confirmed numerically via DMRG simulations.^{282,283}

Fermionic Ladders. Fermionic ladders present more instabilities with respect to the single tube, single species case. In the absence of a lattice, the weak-coupling phase

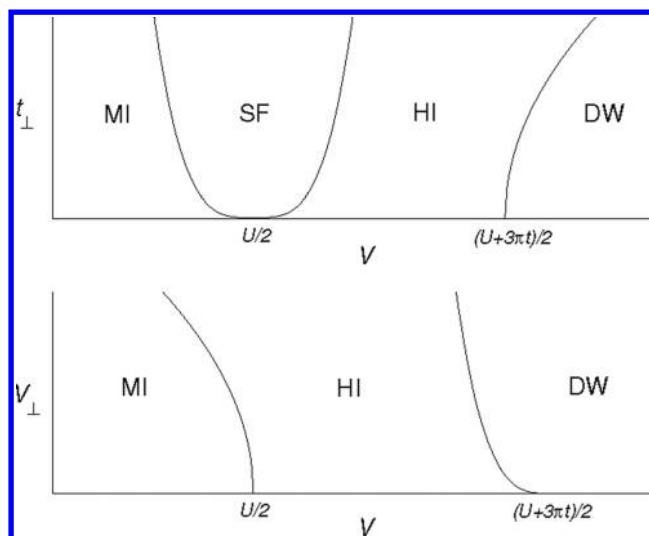


Figure 43. Qualitative changes in the phase diagram of two-coupled bosonic chains at unit filling and fixed U/J close to the HI phase. *Upper panel:* at finite interchain tunneling and no interchain interaction, a superfluid phase appears between the DW and the HI. *Lower panel:* at finite interchain interaction and no interchain tunneling, the phase diagram changes only quantitatively. Here, $V_{\perp} = \mathcal{V}_{12}(0)$, $t = J$ and $t_{\perp} = J_{\perp}$ fix the notations with respect to ref 282, from which this image has been taken. Copyright 2008 American Physical Society.

diagram has been investigated using the bosonization formalism^{247,246} in various setups.^{284,285} In the case of short-range interwire repulsion, the interplay between the longitudinal confinement length R , the interwire distance d , and the angle θ (see Figure 2) is responsible for the stabilization of three main phases. In the case of intrawire attraction, $\theta \lesssim 0.3\pi$, pairing on the single wire is favored, giving rise to a *triplet superfluid* phase (TS); in the opposite case of intrawire repulsion, $\theta \gtrsim 0.3\pi$, a spin density wave with alternating order (SDW_z) appears, while, in the intermediate regime $\theta \simeq 0.3\pi$, the dominant order is an in-plane spin-density wave (SDW_{xy}).²⁸⁴ In the case of a deep lattice, eq 116 becomes an extension of the so-called anisotropic extended Hubbard model (AEHM)²⁸⁶ with both large anisotropy and long-range, dipolar terms; while all the previous phases are expected to appear in the low-density limit, the possibility of tuning independently inter- and intrawire repulsion, making the former stronger than the latter, leads to a spontaneous breaking of the \mathbb{Z}_2 symmetry associated with the ladder geometry, stabilizing a fully *polarized* ground state where all particles stay on the same tube to minimize the intertube repulsion. Moreover, the addition of interwire tunneling terms (eq 117) may stabilize additional phases.²⁸⁴

When interwire interactions are turned attractive, a different physical picture arises depending on the population ratio between the wires, n_1/n_2 . When $n_1 = n_2$, pairing between the tubes is always favored, and the system behaves like a quantum liquid of composite bosonic particles made of one boson per wire; such a liquid can be both a superfluid (that is, a PSF) and a CDW depending on both the interwire distance and dipole strength.²⁸⁵ If a shallow optical lattice commensurate with the particle density is introduced along the tube direction, that is its lattice wavelength λ satisfies $2/n_1\lambda \in \mathbb{N}$, the system can undergo a BKT transition to a composite crystal as a function of the lattice depth, in analogy with what happens in the single tube bosonic case (see section 7.1.1): in a grand canonical ensemble,

this picture evolves, establishing a Luttinger staircase of dimer crystals.²⁸⁵ In the deep lattice case, these predictions have been checked by means of DMRG simulations.

Imbalanced Ladders. A completely different phenomenon occurs in the presence of a density imbalance between the tubes (Figure 44). For interwire distances g larger than the inverse

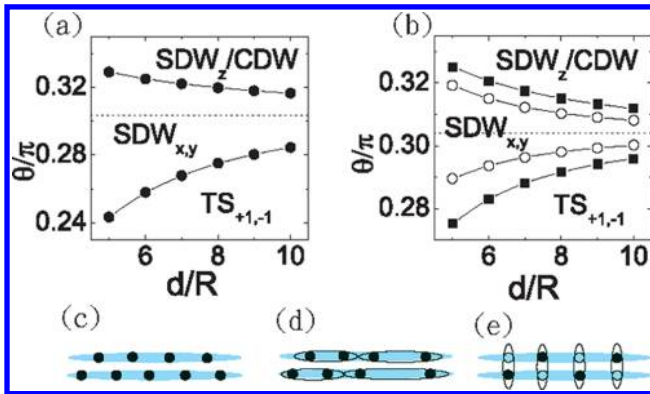


Figure 44. Panels a and b: phase diagram of fermionic two-leg ladders with interwire nearest-neighbor attraction repulsion as a function of the interwire distance-to-wire width ratio d/R and the angle θ (see Figure 2); $k_F R = 0.1, 0.2$ in the left and right panels, respectively, where k_F is the Fermi momentum of the single tube. Panels c, d, and e: cartoons of the SDW_z, TS, and SDW_{x,y} phases discussed in the text; horizontal ellipses denote pairing between particles in the same tube, while intertube correlation is indicated by vertical ellipses. Image taken from ref 284. Copyright 2008 American Physical Society.

particle density, the long-range nature of the dipolar interaction creates an effective fixed range interwire attraction, thus favoring pairing not only between two, but also between many, particles. In the special case of commensurate densities between the wires, $n_1/n_2 = p/q \in \mathbb{Q}$, a gas of composite particles, or *multimers*, composed by $p(q)$ particles in the first (second) wire, respectively, can be stabilized for sufficiently low densities.²⁸⁵ Such a multimer liquid picture has a description in terms of low-energy field theory²⁸⁷ and allows study of the generalized pairing mechanism beyond two-particle ones. In the special case of $p = 1, q = 2$, the stability of *trimer liquids* has been confirmed numerically for sufficiently large tunneling and dipole imbalance between the tubes. When a trapping potential and a nonideal population ratio are also considered, such trimer liquids (which are not stable in homogeneous setups with unmatched densities) appear in the center of the system and are surrounded by both dimer liquids or single species ones, depending on the population ration, forming a pancake-like structure of composite liquids (see Figure 45) as shown in recent DMRG simulations.²⁸⁵

The possibility of further tuning the numerous parameters of the ladder Hamiltonian (eq 116) may indeed allow identification of an additional exotic state of matter, as the complete phase diagram of these system is still largely unexplored. Moreover, before turning our attention to systems composed by a large number of tubes, it is worth noticing that ladder systems with more than two tubes and mixtures in quasi-1D geometries are in principle good candidates to study new model Hamiltonians in connection to many-body problems with many degrees of freedom.

7.3.2. Planar Array of Tubes. Planar arrays of tubes of dipolar gases constitute a hybrid setup where one can investigate 2D states of matter with physical properties typical

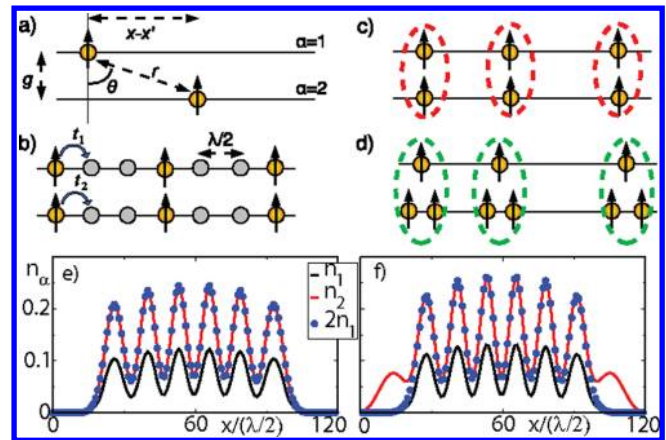


Figure 45. Panel a: typical configuration of two-leg ladder with attractive short-distance interaction between the wires. Panels b–d: cartoons of a dimer crystal (b), a dimer liquid (or PSF; c), and a trimer liquid (d). Panels e and f: typical density distribution of strongly imbalanced wires with $2n_1 \lesssim n_2$ (see ref 285 for technical details). In both cases, the density match $n_2 = 2n_1$ in the central part of the system indicates the presence of a trimer liquid. Image taken from ref 285. Copyright 2011 American Physical Society.

of 1D systems such as, e.g., the quasi long-range order of the correlation functions. Even in this case, the effective Hamiltonian

$$H_{plane} = \sum_{\alpha,j} \int dx \psi_{\alpha,j}^\dagger(x) \left(-\frac{\hbar^2}{2m} \partial_x^2 \right) \psi_{\alpha,j}(x) + \sum_{\alpha,\beta,j,l} \int dx dx' \rho_{\alpha,j}(x) \rho_{\beta,l}(x') \mathcal{V}_{\alpha\beta}(x, x')$$

has many controllable parameters: here, $\psi_\omega^\dagger \psi_\omega$ are the creation/annihilation operators on the tube α (sums over Greek indices denote sums over the tube index, while Latin indices denote particles along each tube), $\rho_\alpha = \psi_\alpha^\dagger \psi_\alpha$ the first term represents the kinetic energy over each tube, and the second one the dipolar interactions, which depend on both strength and orientation of the dipole moments. In the zero-density limit, where only one bosonic particle per wire is considered and interwire interactions are attractive, a *quantum rough chain* forms with the off-diagonal long-range order in the M -body correlation function, where M is the number of wires.²⁸⁸

In the finite density regime, the many-body physics displays very different effects. In the bosonic case with intrawire dipolar repulsion, the competition between local interactions and long-range ones is encoded into a dimensionless parameter $\gamma = 4V_0 K / (ua^2)$, where u and K are the sound velocity and the TLL parameter of a single tube, V_0 is the strength of the dipolar interactions, and a is the intertube spacing. By varying both K and γ , one can span a broad parameter region with respect to the dipolar interaction, the density of particles, and the s -wave scattering length a_{1D} .²⁸⁹ In addition to a series of density wave states driven by the strong dipolar repulsion, which may lead to both a stripe and checkerboard order depending on the relative strength between inter- and intratube repulsion, a gapless phase (denoted as (i) in Figure 46) with dominant superfluid correlations along the tubes is present for large values of K (that is, for weak intratube interactions).²⁸⁹ Such a phase, which despite being effectively two-dimensional still preserves an algebraic decay of correlation functions typical of the quasi-long-range order of 1D systems, is known as sliding Luttinger

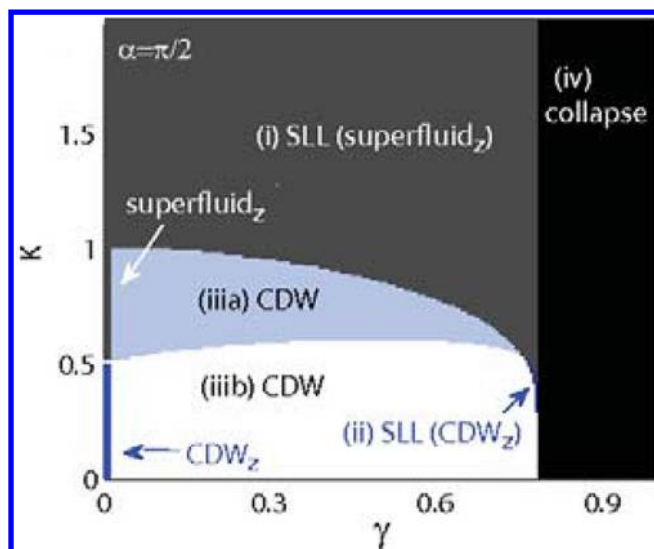


Figure 46. Phase diagram of a planar array of dipolar bosons as a function of the single wire Luttinger parameter K and the ratio between the dipolar interaction and the scattering length $\gamma = 4V_0K/(a^2U)$ (see text). Here, the angle θ (α according to notations in ref 289) is fixed at $\pi/2$. Image taken from ref 289. Copyright 2008 American Physical Society.

liquid (SLL) and has been investigated even in several fermionic models related to stripe physics and high- T_c superconductivity.²⁹⁰ Moreover, the SLL phase may also have dominant density–density correlation along the tube in a tiny region at intermediate γ (denoted as (ii)). In the strongly interacting regime, a collapsed regime takes place, whose precise shape depends on the sign of the intertube interactions. The complete phase diagram for a fixed value of the angle θ is shown in Figure 46.

The planar array of fermionic dipoles displays a different phase diagram; albeit, some features such as the density wave patterns emerge independently on the statistics. The phase diagram of this system as a function of the angles θ and ϕ (see Figure 2) has been derived in the framework of a generalized TLL theory²⁹¹ by comparing the long-distance decay of several correlation functions, as reported in Figure 47. When both

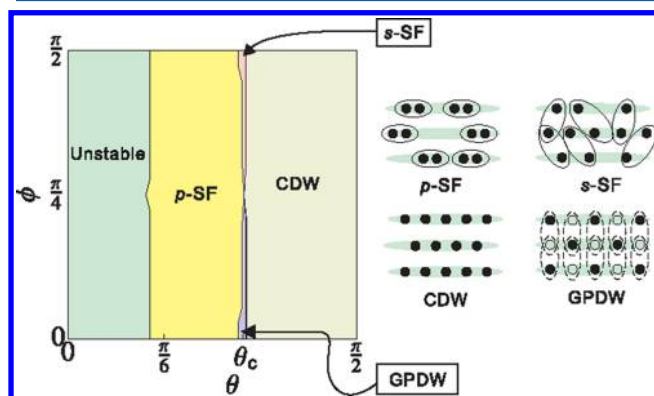


Figure 47. Left panel: schematic phase diagram of a planar array of fermionic dipolar tubes as a function of the angles θ and ϕ ; all phases are discussed in the text, and their cartoons are presented in the right panel, where solid ellipses denote (intra- or intertube) pairing and shaded ones indicate intertube coherence. Image taken from ref 291. Copyright 2008 American Physical Society.

inter- and intratube interactions are strongly repulsive, the ground state exhibits CDW (checkerboard) order, similarly to the bosonic case. Close to the magic angle $\theta = \theta_c = 0.3\pi$, where the intrawire interaction turns from repulsive to attractive, an intertube superfluid (*s*-SF) phase together with a density wave with broken particle number conservation along the tubes (or gauge-phase density wave, GPDW) are present. Finally, for attractive intratube interactions, a *p*-wave superfluid (*p*-SF) is the precursor of an unstable phase toward intratube collapse.

8. CONCLUSIONS AND OUTLOOK

The many-body systems discussed in this review are examples of the variety of physical properties which originate from the anisotropy and long-range character of dipole–dipole interactions, in combination with their tunability with external fields. In many physical situations, quantum dipolar gases behave qualitatively differently when compared to atomic gases with short-range van der Waals interactions, and they provide us with a large number of novel quantum systems with unique physical properties. Understanding the many-body behavior of these systems is a very interesting and challenging problem with several potentially significant consequences for fundamental science and practical applications.

In the present review we have focused on dipolar quantum gases represented by polar molecules in the rovibrational ground state. An alternative realization of a dipolar quantum gas, although in a completely different regime, is a gas of laser excited Rydberg atoms²⁹² or molecules.^{293,294} Highly excited Rydberg atoms and molecules interact via remarkably strong electric dipole moments or van der Waals interactions. This leads to the phenomenon of a *dipole blockade* and formation of *superatoms* where within a given blockade radius only a single Rydberg atom can be excited and, for example, crystals of these superatoms can be formed.²⁹² In view of the finite lifetime of Rydberg states, these many body phases will only exist for a comparatively short time in the so-called *frozen gas* regime where there is no atomic motion. However, as discussed in ref 150, the large Rydberg dipoles can also be admixed weakly to the ground state by off-resonant laser excitation, which provides a situation loosely reminiscent of the polar molecule case, although decoherence due to spontaneous emission remains always an issue.

Finally, we remark that the tools for manipulating interactions in dipolar systems, as described in the present review, also provide promising ingredients for controlled entanglement between polar molecules, and thus possible new scenarios for quantum computing.^{295–297} Loading exactly one atom or molecule per lattice site via a Mott insulator transition in an optical lattice provides us with an array of qubits. In the case of polar molecules, the qubits can be represented by long-lived rotational or spin degrees of freedom. Single site addressing, as developed in refs 6 and 7 for atoms, allows both manipulation of as well as reading of the single qubit. Entanglement of qubits can be achieved via the strong and long-range dipolar interactions between molecules^{295–297} or, in the atomic case, via dipolar Rydberg interactions.²⁹²

AUTHOR INFORMATION

Corresponding Author

*E-mail: Peter.Zoller@uibk.ac.at.

Notes

The authors declare no competing financial interest.

Biographies



Mikhail Baranov is a senior researcher at the Austrian Academy of Sciences in Innsbruck. He received his M.S. in Theoretical Physics in 1984 from the Moscow Institute of Engineering and Physics, Russia, and his Ph.D. in Physics and Mathematics in 1987 at the same institute. In 2008 he joined Prof. Zoller's group at Innsbruck. His scientific interests are many-body systems, strongly correlated states, and ultracold atomic and molecular gases.



Marcello Dalmonte is Junior Scientist at the Austrian Academy of Sciences in Innsbruck. He received both his M.S. (2007) and Ph.D. (April 2011) from the Department of Physics of the University of Bologna (Italy), working under the supervision of Dr. Elisa Ercolessi. During his studies, he spent several months as a visiting student at the Institute for Theoretical Physics in Innsbruck. His main research interests include different aspects of many-body theories in one-dimensional geometries, with particular focus on quantum phenomena and strong correlations in ultracold atomic and molecular gases.



Guido Pupillo is professor at the University of Strasbourg and director of the Laboratory of Quantum Physics at the Institut de Science d'Ingénierie Supramoléculaires and the Institut de Physique et Chimie des Matériaux in Strasbourg. He received his Ph.D. in Physics from the University of Maryland in the USA, for research conducted at the National Institute of Standards and Technology (Gaithersburg). In 2005 he joined Prof. Zoller's group at the University of Innsbruck, where he received the Habilitation for professorship in theoretical physics in 2011. His research interests focus on the physics of strongly correlated atomic and molecular gases.



Peter Zoller is professor at the University of Innsbruck and works on quantum optics and quantum information. He obtained his Doctorate from the University of Innsbruck in 1977, and the Habilitation for professorship in 1981. After spending several years as a visiting fellow, from 1991 to 1994 he was professor of physics and JILA Fellow at JILA and at the Physics Department of the University of Colorado, Boulder, USA. Back in Innsbruck, from 1995 to 1999 he headed the Institute of Theoretical Physics and was vice-dean of studies from 2001 to 2004. He was Loeb lecturer at Harvard, Boston, MA (2004), Yan Jici chair professor at the University of Science and Technology of China, Hefei, and chair professor at Tsinghua University, Beijing (2004), as well as Lorentz professor at the University of Leiden in The Netherlands (2005). Since 2003, Peter Zoller has also held the position of Scientific Director at the Institute for Quantum Optics and Quantum Information (IQOQI) of the Austrian Academy of Sciences. He is the recipient of several international prizes, including the Benjamin Franklin Medal in Physics (2010), the Dirac Medal (2006), the Niels Bohr/UNESCO Gold Medal (2005), and the Max Planck Medaille 2005. He is best known for his research on quantum computing and quantum communication and for bridging quantum optics and solid state physics.

ACKNOWLEDGMENTS

We would like to thank I. Bloch, D. Blume, J. Bohn, H. P. Büchler, L. D. Carr, N. R. Cooper, R. Côté, D. DeMille, E. Demler, J. Doyle, F. Ferlaino, A. Gorshkov, M. Lewenstein, M. Lukin, D. Jin, P. Julienne, R. Krems, B. Lev, G. Meijer, H. C. Nägerl, D. Petrov, T. Pfau, G. Quéméner, L. Santos, G. Shlyapnikov, J. Ye, S. Yelin, D.-W. Wang, and M. Weidemüller for many interesting discussions on the topics treated in this review. This work was supported by the Austrian Science Fund, by EU grants AQUITE, COHERENCE, and NAME-QUAM, and by MURI, AFOSR, ISIS, EOARD, IPCMS, and the RTRA Foundation.

REFERENCES

(1) Metcalf, H. J.; van der Straten, P. *Laser Cooling and Trapping*; Springer-Verlag: New York, 1999.

- (2) Chin, C.; Grimm, R.; Julienne, P.; Tiesinga, E. *Rev. Mod. Phys.* **2010**, *82*, 1225–1286.
- (3) Bloch, I.; Dalibard, J.; Zwerger, W. *Rev. Mod. Phys.* **2008**, *80*, 885.
- (4) Bloch, I. *Nature Phys.* **2005**, *1*, 23.
- (5) Greiner, M.; Fölling, S. *Nature* **2008**, *453*, 736.
- (6) Bakr, W. S.; Gillen, J. I.; Peng, A.; Fölling, S.; Greiner, M. *Nature* **2009**, *462*, 74.
- (7) Sherson, J.; Weitenberg, C.; Endres, M.; Cheneau, M.; Bloch, I.; Kuhr, S. *Nature* **2010**.
- (8) Inguscio, M., Ketterle, W., Salomon, C., Eds.; *Proceedings of the International School of Physics Enrico Fermi, Course CLXIV, Varenna, 20–30 June 2006*; IOP Press: Amsterdam, 2008.
- (9) Hadzibabic, Z.; Kruger, P.; Cheneau, M.; Battelier, B.; Dalibard, J. *Nature* **2006**, *441*, 1118–1121.
- (10) Griesmaier, A.; Werner, J.; Hensler, S.; Stuhler, J.; Pfau, T. *Phys. Rev. Lett.* **2005**, *94*, 160401.
- (11) Stuhler, J.; Griesmaier, A.; Koch, T.; Fattori, M.; Pfau, T.; Giovanazzi, S.; Pedri, P.; Santos, L. *Phys. Rev. Lett.* **2005**, *95*, 150406.
- (12) Fattori, M.; Koch, T.; Goetz, S.; Griesmaier, A.; Hensler, S.; Stuhler, J.; Pfau, T. *Nat. Phys.* **2006**, *2*, 765–768.
- (13) Griesmaier, A.; Stuhler, J.; Koch, T.; Fattori, M.; Pfau, T.; Giovanazzi, S. *Phys. Rev. Lett.* **2006**, *97*, 250402.
- (14) Lahaye, T.; Koch, T.; Fröhlich, B.; Fattori, M.; Metz, J.; Griesmaier, A.; Giovanazzi, S.; Pfau, T. *Nature* **2007**, *448*, 672–675.
- (15) Koch, T.; Lahaye, T.; Metz, J.; Fröhlich, B.; Griesmaier, A.; Pfau, T. *Nat. Phys.* **2008**, *4*, 218–222.
- (16) Lahaye, T.; Metz, J.; Fröhlich, B.; Koch, T.; Meister, M.; Griesmaier, A.; Pfau, T.; Saito, H.; Kawaguchi, Y.; Ueda, M. *Phys. Rev. Lett.* **2008**, *101*, 080401.
- (17) Aikawa, K.; Frisch, A.; Mark, M.; Baier, S.; Rietzler, A.; Grimm, R.; Ferlaino, F. *Phys. Rev. Lett.* **2012**, *108*, 210401.
- (18) Lu, M.; Burdick, N. Q.; Youn, S. H.; Lev, B. L. *Phys. Rev. Lett.* **2011**, *107*, 190401.
- (19) Lu, M.; Burdick, N. Q.; Lev, B. L. *Phys. Rev. Lett.* **2012**, *108*, 215301.
- (20) Weinstein, J. D.; DeCarvalho, R.; Guillet, T.; Friedrich, B.; Doyle, J. M. *Nature* **1998**, *395*, 148–150.
- (21) Doyle, J. M.; Friedrich, B. *Nature* **1999**, *401*, 749–751.
- (22) Bethlem, H. L.; Berden, G.; Meijer, G. *Phys. Rev. Lett.* **1999**, *83*, 1558–1561.
- (23) Bethlem, H. L.; Berden, G.; van Roij, A. J. A.; Crompvoets, F. M. H.; Meijer, G. *Phys. Rev. Lett.* **2000**, *84*, 5744–5747.
- (24) Bethlem, H. L.; Berden, G.; Crompvoets, F. M. H.; Jongma, R. T.; van Roij, A. J. A.; Meijer, G. *Nature* **2000**, *406*, 491–495.
- (25) Bethlem, H. L.; Crompvoets, F. M. H.; Jongma, R. T.; van de Meerakker, S. Y. T.; Meijer, G. *Phys. Rev. A* **2002**, *65*, 053416.
- (26) *Special Issue on “Ultracold Polar Molecules: Formation and Collisions”*; Doyle, J., Friedrich, B., Krems, R. V., Masnou-Seeuws, F., Eds.; *Eur. Phys. J. D* **2004**; Vol. 31.
- (27) van de Meerakker, S. Y. T.; Smeets, P. H. M.; Vanhaecke, N.; Jongma, R. T.; Meijer, G. *Phys. Rev. Lett.* **2005**, *94*, 023004.
- (28) Bochinski, J. R.; Hudson, E. R.; Lewandowski, H. J.; Ye, J. *Phys. Rev. A* **2004**, *70*, 043410.
- (29) Wang, D.; Qi, J.; Stone, M.; Nikolayeva, O.; Hattaway, B.; Gensemer, S.; Wang, H.; Zemke, W.; Gould, P.; Eyler, E.; Stwalley, W. *Eur. Phys. J. D* **2004**, *31*, 165.
- (30) Egorov, D.; Campbell, W. C.; Friedrich, B.; Maxwell, S. E.; Tsikata, E.; van Buuren, L. D.; Doyle, J. M. *Eur. Phys. J. D—At., Mol., Opt. Plasma Phys.* **2004**, *31*, 307–311.
- (31) Sage, J. M.; Sainis, S.; Bergeman, T.; DeMille, D. *Phys. Rev. Lett.* **2005**, *94*, 203001.
- (32) Baranov, M. *Phys. Rep.* **2008**, *464*, 71–111.
- (33) Carr, L. D.; DeMille, D.; Krems, R. V.; Ye, J. *New J. Phys.* **2009**, *11*, 055049.
- (34) Lahaye, T.; Menotti, C.; Santos, L.; Lewenstein, M.; Pfau, T. *Rep. Prog. Phys.* **2009**, *72*, 126401.
- (35) Krems, R. V.; Stwalley, W. C.; Friedrich, B. *Cold Molecules: Theory, Experiment, Applications*; CRC Press: 2009.
- (36) Trefzger, C.; Menotti, C.; Capogrosso-Sansone, B.; Lewenstein, M. *J. Phys. B: At. Mol. Opt. Phys.* **2011**, *44*, 193001.
- (37) Müller, S.; Billy, J.; Henn, E. A. L.; Kadau, H.; Griesmaier, A.; Jona-Lasinio, M.; Santos, L.; Pfau, T. *Phys. Rev. A* **2011**, *84*, 053601.
- (38) Marinescu, M.; You, L. *Phys. Rev. Lett.* **1998**, *81*, 4596–4599.
- (39) Deb, B.; You, L. *Phys. Rev. A* **2001**, *64*, 022717.
- (40) Yi, S.; You, L. *Phys. Rev. A* **2000**, *61*, 041604.
- (41) Ronen, S.; Bortolotti, D. C. E.; Blume, D.; Bohn, J. L. *Phys. Rev. A* **2006**, *74*, 033611.
- (42) Derevianko, A. *Phys. Rev. A* **2003**, *67*, 033607.
- (43) Derevianko, A. *Phys. Rev. A* **2005**, *72*, 039901.
- (44) Bortolotti, D. C. E.; Ronen, S.; Bohn, J. L.; Blume, D. *Phys. Rev. Lett.* **2006**, *97*, 160402.
- (45) Giovanazzi, S.; Görlitz, A.; Pfau, T. *Phys. Rev. Lett.* **2002**, *89*, 130401.
- (46) Mehring, M. *Principles of High Resolution NMR in Solids*; Springer: Berlin, 1983.
- (47) Zuchowski, P. S.; Hutson, J. M. *Phys. Rev. A* **2010**, *81*, 060703.
- (48) Idziaszek, Z.; Julienne, P. S. *Phys. Rev. Lett.* **2010**, *104*, 113202.
- (49) Idziaszek, Z.; Quemener, G.; Bohn, J. L.; Julienne, P. S. *Phys. Rev. A* **2010**, 020703 (R).
- (50) Ni, K.-K.; Ospelkaus, S.; Wang, D.; Quemener, G.; Neyenhuis, B.; de Miranda, M. H. G.; Bohn, J. L.; Ye, J.; Jin, D. S. *Nature* **2010**, *464*, 1324.
- (51) de Miranda, M. H. G.; Chotia, A.; Neyenhuis, B.; Wang, D.; Quemener, G.; Ospelkaus, S.; Bohn, J. L.; Ye, J.; Jin, D. S. *Nature Phys.* **2011**, *7*, 502.
- (52) Ticknor, C. *Phys. Rev. A* **2010**, *81*, 042708.
- (53) Quémener, G.; Bohn, J. L. *Phys. Rev. A* **2010**, *81*, 060701(R).
- (54) Petrov, D.; Shlyapnikov, G. *Phys. Rev. A* **2001**, *64*, 012706.
- (55) Li, Z.; Alyabyshev, S. V.; Krems, R. V. *Phys. Rev. Lett.* **2008**, *100*, 073202.
- (56) Li, Z.; Krems, R. V. *Phys. Rev. A* **2009**, *79*, 050701.
- (57) Micheli, A.; Pupillo, G.; Büchler, H. P.; Zoller, P. *Phys. Rev. A* **2007**, *76*, 043604.
- (58) Gribakin, G. F.; Flambaum, V. V. *Phys. Rev. A* **1993**, *48*, 546.
- (59) Julienne, P. S. *Faraday Discuss.* **2009**, *142*, 361.
- (60) Micheli, A.; Idziaszek, Z.; Pupillo, G.; Baranov, M. A.; Zoller, P.; Julienne, P. S. *Phys. Rev. Lett.* **2010**, *105*, 073202.
- (61) Julienne, P. S.; Hanna, T. M.; Idziaszek, Z. *Phys. Chem. Chem. Phys.* **2011**.
- (62) Coleman, S. *Phys. Rev. D* **1977**, *15*, 2929–2936.
- (63) Quémener, G.; Bohn, J. L. *Phys. Rev. A* **2010**, *81*, 022702.
- (64) Büchler, H. P.; Demler, E.; Lukin, M.; Micheli, A.; Prokof'ev, N.; Pupillo, G.; Zoller, P. *Phys. Rev. Lett.* **2007**, *98*, 60404.
- (65) Zilio, S. C.; Marcassa, L.; Muniz, S.; Horowicz, R.; Bagnato, V.; Napolitano, R.; Weiner, J.; Julienne, P. S. *Phys. Rev. Lett.* **1996**, *76*, 2033–2036.
- (66) Napolitano, R.; Weiner, J.; Julienne, P. S. *Phys. Rev. A* **1997**, *55*, 1191–1207.
- (67) Weiner, J.; Bagnato, V. S.; Zilio, S.; Julienne, P. S. *Rev. Mod. Phys.* **1999**, *71*, 1–85.
- (68) Gorshkov, A. V.; Rabl, P.; Pupillo, G.; Micheli, A.; Zoller, P.; Lukin, M. D.; Büchler, H. P. *Phys. Rev. Lett.* **2008**, *101*, 073201.
- (69) Aldegunde, J.; Ran, H.; Hutson, J. M. *Phys. Rev. A* **2009**, *80*, 043410.
- (70) Ran, H.; Aldegunde, J.; Hutson, J. M. *New J. Phys.* **2010**, *12*, 043015.
- (71) Ticknor, C.; Bohn, J. L. *Phys. Rev. A* **2005**, *72*, 032717.
- (72) Dalfovo, F.; Giorgini, S.; Pitaevskii, L. P.; Stringari, S. *Rev. Mod. Phys.* **1999**, *71*, 463–512.
- (73) Yi, S.; You, L. *Phys. Rev. A* **2001**, *63*, 053607.
- (74) Santos, L.; Shlyapnikov, G. V.; Zoller, P.; Lewenstein, M. *Phys. Rev. Lett.* **2000**, *85*, 1791–1794.
- (75) Lushnikov, P. M. *Phys. Rev. A* **2002**, *66*, 051601.
- (76) Santos, L.; Shlyapnikov, G. V.; Zoller, P.; Lewenstein, M. *Phys. Rev. Lett.* **2002**, *88*, 139904.
- (77) Dutta, O.; Meystre, P. *Phys. Rev. A* **2007**, *75*, 053604.

- (78) Eberlein, C.; Giovanazzi, S.; O'Dell, D. H. J. *Phys. Rev. A* **2005**, *71*, 033618.
- (79) Ronen, S.; Bortolotti, D. C. E.; Bohn, J. L. *Phys. Rev. Lett.* **2007**, *98*, 030406.
- (80) Góral, K.; Rzażewski, K.; Pfau, T. *Phys. Rev. A* **2000**, *61*, 051601.
- (81) Martikainen, J.-P.; Mackie, M.; Suominen, K.-A. *Phys. Rev. A* **2001**, *64*, 037601.
- (82) Santos, L.; Shlyapnikov, G. V.; Lewenstein, M. *Phys. Rev. Lett.* **2003**, *90*, 250403.
- (83) Ruprecht, P. A.; Edwards, M.; Burnett, K.; Clark, C. W. *Phys. Rev. A* **1996**, *54*, 4178–4187.
- (84) Góral, K.; Santos, L. *Phys. Rev. A* **2002**, *66*, 023613.
- (85) O'Dell, D. H. J.; Giovanazzi, S.; Eberlein, C. *Phys. Rev. Lett.* **2004**, *92*, 250401.
- (86) Baranov, M. A.; Dobrek, Ł.; Góral, K.; Santos, L.; Lewenstein, M. *Phys. Scr.* **2002**, *2002*, 74.
- (87) Fischer, U. R. *Phys. Rev. A* **2006**, *73*, 031602.
- (88) Stringari, S. *Phys. Rev. A* **1998**, *58*, 2385–2388.
- (89) Landau, L. D.; Lifshitz, L. M. *Quantum Mechanics {Non-Relativistic} Theory*, 3rd ed; Butterworth-Heinemann: 1981; Vol. 3.
- (90) Lifshitz, E.; Pitaevskii, L. *Statistical Physics, Part 2*; Butterworth-Heinemann: 1980.
- (91) Pomeranchuk, I. *Sov. Phys. JETP* **1958**, *8*, 361.
- (92) Miyakawa, T.; Sogo, T.; Pu, H. *Phys. Rev. A* **2008**, *77*, 061603.
- (93) Sogo, T.; He, L.; Miyakawa, T.; Yi, S.; Pu, H. *New J. Phys.* **2008**, *11*, 055017.
- (94) Ronen, S.; Bohn, J. L. *Phys. Rev. A* **2010**, *81*, 033601.
- (95) Chan, C.-K.; Wu, C.; Lee, W.-C.; Das Sarma, S. *Phys. Rev. A* **2010**, *81*, 023602.
- (96) Kestner, J. P.; Das Sarma, S. *Phys. Rev. A* **2010**, *82*, 033608.
- (97) Sieberer, L. M.; Baranov, M. A. *Phys. Rev. A* **2011**, *84*, 063633.
- (98) Lu, Z.-K.; Shlyapnikov, G. V. *Phys. Rev. A* **2012**, *85*, 023614.
- (99) You, L.; Marinescu, M. *Phys. Rev. A* **1999**, *60*, 2324–2329.
- (100) Stoof, H.; Houbiers, M. 1999, arXiv:9808171.
- (101) Baranov, M. A.; Mar'enko, M. S.; Rychkov, V. S.; Shlyapnikov, G. V. *Phys. Rev. A* **2002**, *66*, 013606.
- (102) J. Bardeen, L. C.; Schrieffer, J. *Phys. Rev.* **1957**, *108*, 1175.
- (103) Leggett, A. J. *Rev. Mod. Phys.* **1975**, *47*, 331.
- (104) Gor'kov, L.; Melik-Barkhudarov, T. *Sov. Phys. JETP* **1961**, *13*, 1018.
- (105) Vollhardt, D.; Wölfle, P. *The Superfluid Phases of Helium 3*; Taylor and Francis: London, 1990.
- (106) Volovik, G.; Gor'kov, L. *Sov. Phys. JETP* **1985**, *61*, 843.
- (107) Marchenko, V. *Sov. Phys. JETP* **1986**, *66*, 331.
- (108) Sigrist, M.; Ueda, K. *Rev. Mod. Phys.* **1991**, *63*, 239–311.
- (109) Fisher, R. A.; Kim, S.; Woodfield, B. F.; Phillips, N. E.; Taillefer, L.; Hasselbach, K.; Flouquet, J.; Giorgi, A. L.; Smith, J. L. *Phys. Rev. Lett.* **1989**, *62*, 1411–1414.
- (110) Baranov, M. A.; Dobrek, Ł.; Lewenstein, M. *New J. Phys.* **2004**, *6*, 198.
- (111) Baranov, M. A.; Petrov, D. S. *Phys. Rev. A* **1998**, *58*, R801–R804.
- (112) Bruun, G.; Castin, Y.; Dum, R.; Burnett, K. *Eur. Phys. J. D* **1999**, *7*, 433.
- (113) Viverit, L.; Bruun, G. M.; Minguzzi, A.; Fazio, R. *Phys. Rev. Lett.* **2004**, *93*, 110406.
- (114) Shi, T.; Zhang, J.-N.; Sun, C.-P.; Yi, S. *Phys. Rev. A* **2010**, *82*, 033623.
- (115) Bruun, G. M.; Taylor, E. *Phys. Rev. Lett.* **2008**, *101*, 245301.
- (116) Berezinskii, V. L. *JETP* **1972**, *34*, 610.
- (117) Kosterlitz, J. M.; Thouless, D. J. *J. Phys. C* **1973**, *6*, 1181.
- (118) Kosterlitz, J. J. *J. Phys. C: Solid State Phys.* **1974**, *7*, 1046–1060.
- (119) Miyake, K. *Prog. Theor. Phys.* **1983**, *69*, 1794–1797.
- (120) Cooper, N. R.; Shlyapnikov, G. V. *Phys. Rev. Lett.* **2009**, *103*, 155302.
- (121) Levinsen, J.; Cooper, N. R.; Shlyapnikov, G. V. *Phys. Rev. A* **2011**, *84*, 013603.
- (122) Volovik, G. *Exotic Properties of Superfluid ³He*; World Scientific: Singapore, 1992.
- (123) Read, N.; Green, D. *Phys. Rev. B* **2000**, *61*, 10267–10297.
- (124) Stern, A. *Ann. Phys.* **2008**, *323*, 204–249.
- (125) Nayak, C.; Simon, S. H.; Stern, A.; Freedman, M.; Das Sarma, S. *Rev. Mod. Phys.* **2008**, *80*, 1083–1159.
- (126) Pikovski, A.; Klawunn, M.; Shlyapnikov, G. V.; Santos, L. *Phys. Rev. Lett.* **2010**, *105*, 215302.
- (127) Baranov, M. A.; Micheli, A.; Ronen, S.; Zoller, P. *Phys. Rev. A* **2011**, *83*, 043602.
- (128) Klawunn, M.; Pikovski, A.; Santos, L. *Phys. Rev. A* **2010**, *82*, 044701.
- (129) Taylor, J. *Scattering Theory*; John Wiley and Sons: New York, 1972.
- (130) Zinner, N. T.; Wunsch, B.; Pekker, D.; Wang, D.-W. *Phys. Rev. A* **2012**, *85*, 013603.
- (131) Góral, K.; Englert, B.-G.; Rzażewski, K. *Phys. Rev. A* **2001**, *63*, 033606.
- (132) Pines, D.; Nozieres, P. *The Theory of Quantum Liquids*; W.A. Benjamin, Inc.: 1966.
- (133) Sun, K.; Wu, C.; Das Sarma, S. *Phys. Rev. B* **2010**, *82*, 075105.
- (134) Zinner, N. T.; Bruun, G. M. *Eur. Phys. J. D* **2011**, *65*, 133–139.
- (135) Babadi, M.; Demler, E. *Phys. Rev. B* **2011**, *84*, 235124.
- (136) Wang, D.-W.; Lukin, M. D.; Demler, E. *Phys. Rev. Lett.* **2006**, *97*, 180413.
- (137) Klawunn, M.; Duhme, J.; Santos, L. *Phys. Rev. A* **2010**, *81*, 013604.
- (138) Volosniev, A. G.; Fedorov, D. V.; Jensen, A. S.; Zinner, N. T. *Phys. Rev. A* **2012**, *85*, 023609.
- (139) Volosniev, A. G.; Armstrong, J. R.; Fedorov, D. V.; Jensen, A. S.; Zinner, N. T. 2011, arXiv:1112.2541.
- (140) Potter, A. C.; Berg, E.; Wang, D.-W.; Halperin, B. I.; Demler, E. *Phys. Rev. Lett.* **2010**, *105*, 220406.
- (141) Kalia, R. K.; Vashishta, P. *J. Phys. C* **1981**, *14*, L643.
- (142) Bruun, G. M.; Taylor, E. *Phys. Rev. Lett.* **2008**, *101*, 245301.
- (143) Wineland, D.; Monroe, C.; Itano, W. M.; Leibfried, D.; King, B. E.; Meekhof, D. M. *J. Res. Natl. Inst. Stand. Technol.* **1998**, *103*, 259.
- (144) Filinov, A.; Prokof'ev, N.; Bonitz, M. *Phys. Rev. Lett.* **2010**, *105*, 070401.
- (145) Boninsegni, M.; Prokof'ev, N.; Svistunov, B. *Phys. Rev. Lett.* **2006**, *96*, 070601.
- (146) Astrakharchik, G.; Boronat, J.; Kurbakov, I.; Lozovik, Y. *Phys. Rev. Lett.* **2007**, *98*, 060405.
- (147) Mora, C.; Parcollet, O.; Waintal, X. *Phys. Rev. B* **2007**, *76*, 064511.
- (148) F. Mazzanti, G. E. A.; Zillich, R. E.; Boronat, J. *Phys. Rev. Lett.* **2009**, *102*, 110405.
- (149) Hufnagel, D.; Kaltseis, R.; Apaja, V.; Zillich, R. E. *Phys. Rev. Lett.* **2011**, *107*, 065303.
- (150) Pupillo, G.; Micheli, A.; Boninsegni, M.; Lesanovsky, I.; Zoller, P. *Phys. Rev. Lett.* **2010**, *104*, 223002.
- (151) Belousov, A. I.; Lozovik, Y. E. *Eur. Phys. J. D* **2000**, *8*, 251.
- (152) Yu., E.; Lozovik, S. Y. V.; Willander, M. *JETP Lett.* **2004**, *79*, 473.
- (153) Ludwig, P.; Balzer, K.; Filinov, A.; Stolz, H.; Bonitz, M. *New J. Phys.* **2008**, *10*, 083031.
- (154) Bedanov, V. M.; Peeters, F. M. *Phys. Rev. B* **1994**, *49*, 2667.
- (155) Filinov, A.; Böning, J.; Bonitz, M.; Lozovik, Y. *Phys. Rev. B* **2008**, *77*, 214527.
- (156) Pupillo, G.; Micheli, A.; Boninsegni, M.; Lesanovsky, I.; Zoller, P. 2009, arXiv:0904.2735.
- (157) J. Piyush, F. C.; Boninsegni, M. *Phys. Rev. B* **2011**, *84*, 014534.
- (158) Golomedov, A. E.; Astrakharchik, G. E.; Lozovik, Y. E. *Phys. Rev. A* **2011**, *84*, 033615.
- (159) Cremon, J. C.; Bruun, G. M.; Reimann, S. M. *Phys. Rev. Lett.* **2010**, *105*, 255301.
- (160) Nelson, D. R.; Halperin, B. I. *Phys. Rev. B* **1979**, *19*, 2457.
- (161) Young, A. P. *Phys. Rev. B* **1979**, *19*, 1855.
- (162) Lin, S.; Zheng, B.; Trimper, S. *Phys. Rev. E* **2006**, *73*, 066106.
- (163) Spivak, B.; Kivelson, S. A. *Phys. Rev. B* **2004**, *70*, 155114.
- (164) O'Dell, D. H. J.; Eberlein, C. *Phys. Rev. A* **2007**, *75*, 013604.

- (165) Cooper, N. R.; Rezayi, E. H.; Simon, S. H. *Phys. Rev. Lett.* **2005**, *95*, 200402.
- (166) Zhang, J.; Zhai, H. *Phys. Rev. Lett.* **2005**, *95*, 200403.
- (167) Yi, S.; Pu, H. *Phys. Rev. A* **2006**, *73*, 061602.
- (168) Komineas, S.; Cooper, N. R. *Phys. Rev. A* **2007**, *75*, 023623.
- (169) Baranov, M. A.; Osterloh, K.; Lewenstein, M. *Phys. Rev. Lett.* **2005**, *94*, 070404.
- (170) Baranov, M. A.; Fehrmann, H.; Lewenstein, M. *Phys. Rev. Lett.* **2008**, *100*, 200402.
- (171) Grass, T.; Baranov, M. A.; Lewenstein, M. *Phys. Rev. A* **2011**, *84*, 043605.
- (172) Hubbard, J. *Proc. R. Soc. London A* **1963**, *276*, 238.
- (173) Lee, P. A.; Nagaosa, N.; Wen, X.-G. *Rev. Mod. Phys.* **2006**, *78*, 17–85.
- (174) Jaksch, D.; Bruder, C.; Cirac, J. I.; Gardiner, C. W.; Zoller, P. *Phys. Rev. Lett.* **1998**, *81*, 3108–3111.
- (175) Hofstetter, W.; Cirac, J. I.; Zoller, P.; Demler, E.; Lukin, M. D. *Phys. Rev. Lett.* **2002**, *89*, 220407.
- (176) Fisher, M. P. A.; Weichman, P. B.; Grinstein, G.; Fisher, D. S. *Phys. Rev. B* **1989**, *40*, 546–570.
- (177) Greiner, M.; Mandel, O.; Esslinger, T.; Hänsch, T.; Bloch, I. *Nature* **2002**, *415*, 39.
- (178) Spielman, I. B.; Phillips, W. D.; Porto, J. V. *Phys. Rev. Lett.* **2007**, *98*, 080404.
- (179) Haller, E.; Hart, R.; Mark, M. J.; Danzl, J. G.; Reichsöllner, L.; Gustavsson, M.; Dalmonde, M.; Pupillo, G.; Nägerl, H.-C. *Nature* **2010**, *466*, 597.
- (180) Stöferle, T.; Moritz, H.; Günter, K.; Köhl, M.; Esslinger, T. *Phys. Rev. Lett.* **2006**, *96*, 030401.
- (181) Jördens, R.; Strohmaier, N.; Günter, K.; Moritz, H.; Esslinger, T. *Nature* **2008**, *455*, 204–207.
- (182) Schneider, U.; Hackermüller, L.; Will, S.; Best, T.; Bloch, I.; Costi, T. A.; Helmes, R. W.; Rasch, D.; Rosch, A. *Science* **2008**, *322*, 1520–1525.
- (183) Capogrosso-Sansone, B.; Trefzger, C.; Lewenstein, M.; Zoller, P.; Pupillo, G. *Phys. Rev. Lett.* **2010**, *104*, 125301.
- (184) Bruder, C.; Fazio, R.; Schön, G. *Phys. Rev. B* **1993**, *47*, 342–347.
- (185) Sasaki, S.; Ishiguro, R.; Caupin, F.; Maris, H. J.; Balibar, S. *Science* **2006**, *313*, 1098–1100.
- (186) Prokofev, N. V. *Adv. Phys.* **2007**, *56*, 381.
- (187) Anderson, P. W. 2011, arXiv:1102.4797v1.
- (188) Batrouni, G. G.; Scalettar, R. T.; Zimanyi, G. T.; Kampf, A. P. *Phys. Rev. Lett.* **1995**, *74*, 2527–2530.
- (189) Yi, S.; Li, T.; Sun, C. P. *Phys. Rev. Lett.* **2007**, *98*, 260405.
- (190) Danshita, I.; de Melo, C. A. R. S. *Phys. Rev. Lett.* **2009**, *103*, 225301.
- (191) Pollet, L.; Picon, J. D.; Buechler, H.; Troyer, M. *Phys. Rev. Lett.* **2010**, *104*, 125302.
- (192) Boninsegni, M.; Prokofev, N. V. *Phys. Rev. B* **2008**, *77*, 092502.
- (193) Dang, L.; Boninsegni, M.; Pollet, L. *Phys. Rev. B* **2008**, *78*, 132512.
- (194) Boninsegni, M.; Prokofev, N. *Phys. Rev. Lett.* **2005**, *95*, 237204.
- (195) Wessel, S.; Troyer, M. *Phys. Rev. Lett.* **2005**, *95*, 127205.
- (196) Sengupta, P.; Pryadko, L. P.; Alet, F.; Troyer, M.; Schmid, G. *Phys. Rev. Lett.* **2005**, *94*, 207202.
- (197) Heidarian, D.; Damle, K. *Phys. Rev. Lett.* **2005**, *95*, 127206.
- (198) Melko, R. G.; Paramekanti, A.; Burkov, A. A.; Vishwanath, A.; Sheng, D. N.; Balents, L. *Phys. Rev. Lett.* **2005**, *95*, 127207.
- (199) Goral, K.; Santos, L.; Lewenstein, M. *Phys. Rev. Lett.* **2002**, *88*, 170406.
- (200) Andreev, A. F.; Lischitz, I. M. *JETP* **1969**, *29*, 1107.
- (201) Hubbard, J. *Phys. Rev. B* **1978**, *17*, 494.
- (202) Pokrovsky, V. L.; Uimin, G. V. *J. Phys. C* **1978**, *11*, 3535.
- (203) Menotti, C.; Trefzger, C.; Lewenstein, M. *Phys. Rev. Lett.* **2007**, *98*, 235301.
- (204) Trefzger, C.; Menotti, C.; Lewenstein, M. *Phys. Rev. A* **2008**, *78*, 043604.
- (205) Campbell, G. K.; Mun, J.; Boyd, M.; Medley, P.; Leanhardt, A. E.; Marcassa, L.; Pritchard, D. E.; Ketterle, W. *Science* **2006**, *313*, 649.
- (206) Foelling, S.; Widera, A.; Mueller, T.; Gerbier, F.; Bloch, I. *Phys. Rev. Lett.* **2006**, *97*, 060403.
- (207) Mikelsons, K.; Freericks, J. K. *Phys. Rev. A* **2011**, *83*, 043609.
- (208) Sun, K.; Wu, C.; Sarma, S. D. *Phys. Rev. B* **2010**, *82*, 075105.
- (209) Yamaguchi, Y.; Sogo, T.; Ito, T.; Miyakawa, T. *Phys. Rev. A* **2010**, *82*, 013643.
- (210) Lin, C.; Zhao, E.; Liu, W. V. *Phys. Rev. B* **2010**, *81*, 045115.
- (211) Lin, C.; Zhao, E.; Liu, W. V. *Phys. Rev. B* **2011**, *83*.
- (212) Quintanilla, J.; Carr, S. T.; Betouras, J. J. *Phys. Rev. A* **2009**, *79*, 031601(R).
- (213) Fregoso, B. M.; Sun, K.; Fradkin, E.; Lev, B. L. *New J. Phys.* **2009**, *11*, 103003.
- (214) Chaikin, P. M.; Lubensky, T. C. *Principles of Condensed Matter Physics*; Cambridge University Press: Cambridge, 1995.
- (215) Trefzger, C.; Menotti, C.; Lewenstein, M. *Phys. Rev. Lett.* **2009**, *103*, 035304.
- (216) Moore, G.; Read, N. *Nuclear Phys. B* **1991**, *360*, 362–396.
- (217) Fradkin, E.; Nayak, C.; Tsvetlik, A.; Wilczek, F. *Nucl. Phys. B* **1998**, *516*, 704.
- (218) Cooper, N. R. *Phys. Rev. Lett.* **2004**, *92*, 220405.
- (219) Büchler, H.; Micheli, A.; Zoller, P. *Nature Phys.* **2007**, *3*, 726.
- (220) Schmidt, K. P.; Dorier, J.; Laeuchli, A. *Phys. Rev. Lett.* **2008**, *101*, 150405.
- (221) Tewari, S.; Scarola, V. W.; Senthil, T.; Das Sarma, S. *Phys. Rev. Lett.* **2006**, *97*, 200401.
- (222) Capogrosso-Sansone, B.; Wessel, S.; Büchler, H.; Zoller, P.; Pupillo, G. *Phys. Rev. B* **2009**, *79*, 020503(R).
- (223) Micheli, A.; Brennen, G.; Zoller, P. *Nature Phys.* **2006**, *2*, 341–347.
- (224) Douçot, B.; Feigel'man, M. V.; Ioffe, L. B.; Ioselevich, A. S. *Phys. Rev. B* **2005**, *71*, 024505.
- (225) Wall, M. L.; Carr, L. D. *Phys. Rev. A* **2010**, *82*, 013611.
- (226) Gorshkov, A. V.; Manmana, S. R.; Chen, G.; Demler, E.; Lukin, M. D.; Rey, A. M. *Phys. Rev. A* **2011**, *84*, 033619.
- (227) Gorshkov, A. V.; Manmana, S. R.; Chen, G.; Ye, J.; Demler, E.; Lukin, M. D.; Rey, A. M. *Phys. Rev. Lett.* **2011**, *107*, 115301.
- (228) Ogata, M.; Fukuyama, H. *Rep. Prog. Phys.* **2008**, *71*, 036501.
- (229) Yu, H.; Liu, W. M.; Lee, C. 2009, arXiv:0910.4922v1.
- (230) Schachenmayer, J.; Lesanovsky, I.; Micheli, A.; Daley, A. J. *New J. Phys.* **2010**, *12*, 103044.
- (231) Hauke, P.; Cucchietti, F. M.; Müller-Hermes, A.; Bañuls, M.-C.; Cirac, J. I.; Lewenstein, M. *New J. Phys.* **2010**, *12*, 113037.
- (232) Porras, D.; Cirac, J. *Phys. Rev. Lett.* **2004**, *92*, 207901.
- (233) Barnett, R.; Petrov, D.; Lukin, M.; Demler, E. *Phys. Rev. Lett.* **2006**, *96*, 190401.
- (234) Herrera, F.; Litinskaya, M.; Krems, R. V. *Phys. Rev. A* **2010**, *82*, 033428.
- (235) Pérez-Ros, J.; Herrera, F.; Krems, R. V. *New J. Phys.* **2010**, *12*, 103007.
- (236) Agranovich, V. *Excitations in Organic Solids*; Oxford University Press: New York, 2009.
- (237) Zoubi, H.; Rocca, G. C. L. *Phys. Rev. B* **2005**, *72*, 125306.
- (238) Rabl, P.; Zoller, P. *Phys. Rev. A* **2007**, *76*, 042308.
- (239) Brennen, G. K.; Micheli, A.; Zoller, P. *New J. Phys.* **2007**, *9*, 138.
- (240) Alexandrov, A. *Theory of superconductivity*; IoP Publishing: Philadelphia, PA, 2003.
- (241) Pupillo, G.; Griessner, A.; Micheli, A.; Ortner, M.; Wang, D.-W.; Zoller, P. *Phys. Rev. Lett.* **2008**, *100*, 050402.
- (242) Ortner, M.; Micheli, A.; Pupillo, G.; Zoller, P. *New J. Phys.* **2009**, *11*, 055045.
- (243) Mahan, G. *Many Particle Physics*; Kluwer Academic/Plenum Publishers: New York, 2000.
- (244) Haldane, F. D. M. *Phys. Rev. Lett.* **1981**, *47*, 1840.
- (245) Giamarchi, T. *Quantum Physics in One Dimension*; Oxford University Press: Oxford, 2003.

- (246) Gogolin, A. O.; Nersesyan, A. A.; Tsvelik, A. M. *Bosonization and strongly correlated systems*; Cambridge University Press: Cambridge, 1998.
- (247) Giamarchi, T. *Chem. Rev.* **2004**, *104*, 5037–56.
- (248) Y. Tsukamoto, N. K. *J. Phys. Soc. Jpn.* **2000**, *69*, 149.
- (249) Inoue, H.; Nomura, K. *J. Phys. A: Math. Gen.* **2006**, *39*, 2161.
- (250) Mermin, N. D.; Wagner, H. *Phys. Rev. Lett.* **1966**, *17*, 1133.
- (251) Hohenberg, P. C. *Phys. Rev.* **1967**, *158*, 383.
- (252) Tonks, L. *Phys. Rev.* **1936**, *50*, 955.
- (253) Girardeau, M. *J. Math. Phys.* **1960**, *1*, 516.
- (254) Citro, R.; Orignac, E.; De Palo, S.; Chiofalo, M. L. *Phys. Rev. A* **2007**, *75*, 051602.
- (255) Citro, R.; Palo, S. D.; Orignac, E.; Pedri, P.; Chiofalo, M. L. *New J. Phys.* **2008**, *10*, 045011.
- (256) Arkhipov, A.; Astrakharchik, G.; Belikov, A.; Lozovik, Y. *JETP Lett.* **2005**, *82*, 39–43, 10.1134/1.2045336.
- (257) Roscilde, T.; Boninsegni, M. *New J. Phys.* **2010**, *12*, 033032.
- (258) Dalmonte, M.; Pupillo, G.; Zoller, P. *Phys. Rev. Lett.* **2010**, *105*, 140401.
- (259) Lieb, E. H.; Liniger, W. *Phys. Rev.* **1963**, *130*, 1605.
- (260) Pedri, P.; Palo, S. D.; Orignac, E.; Citro, R.; Chiofalo, M. L. *Phys. Rev. A* **2008**, *77*, 015601.
- (261) Büchler, H. P.; Blatter, G.; Zwerger, W. *Phys. Rev. Lett.* **2003**, *90*, 130401.
- (262) Burnell, F. J.; Parish, M. M.; Cooper, N. R.; Sondhi, S. L. *Phys. Rev. B* **2009**, *80*, 174519.
- (263) Batrouni, G.; Hebert, F.; Scalettar, R. *Phys. Rev. Lett.* **2006**, *97*, 087209.
- (264) Mishra, T.; Pai, R. V.; Ramanan, S.; Luthra, M. S.; Das, B. P. *Phys. Rev. A* **2009**, *80*, 043614.
- (265) Kumar, M.; Sarkar, S.; Ramasesha, S. 2008, arXiv:0812.5059v1.
- (266) Dalmonte, M.; Ercolessi, E.; Taddia, L. *Phys. Rev. B* **2011**, *84*, 085110.
- (267) Dalla Torre, E. G.; Berg, E.; Altman, E. *Phys. Rev. Lett.* **2006**, *97*, 260401.
- (268) White, S. R. *Phys. Rev. Lett.* **1992**, *69*, 2863.
- (269) Schollwoeck, U. *Rev. Mod. Phys.* **2005**, *77*, 259.
- (270) Tasaki, H. *Phys. Rev. Lett.* **1991**, *66*, 798.
- (271) Kennedy, T.; Tasaki, H. *Phys. Rev. B* **1992**, *45*, 304.
- (272) Daley, A. J.; Taylor, J. M.; Diehl, S.; Baranov, M. A.; Zoller, P. *Phys. Rev. Lett.* **2009**, *102*, 040402.
- (273) Dalmonte, M.; Dio, M. D.; Barbiero, L.; Ortolani, F. *Phys. Rev. B* **2011**, *83*, 155110.
- (274) Amico, L.; Mazzarella, G.; Pasini, S.; Cataliotti, F. *New J. Phys.* **2010**, *12*, 013002.
- (275) Schmitteckert, P.; Werner, R. *Phys. Rev. B* **2004**, *69*, 195115.
- (276) Ospelkaus, S.; Ni, K.-K.; Quémener, G.; Neyenhuis, B.; Wang, D.; de Miranda, M. H. G.; Bohn, J. L.; Ye, J.; Jin, D. S. *Phys. Rev. Lett.* **2010**, *104*, 030402.
- (277) Kestner, J. P.; Wang, B.; Sau, J. D.; Sarma, S. D. *Phys. Rev. B* **2011**, *83*, 174409.
- (278) Vidal, G. *Phys. Rev. Lett.* **2007**, *98*, 070201.
- (279) Wang, B.; Wang, D.-W.; Sarma, S. D. *Phys. Rev. A* **2010**, *82*, 021602(R).
- (280) Argüelles, A.; Santos, L. *Phys. Rev. A* **2007**, *75*, 053613.
- (281) Anfuso, F.; Rosch, A. *Phys. Rev. B* **2007**, *75*, 144420.
- (282) Berg, E.; Torre, E. G. D.; Giamarchi, T.; Altman, E. *Phys. Rev. B* **2008**, *77*, 245119.
- (283) Berg, E.; Levin, M.; Altman, E. *Phys. Rev. Lett.* **2011**, *106*, 110405.
- (284) Chang, C.-M.; Shen, W.-C.; Lai, C.-Y.; Chen, P.; Wang, D.-W. *Phys. Rev. A* **2008**, *79*, 053630.
- (285) Dalmonte, M.; Zoller, P.; Pupillo, G. *Phys. Rev. Lett.* **2011**, *107*, 163202.
- (286) Otsuka, H. *Phys. Rev. Lett.* **2000**, *84*, 5572.
- (287) Burovski, E.; Orso, G.; Jolicoeur, T. *Phys. Rev. Lett.* **2009**, *103*, 215301.
- (288) Capogrosso-Sansone, B.; Kuklov, A. *J. Low Temp. Phys.* **2011**, *165*, 213.
- (289) Kollath, C.; Meyer, J. S.; Giamarchi, T. *Phys. Rev. Lett.* **2008**, *100*, 130403.
- (290) Kivelson, S. A.; Fradkin, E.; Oganesyan, V.; Bindloss, I. P.; Tranquada, J. M.; Kapitulnik, A.; Howald, C. *Rev. Mod. Phys.* **2003**, *75*, 1201.
- (291) Huang, Y.-P.; Wang, D.-W. *Phys. Rev. A* **2009**, *80*, 053610.
- (292) Saffman, M.; Walker, T.; Molmer, K. *Rev. Mod. Phys.* **2010**, *82*, 2313.
- (293) Merkt, F. *Annu. Rev. Phys. Chem.* **1997**, *48*, 675–709.
- (294) Yamakita, Y.; Procter, S.; Goodgame, A.; Softley, T.; Merkt, F. *J. Chem. Phys.* **2004**, *121*, 1419.
- (295) DeMille, D. *Phys. Rev. Lett.* **2002**, *88*, 067901.
- (296) Yelin, S. F.; Kirby, K.; Côté, R. *Phys. Rev. A* **2006**, *74*, 050301.
- (297) Ortner, M.; Zhou, Y. L.; Rabl, P.; Zoller, P. *Quant. Inf. Proc.* **2011**, *10*, 793.
- (298) Bismut, G.; Pasquiou, B.; Maréchal, E.; Pedri, P.; Vernac, L.; Gorceix, O.; Laburthe-Tolra, B. *Phys. Rev. Lett.* **2010**, *105*, 040404.
- (299) Pasquiou, B.; Bismut, G.; Maréchal, E.; Pedri, P.; Vernac, L.; Gorceix, O.; Laburthe-Tolra, B. *Phys. Rev. Lett.* **2011**, *106*, 015301.
- (300) Bismut, G.; Laburthe-Tolra, B.; Maréchal, E.; Pedri, P.; Gorceix, O. *arXiv* **2012**, *1205*, 6305.